A Model of Galactic Dust and Gas from FIRAS

by

William J. Barnes

B.A., University of California (1987)

Submitted to the Department of Physics
in partial fulfillment of the requirements for the degree of

Doctor of Philosophy

at the

MASSACHUSETTS INSTITUTE OF TECHNOLOGY

May 1994

© Massachusetts Institute of Technology 1994

Signature of Author .....
Department of Physics
April 28, 1994

Certified by .....
Stephan S. Meyer
Associate Professor of Astronomy and Astrophysics at the University of Chicago
Thesis Supervisor

Accepted by .....
George Koster
Chairman, Department Committee

Science
MASSACHUSETTS INSTITUTE
OF TECHNOLOGY

MAY 25 1994

A Model of Galactic Dust and Gas from FIRAS

by

William J. Barnes

Submitted to the Department of Physics
on April 28, 1994, in partial fulfillment of the
requirements for the degree of
Doctor of Philosophy

Abstract

Data from the Far-Infrared Absolute Spectrophotometer (FIRAS) flown onboard NASA's Cosmic Background Explorer (COBE) are used to determine the emission from galactic dust and gas. The FIRAS instrument is described and the sources of error in its measurements are discussed. The method of Principal Component Analysis (PCA) is presented, refined, and used to analyze the data for global properties of dust and gas. The observed properties are used to test the photodissociation region (PDR) model of emission from diffuse clouds. Evidence for a cold dust component $T \sim 6.5$ K in the Galaxy is presented and the large scale emission of dust is shown to be approximately consistent with a plane-parallel distribution.

Thesis Supervisor: Stephan S. Meyer
Title: Associate Professor of Astronomy and Astrophysics at the University of Chicago

Acknowledgements

I accepted MIT's offer of graduate study without having ever traveled to the East Coast. Never having visited the campus nor its faculty, I find it serendipitous to have hooked up with Steve Meyer as my advisor. His tutelage in all matters of physics, analysis, and computers has proved invaluable to me. He also taught me the most important lesson I learned in graduate school, one that I will carry with for the rest of my life: always shave *after* you shower, it softens up your beard so that you don't get cut quite so often. Thanks. Thanks John Mather for pointing me in the right direction with regards to PCA and also for making a damn fine scientific instrument. Thanks Dale Fixsen for figuring out all the hard stuff so I wouldn't have to. Thanks Ed Cheng for giving me a place to sleep and food to eat. Thanks Chuck Bennett for turning me on to PDRs. Thanks Rich Isaacman for answering so many dumb questions and for letting me win at raquetball once in a while. Thanks Gene Eplee, Alice Trenholme, and Joel Gales for making the data perfect and pulling me away from my computer once and a while.

I would also like to acknowledge my fellow slaves in graduate physics who I toiled alongside through the years: Giaime, Fritschel, Stephens, Mavalvala, Christenson, Saha, and Page. I never did like Kovalik. Special thanks go to the Inman-Kowitt's for showing me the dangers in having *taste*. The award for friendship above and beyond the call of duty goes to Jason Puchalla who sat 3 feet apart from me in a windowless room for 8 hours a day listening to the same songs and the same jokes for over 2 years without once striking me.

I would like to thank my folks, Jim and Gayle, for having reared me with an appreciation of intellectual endeavors and for giving me the freedom to pursue them.

Thank you Susie, for having suffered with me through that horrible experience called New England and for making life fun.

Finally I would like to thank the late crew of the space shuttle *Challenger* whose mortal sacrifice delayed *COBE* just long enough so that I could work on it.

Contents

Chapter 1

Introduction

The Far-InfraRed Absolute Spectrophotometer (FIRAS) flown on board NASA's COsmic Background Explorer *COBE*[1] satellite measured the absolute flux of radiation in wavelength range 100 – 10,000 μm (1 μm = 10^{-4} centimeters). Although specifically designed to determine the spectrum of the Cosmic Background Radiation (CBR) this does not limit its ability to do some interesting astrophysics. With a beam size of 7° it was able to measure the diffuse emission from galactic dust and gas.

When we look at the Galaxy, we tend to concentrate on the stars due to the copious amounts of light they produce. Indeed the stars are responsible for $\sim$ 90% of the mass and $\sim$ 70% of the radiant energy found in the Galaxy and their presence has been known for centuries due the milky white band of light they produce across the night sky. Galactic dust and gas in the interstellar medium (ISM) are much more modest in appearance, having only been discovered within the last hundred years.

Evidence for galactic gas came in the early part of this century with the discovery of the "stationary" calcium line seen in absorption in the spectrum of a binary star. Since a binary star moves about its companion star, any spectral line associated with it would also shows signs of this motion and not be "stationary". It was thus determined to originate in the interstellar

[1]The National Aeronautics and Space Administration/Goddard Space Flight Center (NASA/GSFC) is responsible for the design, development, and operation of the Cosmic Background Explorer (*COBE*). Scientific guidance is provided by the *COBE* Science Working Group. GSFC is also responsible for the development of the analysis software and for the production of the mission data sets.

medium. Definitive evidence for the presence of dust between the stars came in the 1930s with the work of Trumpler. By investigating the apparent increase in the diameters of star clusters with distance from the solar system he inferred the presence of obscuring material. He went on to show that spectral reddening of the stars was due to small particles in interstellar space. These small submicron-sized dust particles absorb and scatter the shorter wavelengths of blue light much more efficiently than the longer wavelengths of red light. When we look at a star through this veil of dust, the star appears redder than it normally would because much of its blue light has been absorbed or scattered away.

The modest appearance of galactic dust and gas belies their importance in the Galaxy. In terms of mass, the gas contains $\sim$ 10% of the total galactic mass, with the dust containing an even smaller fraction ($\sim$ 0.1%). But if we look in terms total radiant energy, we find the dust responsible for $\sim$ 30% of total luminosity of the Galaxy. We see that the dust plays an important role in regulation of energy in the Galaxy for it converts visible and ultraviolet light given off by the stars into infrared and far-infrared radiation.

The birth and death cycle of a star shows the symbiotic relationship between the stellar and interstellar components of the Galaxy. A large cloud of dust and gas will collapse under the gravitational attraction of all the particles within the cloud. This contracting mass will eventually become dense enough to give birth to a star which then illuminates the surrounding dust, giving energy back to the ISM. In the final stages of the star's life it may pass through a red giant phase in which it balloons up to a huge size. At this stage the star has little gravitational hold on the dust in its extended atmosphere and its own radiation will push the dust particles out into the ISM. If the star dies in an explosive supernova, most of the mass that it originally obtained from the ISM is in fact returned to where it came from. Thus the stars and the ISM perform an ongoing exchange of material.

While the knowledge of interstellar gas has progressed since the 1940s with advances in radio astronomy and its study of the spectral lines of atoms, ions, and molecules, the continuum emission from interstellar dust has only been detectable within the last 20 years. The biggest gain in our knowledge of dust emission came from the Infrared Astronomical Satellite (*IRAS*) which gave us a picture of the Galaxy from 12 μm to 100 μm. Dust heated to a temperature of 20 K by the interstellar radiation field (ISRF) produces an emission spectrum with a peak

intensity around 100 μm, thus *IRAS* was able to study only one side of this spectrum. To study the entire dust spectrum, telescopes with advanced detectors were flown onboard balloons and observed dust emission mainly on the plane of the Galaxy.

The FIRAS instrument's spectral range allows it to measure both sides of the dust emission curve with extremely good spectral resolution. And since it measures the emission out to a wavelength of 10,000 μm it was able to discover very cold dust at a temperature $\sim$ 5 K [Wright 91] present in the Galaxy. Cold dust is thought to reside in the centers of clouds where it is shielded from the ISRF by overlying layers of dust.

A model of emission from both gas and dust residing in a cloud in interstellar space is given by the photodissociation region (PDR) model [Tielens 85a]. In this model radiation impinges upon dust grains residing in a cloud of neutral or molecular gas. Photoelectrons liberated from the grains go on to collisionally heat the gas. The gas then cools through various molecular and atomic transitions, but predominantly through the fine-structure transition of ionized carbon. Since the FIRAS observes both the thermal emission from the dust and the 158 μm line of C^+, its observations are uniquely suited to test the PDR model.

This thesis will present the physics of dust and gas emission necessary to model PDRs in chapter 2. Chapters 3 – 5 provide a description of the FIRAS instrument, calibration, and error analysis. These sections are drawn from the papers by [Mather 94b] and [Fixsen 94b] which this author had no part in but are included for an understanding of the uncertainties in the observations. The removal of extragalactic and interplanetary signals, so as to isolate those of galactic origin, is treated in chapter 6. The method of Principal Component Analysis (PCA) used to analyze the data is discussed in chapter 7 and PCA modeling techniques are presented in chapter 8. Chapter 9 presents the results from PCA modeling of the dust and gas emission seen by FIRAS. The PDR model is shown to account for the observed cold dust ($\sim$ 6.5 K) seen in the data and the observed relationship between the C^+ intensity and the dust temperature.

Chapter 2

Physics

2.1 Dust Emission

In order to describe dust emission in the FIR we follow [Whittet 92] and consider the classical dust grain as a spherical particle with a radius $a \sim 0.1\,\mu$m. It will absorb power from the interstellar radiation field (ISRF) according to

$$W_{\rm abs} = c(\pi a^2) \int_0^\infty Q_{\rm abs}(\nu) u_\nu d\nu \tag{2.1}$$

where c is the speed of light, ν is the frequency of radiation, $Q_{\rm abs}(\nu)$ is the frequency dependent absorption efficiency of the grain, and u_ν is the energy density of the ISRF at frequency ν. The grain radiates power as

$$W_{\rm rad} = 4\pi a^2 \int_0^\infty Q_{\rm em}(\nu) \pi B_\nu(T) d\nu \tag{2.2}$$

where $Q_{\rm em}(\nu)$ is the emission efficiency and

$$B_\nu(T) = \frac{2hc^2\nu^3}{e^{h\nu c/kT} - 1} \tag{2.3}$$

is the Planck function at the dust temperature T. In this work the frequency of radiation ν is given in $\rm cm^{-1}$ ($1\ \rm cm^{-1} = 30$ GHz) which is the natural unit for infrared spectrometers. In equilibrium, the absorption and emission rates are equal and we have

$$\int_0^\infty Q_{abs}(\nu) u_\nu d\nu = \frac{4\pi}{c} \int_0^\infty Q_{em}(\nu) B_\nu(T) d\nu \tag{2.4}$$

By Kirchoff's law we know that the two efficiencies are equal and can be replaced by the term $Q(\nu)$ which is known as the emissivity of the dust. Thus if we know the emissivity of the dust and measure its emission spectrum we can infer the strength of the ISRF.

In the FIR the wavelengths are much larger than the size of the dust particles so that $Q(\nu)$ can be approximated as a power law

$$Q(\nu) \propto \nu^{\alpha} \tag{2.5}$$

which results from Mie theory for small particles [Whittet 92]. The spectral index α is called the emissivity index and depends on the dust's physical properties. For most dust components α is theoretically derived to be 2.

[Tielens 87] derived a ν^2 emissivity for both amorphous and crystalline dust structures. A crystal can have an infrared active fundamental vibration whose absorptive properties follow that of a damped harmonic oscillator. The FIR wing of the oscillator's absorption curve is quadratic in frequency. Metals too, since their free electrons can be modeled as oscillators, have the same dependence. Amorphous solids are conglomerations of atoms without order and lack the excitation selection rules of crystals. Thus all vibrational modes can become excited and the FIR absorption will follow the density of vibrational states. According to the Debye law this implies that $Q(\nu) \propto \omega^2 \propto \nu^2$.

The only materials for which α does not take on a value of 2 are layered structures such as layer-lattice silicates and amorphous graphite. Since these structures are linked in only two dimensions, the phonons limited to this 2-D arena have a spectrum which goes as ω instead of ω^2. Depending on the amount of cross-linking between adjacent layers, α can range in value from 1.25 to 1.5 [Tielens 87] . For very small grains the 2-dimensional surface vibrations dominate over 3-dimensional modes and $Q(\nu) \propto \nu$ results.

There is a general belief in the astronomical dust community that, without exception, the value of α is 2. Most researchers accept this as fact to proceed with their analysis [Sodroski 89],[Draine 84]. This theoretical prejudice is explained in [Wright 93] who showed that by merely postulating that the dust has a polarizability, the Kramers-Kronig relation demands that α be an even integer greater than zero, with 2 being the obvious choice.

The importance of this one parameter is illustrated in the preliminary results from the FIRAS [Wright 91] where the average spectrum of galactic dust was fit to two models. One

model assumed an α of 2 and two dust components with two different temperatures, 20 K and 5 K. The other model was a single dust, temperature of $\sim$ 23 K, with a best fit α of 1.65 . The spectrum analyzed had sufficient long wavelength flux such that a single dust model with ν^2 emissivity failed to provide a good fit. Only by decreasing the emissivity index, effectively broadening the dust spectrum, can a single dust model approach a reasonable fit. The emissivity index and the number of dust components are thus related.

The preceding discussion concerned the emission from a classical dust grain in thermal equilibrium with the surrounding ISRF. However, as the *IRAS* observations showed, much of the mid-infrared emission from the Galaxy is due to small grains which are not in thermal equilibrium. For these grains the time between the absorption of successive photons is longer than the time it takes for the grain to cool. This causes the grain's temperature to pulse with the absorption of each photon. Given a mixture of these small grains the resulting emission spectrum exhibits a temperature distribution [Guhathakurta 89] which is peaked at low temperatures.

Having a good dust model provides information on both the mass and energetics of the Galaxy. It also impacts the field of cosmology where experimenters, searching for CBR anisotropies on the Wien side of the CBR spectrum, have to contend with foreground dust emission. The subtraction of an improper dust model is a major source of error in these highly sensitive experiments.

2.2 Gas Emission

The FIRAS detected emission from the interstellar gas due to the fine-structure transitions of C^0, C^+, and N^+ and from the rotational transitions of CO and are listed in table 2.2. The results are given in [Wright 91] and [Bennett 94] and here we concentrate on the large scale diffuse emission from C^+ which is the major cooling mechanism for neutral regions. The CO and C^0 lines trace the clumpy cold neutral and molecular regions which have little spatial extent in our 7° beam. The dust emission from these regions is thus very low compared to any warmer dust found in the beam. Since our goal is to draw conclusions regarding the dust and gas emission as these components coexist, we will ignore the C^0 and CO lines due to our inability to correlate them with such a small dust signal. The emission lines of N^+ originate

ν (cm^{-1})	λ (μm)	Species	Transition
7.681	1302.	CO	$J = 2 - 1$
11.531	867.2	CO	$J = 3 - 2$
15.375	650.4	CO	$J = 4 - 3$
16.419	609.1	[C I]	$2p^2 :^3 P_1 -^3 P_0$
19.237	519.8	CO	$J = 5 - 4$
27.00	370.4	[C I]	$2p^2 :^3 P_2 -^3 P_1$
48.72	205.3	[N II]	$2p^2 :^3 P_1 -^3 P_0$
63.395	157.7	[C II]	$2p :^2 P_{3/2} -^2 P_{1/2}$
82.04	121.9	[N II]	$2p^2 :^3 P_2 -^3 P_1$

Table 2.1: Lines detected by FIRAS

from HII regions since the ionization potential of nitrogen is 14.5 eV. Since these regions are of low density they also contribute little dust emission due to the low optical depth of dust. For this reason we will also ignore the N^+ lines.

Fine-structure transitions result from the interaction of the nucleus of an atom or ion and an orbiting electron. The electron, as it moves about the nucleus, sees a magnetic field due to the electrostatic potential of the nucleus. The intrinsic magnetic moment of the electron interacts with this magnetic field to produce a splitting of the ground state which depends on the total angular momentum ($\mathbf{J} = \mathbf{L} + \mathbf{S}$) of the outermost shell. For C^+ we have one electron in the 2p shell, thus $l = 1$ and $s = \frac{1}{2}$ determine that $j = \frac{3}{2}, \frac{1}{2}$ so that C^+ has the single fine-structure transition $2p :^2 P_{3/2} -^2 P_{1/2}$ at 158 μm. Since C^+ emission results from a magnetic dipole transition, this spectral line is optically thin in most astrophysical environments.

2.3 Photodissociation Regions

A model for coupled emission from both gas and dust is given by the *photodissociation region* (PDR) theoretical framework. [Tielens 85a] defined PDRs as neutral "regions where

FUV radiation dominates the heating and/or some important aspect of the chemistry. Thus photodissociation regions include most of the atomic gas in the galaxy, both in diffuse clouds and in denser regions ..." In this model far ultraviolet (FUV) photons (6–13.6 eV), from either the ISRF or nearby O and B stars, encounter regions of neutral gas and dust residing in molecular or diffuse clouds. The photons dissociate most molecular species and are energetic enough to overcome the work function $\sim$ 6 eV of a dust grain and liberate an electron. They will also ionize neutral carbon which has an ionization potential of 11.3 eV. A strong FUV flux produces enough electrons through these two processes to substantially heat the gas. While the dust cools by thermal emission, the main cooling mechanism available to the gas is the C^+ line which is only 92 K above the ground state.

The observable parameters seen by FIRAS are the dust temperature and the C^+ line intensity along a given line of sight. The following discussion shows how, from an observed dust temperature, we can predict this line intensity. The predicted dependence of the line intensity on dust temperature can then be compared with observations.

A one-dimensional PDR model of *diffuse* regions is given by [Hollenbach 91]. The model consists of a plane-parallel cloud of a given density whose surface is exposed to FUV flux. By solving the thermal and chemical balance equations at each cloud layer, the dust and gas temperatures are determined as a function of visual extinction into the cloud.

We will first model the dust temperature structure of the cloud to determine the relationship between the hotter dust at the surface of the cloud and the colder dust deeper within. From the dust temperature at the surface of the cloud we can infer the amount of impinging FUV flux. This amount of flux and the density of the cloud determine the temperature of the gas. By integrating the emission from the C^+ ions at the given gas temperature, we can predict the emergent line intensity.

In this model a dust grain's temperature depends not only on heating due to the ISRF but also due to thermal emission from the surrounding dust. Following [Hollenbach 91] we examine the energy balance of a spherical dust grain of radius a at an optical depth τ within the cloud. Equating emission and absorption we have

$$4\pi a^2 \int_0^\infty Q(\nu)\pi B_\nu(T_\mathrm{d})d\nu = \pi a^2 \int_0^\infty Q(\nu)F_\nu e^{-\tau_\nu} d\nu + 4\pi a^2 \int_0^\infty Q(\nu)\pi J_\nu d\nu \qquad (2.6)$$

where T_d is the temperature of the grain, F_ν is the FUV flux hitting the edge of the cloud,

τ_ν is the optical depth from the cloud edge to the dust grain, and J_ν the intensity of the FIR emission.

We take the emissivity of the dust to be

$$Q(\nu) = \begin{cases} \left(\frac{\nu}{\nu'}\right)^\alpha & \text{for } \nu < \nu' \\ 1 & \text{for } \nu > \nu' \end{cases} \tag{2.7}$$

The critical frequency ν' is the frequency above which the absorption cross section of the dust grain is purely geometrical and lies roughly in the visible. To calibrate ν' we turn to the observations of [Whitcomb 81] who observed the reflection nebula NGC 7023 in the FIR. Since the dust emission involves frequencies less than ν' and FUV flux involves frequencies greater than ν', in the simple case that the dust is heated only by the star HD 200775, equation 2.6 becomes

$$4\pi a^2 \int_0^{\nu'} \left(\frac{\nu}{\nu'}\right)^\alpha \pi B_\nu(T) d\nu = \pi a^2 \int_{\nu'}^\infty F_\nu d\nu \tag{2.8}$$

where T is the dust temperature at a distance R from the star. Integration gives

$$\nu'^\alpha = \frac{8\pi hc^2}{F_\star} \left(\frac{kT}{hc}\right)^{4+\alpha} \phi(\alpha) \tag{2.9}$$

where $F_\star = L_\star / 4\pi R^2$ is the integral of the star's FUV flux at the position of the grain. The function $\phi(\alpha)$ is given by [Mezger 82]

$$\phi(\alpha) = \int_0^\infty \frac{x^{3+\alpha} dx}{e^x - 1} = \Gamma(4+\alpha)\zeta(4+\alpha) \tag{2.10}$$

where Γ is the Euler gamma function and ζ is the Riemann zeta function. [Whitcomb 81] chose a point $R = .2$ pc distant from the star and found a dust temperature of 55 K based on observations at 55 and 125 μm. This temperature determination, however, assumed that $Q_\nu \propto \nu$. To allow for a variable emissivity index, we can solve for the temperature T' which matches these observations for a given α. We thus have

$$\nu' = \left[\frac{8\pi hc^2}{F_\star} \left(\frac{kT'}{hc}\right)^{4+\alpha} \phi(\alpha)\right]^{1/\alpha} \tag{2.11}$$

The effective temperature of HD 200775 is taken as 17000 K [Whitcomb 81] which yields an FUV flux of 1.2 erg s^{-1} cm^{-2} at the distance $R = .2$ pc. This determines that ν' ranges between $2.6 \times 10^5 - 2.9 \times 10^3$ cm^{-1} ($\sim .04 - 3.4$ μm) for $\alpha = 1 - 2$. This analysis has ignored any dust

heating due to stellar photons with energies less than 6 eV and may therefore overestimate the value of ν'.

In equation 2.6 the FIR intensity hitting the dust grain is given by [Hollenbach 91]

$$J_\nu = B_\nu(T_{\rm cbr}) + (0.42 - \ln\tau)\tau B_\nu(T_{\rm s}) \tag{2.12}$$

where the first term is due to the CBR and the second term is the FIR emission from dust in the cloud . This second term is derived assuming a dust optical depth $\tau \ll 1$ and that the emission is dominated by the warmer dust near the surface of the cloud. The parameters describing this surface layer are its temperature $T_{\rm s}$ and optical depth τ. The factor in parentheses accounts for the one-dimensional plane parallel geometry. The optical depth is given by

$$\tau = \tau_0 \left(\frac{\nu}{\nu_0}\right)^\alpha \tag{2.13}$$

where ν_0 is taken to be some nominal FIR frequency. τ can be estimated by evaluating the dust optical depth at the peak frequency of the dust emission curve determined by $T_{\rm s}$. This frequency can be approximated by

$$\nu_{max} \approx \frac{(3+\alpha)\,kT_{\rm s}}{hc} = (2.1 + .7\alpha)\;T_{\rm s} \quad [{\rm cm}^{-1}] \tag{2.14}$$

which yields

$$\tau = \tau_0 \left[\frac{(2.1 + .7\alpha)\,T_{\rm s}}{\nu_0}\right]^\alpha \tag{2.15}$$

Solving equation 2.6 for $T_{\rm d}$ as a function of visual extinction into the cloud we find

$$\begin{aligned} T_{\rm d}^{4+\alpha} \;=\; & \frac{1.6\times10^{-3}}{8\pi hc^2\phi(\alpha)}\left(\frac{hc}{k}\right)^{4+\alpha}\nu'^{\alpha}Ge^{-k_{uv}A_v} + T_{\rm cbr}^{4+\alpha} + \\ & \left[0.42 - \ln\tau_0\left(\frac{(2.1+.7\alpha)T_{\rm s}}{\nu_0}\right)^\alpha\right]\tau_0\left(\frac{2.1+.7\alpha}{\nu_0}\right)^\alpha T_{\rm s}^{4+2\alpha} \end{aligned} \tag{2.16}$$

where G is the frequency integral of the impinging FUV flux expressed in Habing units [Habing 68], and k_{uv} is the ratio of FUV optical depth to visual extinction A_v. The Habing unit (1.6×10^{-3} ergs s^{-1} cm^2) is determined from observations of O and B stars and expresses the strength of the ISRF in the FUV range. It has a value of unity for the solar neighborhood.

To find the dust temperature at the surface of the cloud we solve 2.16 by including only the first term on the right-hand-side and taking $A_v = 0$ to get

$$T_{\rm s} = \left[\frac{1.6\times10^{-3}}{8\pi hc^2\phi(\alpha)}\left(\frac{hc}{k}\right)^{4+\alpha}\nu'^{\alpha}G\right]^{\frac{1}{4+\alpha}} \tag{2.17}$$

We can invert this equation to establish the relationship between G and the cloud's surface temperature T_s. Substituting in for ν' from equation 2.11 we have

$$G = \left(\frac{T_s}{T'}\right)^{4+\alpha} \frac{F_\star}{1.6 \times 10^{-3}} \tag{2.18}$$

This equation allows us to determine G given an observed dust temperature but is dependent on the observations of [Whitcomb 81] through T' and on the integral of FUV flux $F_\star$ from HD 200775 responsible for the dust heating.

To find τ_0 we equate the impinging FUV flux to the emerging FIR flux from the dust as it is described by the surface temperature T_s

$$1.6 \times 10^{-3} G = 4\pi \int_0^\infty \tau B_\nu(T_s) d\nu \tag{2.19}$$

from which we get

$$\tau_0 T_s^{4+\alpha} = \frac{1.6 \times 10^{-3}}{8\pi h c^2 \phi(\alpha)} \left(\frac{hc}{k}\right)^{4+\alpha} \nu_0^\alpha G \tag{2.20}$$

Plugging in for T_s as derived in 2.17 we get

$$\tau_0 = \left(\frac{\nu_0}{\nu'}\right)^\alpha \tag{2.21}$$

Since the value of ν' may be an overestimate as stated previously, the resulting values for the optical depth may be too low.

Using the derived expressions for T_s and τ_0 we can write equation 2.16 as

$$T_d = \left\{ T_s^{4+\alpha} e^{-k_{uv} A_v} + T_{cbr}^{4+\alpha} + \left[0.42 - \alpha \ln\left(\frac{(2.1 + .7\alpha) T_s}{\nu'}\right)\right] \left(\frac{2.1 + .7\alpha}{\nu'}\right)^\alpha T_s^{4+2\alpha} \right\}^{\frac{1}{4+\alpha}} \tag{2.22}$$

which is the dust temperature T_d as a function of visual extinction A_v into the cloud. This formula shows the dust temperature's explicit dependence on the three sources of heating. The first term shows that the FUV heating decays with increasing visual extinction. The second and third terms are due to heating by CBR and thermal dust emission from the surface layer of the cloud. These two terms are constant and establish the minimum dust temperature in the cloud. Equation 2.22 is similar to the dust temperature derived by [Hollenbach 91] except that we have allowed for a variable emissivity index α .

An analytic equation for the gas temperature of the C^+ emission near the surface of the cloud is also presented in [Hollenbach 91] and its derivation is repeated here. The cooling

function due to a transition from $^2P_{3/2}$ to $^2P_{1/2}$ is given by [Tielens 85a]

$$\Lambda = n_2 A_{21} \Delta E \beta \tag{2.23}$$

where n_2 is the population of the $^3P_{3/2}$ state, $A_{21} = 2.4 \times 10^{-6}$ s^{-1} is the Einstein coefficient for spontaneous emission, $\Delta E = 1.27 \times 10^{-14}$ ergs = 92 K is the energy difference between the two states, and $\beta(\simeq 1)$ is the probability that the resulting photon will escape from the cloud. Since all the carbon is ionized near the surface we have $n_1 + n_2 = n_{C^+} = a_C n$ where a_C is the abundance of carbon relative to the neutral hydrogen density n of the cloud. The relationship between the two level populations is given by [Hollenbach 79]

$$\frac{n_2}{n_1} = \frac{g_2}{g_1} e^{-\Delta E/kT_g} \left(1 + \frac{\beta n_{cr}}{n}\right)^{-1} \tag{2.24}$$

where T_g is the temperature of the gas, $g_1 = 2$ and $g_2 = 4$ are the statistical weights of the levels and the critical density $n_{cr} = A_{21}/\gamma_{21}$ where γ_{21} is the collisional de-excitation rate coefficient for collisions with atomic hydrogen. The critical density defines the density at which collisional transitions match spontaneous transitions. Using these relationships we find the cooling rate of the gas to be

$$\Lambda = \frac{6.1 \times 10^{-20} a_C n \beta}{2 + e^{92/T_g}\left(1 + \frac{\beta n_{cr}}{n}\right)} \quad [\text{ergs s}^{-1}\ \text{cm}^{-3}] \tag{2.25}$$

The gas heating rate due to photoelectrons from dust grains is given by [Hollenbach 91]

$$\Gamma \simeq 4.86 \times 10^{-26} n G e^{-k_{uv} A_v} \frac{(1-x)^2}{x} \quad [\text{ergs s}^{-1}\ \text{cm}^{-3}] \tag{2.26}$$

where $x = \phi/13.6$ eV is the grain-charge parameter with ϕ the changing work function of the grain. At the surface of the cloud the FUV flux may liberate enough electrons from a dust grain to keep it positively charged. This charge increases the work function of the grain for any subsequent photoelectrons. This grain-charge effect on the photoelectron heating rate is included through the parameter x which satisfies

$$x^3 + (10\gamma - 0.44)x^2 - 10\gamma \simeq 0 \tag{2.27}$$

where

$$\gamma = \frac{G}{n} T_g^{1/2} e^{-k_{uv} A_v} \tag{2.28}$$

which is derived from equating the grain's photoejection rate with its electron recombination rate. The cubic equation in x can be solved to give

$$x = 1 - \frac{0.28}{10\gamma + 0.5} \tag{2.29}$$

Equating the heating and cooling rates we find that the gas temperature T_g satisfies the following equation

$$T_g = 92 \left\{ \ln \left(\frac{1}{1 + \beta n_{cr}/n} \left[\frac{1.61 \times 10^5 a_C \beta}{n\gamma} (\gamma + 5)(\gamma + 2.2) T_g^{1/2} - 2 \right] \right) \right\}^{-1} \tag{2.30}$$

which can be solved numerically. This equation is a function of the neutral hydrogen density n and the incident FUV flux G. Varying these two parameters allows us to investigate different physical environments such as high density ($n \sim 10^5$), high flux ($G \sim 10^5$) regions found in the Orion nebula [Tielens 85b], and low density ($n \sim 10^2$), low flux regions ($G \sim 10^2$) found in diffuse clouds.

With the equations 2.16 and 2.30 we plot the temperature of the dust and gas as a function of visual extinction into the cloud. For the standard parameters given in [Hollenbach 91] where $n = 1000$ cm^{-3}, $G = 1000$ Habing units, $a_C = 3 \times 10^{-4}$, $n_{cr} = 3000$ cm^{-3}, $k_{uv} = 1.8$, and $\alpha = 1$ we offer figure 2-1 as a schematic to a typical PDR region where the FUV flux enters from the left of the diagram. This figure is a reproduction of figure 3 given in [Hollenbach 91].

The shaded regions denote the various transitions in the chemical make-up of the cloud. To the left of $A_v = 0$ the FUV flux keeps hydrogen ionized. At $A_v \sim 0$–1, the dust attenuates the FUV flux enough for hydrogen to exist in its atomic state. Beyond $A_v \sim 4$ the FUV flux is low enough so that C^+ recombines with the electrons and CI forms. From $A_v \sim 0$–4 the dominant gas heating mechanism is the photoelectrons from the grains and the major gas cooling mechanism is the C^+ emission.

The dust temperature monotonically decreases with increasing extinction to a minimum determined by the heating due to the CBR and FIR emission from the dust at the cloud surface. The gas temperature, however, has a maximum at $A_v \sim 1$ in the cloud. This is due to the grain-charge effect at the edge of the cloud which decreases the efficiency with which FUV flux is transferred into gas heating. Further into the cloud, the grains become more neutral, increasing this efficiency and thus heating the gas to its maximum temperature.

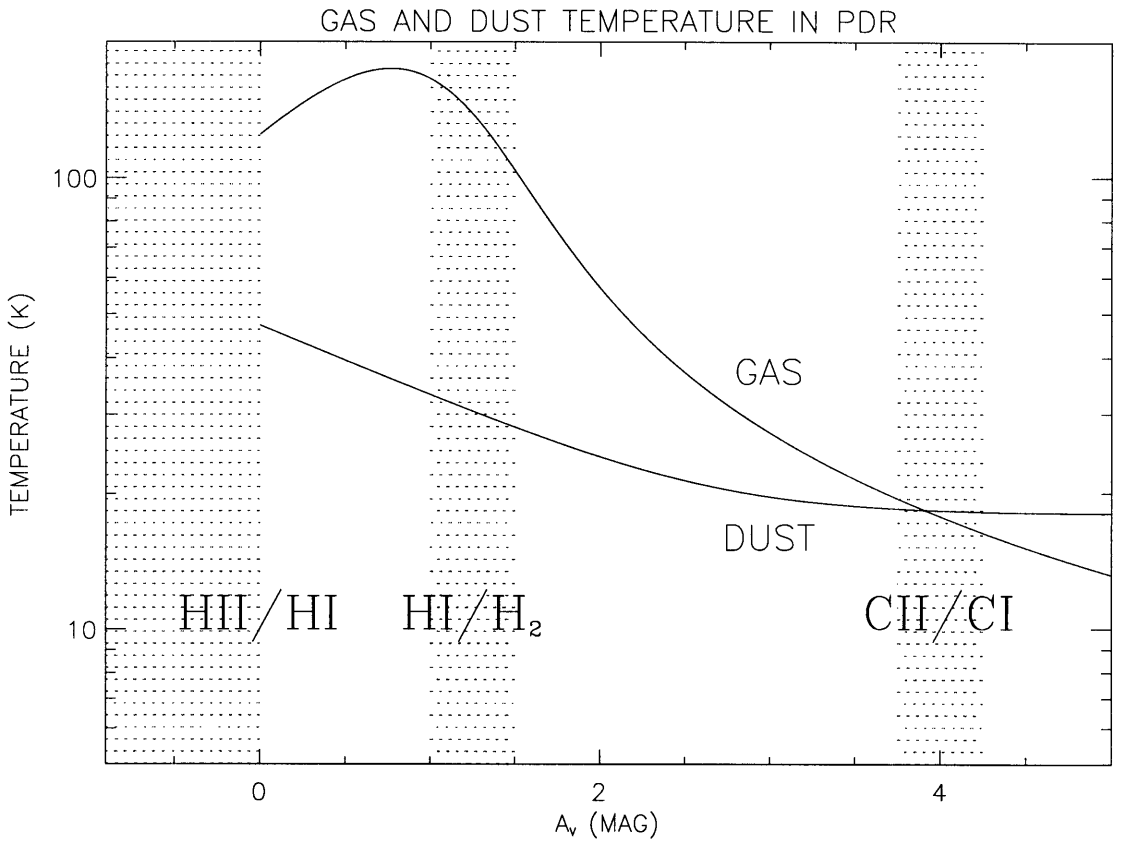

Figure 2-1: PDR model of dust and gas temperatures for a cloud with $n = 1000$ cm^{-3} illuminated by a flux $G = 1000$ Habing units. Also plotted are the HII – HI, HI – H_2, and CII – CI transition regions.

Since the temperature structure of the C^+ gas in the cloud is determined by the model, we can calculate the total emergent intensity. The total intensity is given by

$$I = \frac{1}{4\pi}\int_0^z \Lambda dz \tag{2.31}$$

where z is the distance along the line-of-sight through the cloud. In order to relate the physical distance z to A_v we use the determination of HI column density per magnitude of extinction $N_H/A_v = 1.8 \times 10^{21}$ cm^{-2}mag^{-1} [Bohlin 78] and the fact that the HI column density as a function of z is

$$N_H = \int_0^z n\, dz = nz \tag{2.32}$$

to get

$$z = 1.8 \times 10^{21}\frac{A_v}{n} \quad \Longrightarrow \quad dz = 1.8 \times 10^{21}\frac{dA_v}{n} \tag{2.33}$$

Substituting this into equation 2.31 and using Λ from equation 2.25 yields

$$I = 8.7 a_C \beta \int_0^4 \frac{dA_v}{2 + e^{92/T_g}\left(1 + \frac{\beta n_{cr}}{n}\right)} \quad [\text{ergs s}^{-1}\ \text{cm}^{-2}\ \text{sr}^{-1}] \tag{2.34}$$

where we have limited the integration to the region dominated by C^+ .

We now have the ability, once given a spectrum of dust and gas emission, to interpret the physical parameters in terms of the PDR model. For a given dust temperature T_s we can infer the FUV flux G with which we can predict the C^+ intensity. We can then compare the predicted and observed line intensities to test the validity of the PDR model.

Chapter 3

Instrument

The FIRAS was designed to make precision measurements of the spectrum of the Cosmic Background Radiation (CBR). By measuring the *difference* between the radiation spectrum from the sky and from an internal reference blackbody, FIRAS was able to search for spectral deviations of the CBR from a blackbody spectrum to $\sim 0.005\%$ (rms) of the peak brightness of the CBR spectrum. This section provides a description of the instrument and processing needed to understand the physical and algorithmic sources of error in the data.

3.1 Optical Concept

The FIRAS [Mather 94b] is a rapid-scan polarizing Michelson interferometer with two inputs and two outputs. A descriptive picture of the FIRAS from [Fixsen 94b] is given in figure 3-1. The inputs are defined by two horn shaped antennas. The *Sky Horn* [Mather 86] receives radiation from either the sky or from an external blackbody calibrator (*Xcal*) which can be placed into the horn's mouth. The *Ref Horn* receives radiation from an internal calibrator (*Ical*). As the mirror-transport-mechanism (*MTM*) varies the optical path difference between the two sides of the interferometer, the imposed phase delays produce an output signal that is the Fourier transform of the difference between the two input spectra. Thus FIRAS is a differential instrument because equal spectra coming in the two inputs will cause the output to be zero. Efforts were made to keep the instrument as symmetric as possible so that each thermal source in the beams had a radiative counterpart. This ensured that the sum total of their

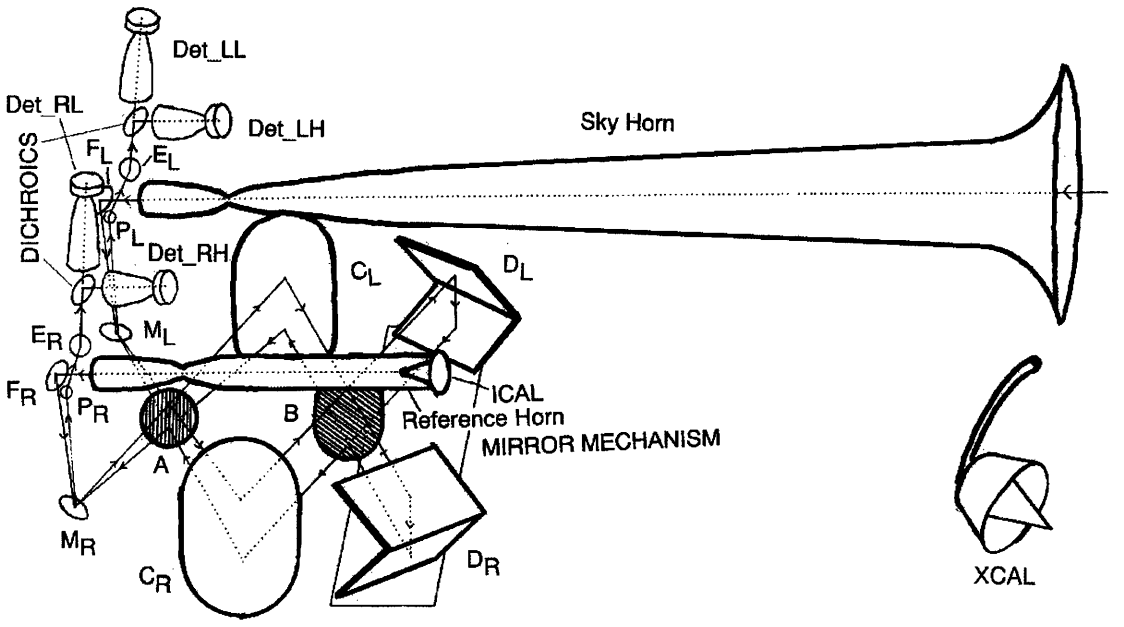

Figure 3-1: Simplified optical layout of the FIRAS, showing the positions of the horns, *Xcal, Ical,* mirrors, grids, *MTM*, and detectors.

radiative contributions to the measurement was kept at a minimum decreasing the dependence on instrument gain. The two outputs, designated *Left* and *Right*, each pass through a dichroic filter, splitting the instrument frequency range into low ($< 20\,\mathrm{cm}^{-1}$) and high ($> 20\,\mathrm{cm}^{-1}$) frequency channels.

To determine the absolute spectrum of the sky, the thermal emission due to sources within the instrument must be subtracted. The emissivities of these objects are determined by placing the external, temperature controlled, full beam calibrator (*Xcal*) into the *Sky Horn.* In this configuration all of the sources in the two inputs, and their temperatures, are known. By varying the temperatures of the two calibrators and the two horns one can determine the emissivity of each object at every frequency. With the temperature and emissivity for each part of the instrument determined, one can then establish the absolute flux in each part of the sky.

3.2 Calibrators

In order to compare the CBR with a blackbody spectrum, both the *Ical* used for measurement, and the *Xcal* used for calibration, were designed to be blackbodies. Both are made of Eccosorb CR110 [Emerson & Cuming Inc.], an iron loaded epoxy that is an efficient microwave absorber. The emissivity of the *Xcal* is measured to be > 0.99995 [Wilkinson 90]. The measured *Ical* emissivity is ~ 0.96 [Mather 94b].

Both objects are nearly isothermal, with the temperature inhomogeneity of the *Xcal* calculated to be less than 1 mK at 2.7 K . Each object could be commanded to any temperature between 2 and 25 K, with the higher temperatures necessary for characterizing the instrument's high frequency response.

3.3 Antennas

The *Sky Horn* is a flared horn antenna with a 7° field-of-view. The flare at the mouth of the horn attenuates the sidelobes entering the non-imaging parabolic concentrator portion of the horn. The étendue, or throughput, $A\Omega$ (= area × solid angle) of the *Sky Horn* can be evaluated most easily at its throat.

$$\begin{aligned} A\Omega &= \int d\Omega \int dA = A_{throat} \int_0^{2\pi} \int_0^{\pi/2} \sin\theta \cos\theta d\theta d\phi \\ &= \pi^2 r_{throat}^2 \sin^2\theta \Big|_0^{\pi/2} = \pi^2 r_{throat}^2 = 1.5 \text{ cm}^2\text{sr} \end{aligned}$$

where $r_{throat} = 0.39$ cm . Since, in a lossless system, the étendue is a conserved quantity, we can calculate the ideal half beamwidth (HBW) on the sky by equating this to the étendue evaluated at the mouth of the horn

$$A\Omega = \pi^2 r_{mouth}^2 \sin^2\theta \Big|_0^{\theta_{HBW}}$$

With $r_{mouth} = 6.83$ cm , θ_{HBW} becomes $\sim 3.5°$.

The *Ref Horn* is a similar non-imaging parabolic concentrator which receives emission from the *Ical* . Ideally both the *Ref Horn* and the *Sky Horn* would be exactly the same so that, if commanded to the same temperature, any emission from them would cancel out in the interferometer. However, due to space limitations on the satellite, the *Ref Horn* was smaller. To compensate for the length difference between the two horns, the mouth of the *Ref Horn* was

extended with a cylinder to achieve the same length-to-diameter ratio as the *Sky Horn*. This made the emissivity of the two horns nearly identical and maintained the instrument's optical balance.

3.4 Interferometer

Following the diagram in figure 3-1, with L and R denoting the *Left* and *Right* sides of the interferometer, each input beam, after encountering the folding flats F_L and F_R and the pick-off mirrors M_L and M_R, passes through the wire grid polarizer A. The vertical wires reflects a beam's vertical polarization while transmitting its horizontal polarization. Each polarized beam then encounters a collimating mirror, C_L or C_R, followed by a polarizing beamsplitter B which is rotated 45° with respect to A as viewed along the optical axis. The two beams are then sent to the dihedral mirrors D_L and D_R mounted on the traveling *MTM*. Each dihedral mirror consists of two flat mirrors joined at 90° . The dihedral is oriented with the joint in the horizontal plane and the plane of each flat at 45° to the vertical. This optical element, when acting upon the polarized beams from the beamsplitter, rotates a beam's polarization by 90° before sending it back to the beamsplitter.

This change in polarization enables that part of the beam which was first reflected now to be transmitted. The recombination at the beamsplitter creates a coherent beam whose polarization state is determined by the path length difference between the two arms of the interferometer. The beam then courses back to the collimating mirror and polarizer on its way out to the detectors. As the MTM changes the path length difference x, the optical output signal of the interferometer is given by

$$I_o(x) = \int_0^\infty d\nu \cos 2\pi\nu x \sum_k a_k(\nu) S_k(\nu) \tag{3.1}$$

where ν is the optical frequency, $a_k(\nu)$ is termed the efficiency and is the product of the étendue and emissivity for each of the k sources in the beam and $S_k(\nu)$ is the spectrum of each source. The balance of the instrument resides in the fact that for each source k there is a nearly identical source l whose efficiency $a_l(\nu) \approx -a_k(\nu)$ due to the 180° phase shift between them.

The two output beams, *Left* and *Right*, are each split into low ($2 - 20\,\mathrm{cm}^{-1}$) and high frequency ($20 - 95\,\mathrm{cm}^{-1}$) channels with a dichroic filter. Thus there are four outputs from the

interferometer: Left Low, Right Low, Left High, Right High. In addition the *MTM* can be scanned at two different speeds (Slow, Fast) for two different scan lengths (Short, Long) for a total of 16 possible data sets combining the 4 channels with the 4 scan modes. The data used in this thesis are from only two of those channels, Right High and Left Low, from only one scan mode, Short Slow. The justification is that a majority of the total data were taken in this particular mode and that these two channels have considerably higher signal/noise ratio (SNR) than the others.

The spectral resolution of the interferometer is approximately given by $1/\Delta_{max}$ where Δ_{max} is the maximum path difference. For the Short Slow mode this distance is 2.46 cm resulting in an ideal spectral resolution of $\sim .41$ cm^{-1}

3.5 Detectors

After being split by the dichroic filters, a detector measures the power at each of the four outputs. The detectors are composite diamond bolometers which detect the infrared power. The complex responsivity B [Volts/Watt] of the detectors can be modeled [Mather 82], [Mather 84a], [Mather 84b] by the formula

$$B(f,\vec{\beta}) = \frac{S_0(\vec{\beta})}{(1 + 2\pi i f \tau_e(\vec{\beta}))} \tag{3.2}$$

where f is the data frequency in Hz, $S_0(\vec{\beta})$ is the zero frequency voltage responsivity, $\tau_e(\vec{\beta})$ is the effective time constant of the detector, and $\vec{\beta}$ is a vector containing bolometer parameters and operating conditions. The optical frequency ν in cm^{-1} is related to the data frequency f in Hz through the equation $f = v\nu$ where v is the effective velocity of the *MTM* in cm s^{-1}. Since this is constant for our single scan mode we can recast the transfer function $B(f,\vec{\beta})$ in terms of the optical frequency $B(\nu,\vec{\beta})$.

The bolometer bath temperature is usually $\sim$ 1.6 K but for high frequency calibrations, where the calibrators are heated to $\sim$ 20 K, it gets up to 1.73 K due to thermal links between the calibrators and the detector mounts. This change in temperature produces a change in the responsivity and the parameters in $\vec{\beta}$ describe this dependence.

Cosmic rays deposit instantaneous spikes of power onto the detectors which convert them to large narrow voltage spikes or "glitches" in the measured interferogram. The pulse height

distribution of the glitch energies obeys an E^{-3} power law, the high-energy tail of which can be removed from the interferogram using a modified CLEAN algorithm described in [Isaacman 92].

3.6 Signal Processing

The signal from the detector is amplified by a factor between 10^2 and 3×10^5 and then passed through electronic filters which decrease the high frequency noise and compensate for the low-pass nature of detector itself. The electronics transfer function, described as a function of data frequency $Z(f)$, was determined by a preflight measurement of the electronic components [Fixsen 94b]. We again convert data frequency to optical frequency to get $Z(\nu)$ as our electronics transfer function.

3.7 Apodization

The measured interferogram is given by the optical interferogram after convolution with the transfer functions of both the detector B and the electronics Z

$$I(x) = \int_0^\infty d\nu \cos 2\pi\nu x \, Z(\nu) B(\nu, \vec{\beta}) \sum_k a_k(\nu) S_k(\nu) \tag{3.3}$$

where the index k runs over the objects in the beam : *Sky Horn, Ical, Ref Horn*, grids, collimator mirror, dihedral mirror, bolometer, and the *Xcal* if it is placed in the *Sky Horn.* The measured spectrum is the inverse Fourier transform of this interferogram

$$Y(\nu) = \int_{-\infty}^{+\infty} A(x) I(x) e^{-2\pi i \nu x} dx = Z(\nu) B(\nu, \vec{\beta}) \sum_k a_k(\nu) S_k(\nu) \tag{3.4}$$

Although we use only the real part of this spectrum for observations of dust and gas emission, the complex spectrum is necessary to determine any phase corrections.

$I(x)$ is not actually sampled over the range implied by the limits of the integration but only over a finite range determined by the length of the *MTM* scan. In order to account for this sampling and to reduce the sidelobes of the spectral response window function, we multiply $I(x)$ by an apodization function $A(x)$ before performing the transform. The function, fully detailed in [Fixsen 94b] and [Bennett 94], allows for the fact that the MTM scan is asymmetric about the zero path difference position ($x = 0$) and should fall smoothly to zero at the two ends

of the scan. While the inclusion of this function yields a well behaved spectrum, it reduces the instrument's spectral resolution from $\sim .41\,\mathrm{cm}^{-1}$ down to $\sim .7\,\mathrm{cm}^{-1}$ and correlates the noise between neighboring frequency points. The asymmetry causes correlations between the real and imaginary parts.

3.8 Summary

The spectrum of the sky is obtained by inverting equation 3.4 to yield

$$S_{sky}(\nu) = \frac{1}{a_{Xcal}(\nu)} \left[\frac{Y(\nu)}{Z(\nu)B(\nu,\vec{\beta})} - \sum_{k \neq Xcal} a_k(\nu) S_k(\nu) \right] \tag{3.5}$$

where efficiency for the sky is taken to be the same as that of the *Xcal*, $Y(\nu)$ is the complex Fourier transform of the apodized interferogram, $Z(\nu)$ is the electronics transfer function, and $B(\nu,\vec{\beta})$ is the complex responsivity of the bolometer. The sum includes all sources within the instrument: *Ical, Sky Horn, Ref Horn*, dihedral mirror, collimator mirror, wire grids, and bolometer. This spectrum samples a patch of sky with $\theta_{HBW} \sim 3.5°$ and a frequency resolution $\sim .7\,\mathrm{cm}^{-1}$.

Chapter 4

Calibration

Equation 3.5 is a simplification. Systematic effects introduced by the instrument due to mechanical vibrations, optically produced harmonics, and small phase shifts were also present in the measured complex spectra. To account for these artifacts the actual spectra we work with are described by [Fixsen 94b]

$$S_{sky}(\nu) = \frac{e^{i\nu\psi}}{a_{Xcal}(\nu)} \left[\frac{Y(\nu)}{Z(\nu)B(\nu,\vec{\beta})} - \sum_{k \neq Xcal} a_k(\nu) S_k(\nu) - C(\nu) \right] \tag{4.1}$$

The phase correction ψ remedies linear phase error due to mis-sampling of the zero path difference position ($x = 0$) in the interferometer. The value of ψ is determined by minimizing the spectrum's imaginary part. The complex vector $C(\nu)$ models the instrument's vibrational and harmonic contributions to the data [Fixsen 94b].

To calibrate the instrument, the *Xcal* is placed into the the mouth of the *Sky Horn* . This occurred for $\sim$ 3 days every month over the 10 month duration of the mission. In this state we know every source contributing to the measured signal and its temperature. Since each source of emission is nearly isothermal, the source spectrum is given by the Planck function $P(\nu, T) = 2hc^2\nu^3/(e^{h\nu c/kT} - 1)$ at the source temperature T. Equation 4.1 above can now be written

$$\frac{Y(\nu)}{Z(\nu)B(\nu,\vec{\beta})} - \sum_k a_k(\nu) P(\nu, T_k + dT_k) - C(\nu) = 0 \tag{4.2}$$

where the sum over the k sources now includes the *Xcal*. The photometric precision of the bolometers was greater then the thermometric precision of the controllable temperatures, so

temperature corrections dT_k were added to the measured temperatures T_k of the emitters. With the above formula as the basis for the χ^2 computation, the parameters $\vec{\beta}$, $a_k(\nu)$ and dT_k were found using a combination of the conjugate gradient and Levenberg-Marqurdt fitting methods [Fixsen 94b].

Once determined, the values for $\vec{\beta}$ and $a_k(\nu)$ are used to calibrate each sky spectrum. After Doppler shifting the data to the Solar System barycenter, the spectra are binned into 6144 equal area pixels, each 6.7 deg^2, by using the quadrilateralized spherical cube representation [O'Neill 76]. The final result is a collection of calibrated spectral measurements for each frequency bin for each position on the sky where data was taken. In this thesis the number of pixels with data is 5212.

Chapter 5

Error Analysis

The data contain both random and systematic errors. While physical models exist for some of these error sources, accounting for others relies on empirical fitting to reduce their influence in the data set. In the following sections we present the physical and empirical models which describe these errors so that we may arrive at the proper weights for use in modeling the data.

Following [Fixsen 94b], each calibrated spectrum on the sky is derived from an uncalibrated spectrum $Y_{p\nu}$, the calibration parameters $\vec{\beta}$ and $a_{k\nu}$, and the thermometrically measured temperatures T_k at the time of the observation, where ν denotes the optical frequency, p represents the pixel index of the spectrum, and k denotes the index of the optical elements in the instrument. Thus the functional form for the spectrum is

$$S_{p\nu} = S(Y_{p\nu}, \vec{\beta}, a_{k\nu}, T_k) = \frac{e^{i\nu\psi}}{a_{x\nu}} \left[\frac{Y_{p\nu}}{Z_\nu B_{\nu\vec{\beta}}} - \sum_{k \neq x} a_{k\nu} P_\nu(T_k) - C_\nu \right] \tag{5.1}$$

The uncertainties in these quantities propagate through to uncertainties in S as follows

$$\begin{aligned} \delta S_{p\nu} &= \frac{\partial S_{p\nu}}{\partial Y_{p\nu}} \delta Y_{p\nu} + \frac{\partial S_{p\nu}}{\partial \vec{\beta}} \delta\vec{\beta} + \frac{\partial S_{p\nu}}{\partial a_{k\nu}} \delta a_{k\nu} + \\ &\quad \frac{\partial S_{p\nu}}{\partial T_k} \delta T_k + \frac{\partial S_{p\nu}}{\partial T_x} \delta T_x \end{aligned} \tag{5.2}$$

The four independent sources of error in S are: detector noise $\delta Y_{p\nu}$, the covariance of the calibration parameters $\delta\vec{\beta}$ and $\delta a_{k\nu}$, random errors in the temperature measurements δT_k and absolute calibration error in the *Xcal* thermometry δT_x. The following sections describe each of these sources of error.

5.1 Detector Noise

The random error due to the detector noise of the bolometer is represented by the vector D which depends on frequency. D is determined from the all sky average of the variance within each of the pixels. While D is a good measure of this noise, it may not perfectly account for the true detector noise. Since detector noise is white noise with a short correlation time, it decreases with integration. To calculate this error for a given observation, we divide this noise vector by the square root of the number of interferograms that went into that observation. The covariance due to detector noise between the spectra of two different pixels p, p' at two different frequencies ν, ν' is given by

$$\sigma_D^2(pp'\nu\nu') = \frac{D_\nu D_{\nu'}}{\sqrt{N_p N_{p'}}}\delta_{pp'}\delta_{\nu\nu'} \tag{5.3}$$

where the delta functions are valid because the detector noise is independent for each pixel and frequency. The apodization function applied to the interferogram does in fact correlate the noise between neighboring frequency bins on the order of $\sim 5\%$ but this is ignored. We cannot ignore the errors induced by vibrations at certain frequencies. The increased error at these frequencies ($10.7\,\mathrm{cm}^{-1}, 73\,\mathrm{cm}^{-1}$) are accommodated by multiplying the detector noise at these frequencies by a factor of 10.

5.2 Efficiencies

The efficiencies $a_{k\nu}$ derived in the calibration model have nonzero off-diagonal covariances. These translate into covariances between the sky spectra of the form

$$\sigma_E^2(pp'\nu\nu') = \frac{\partial S_{p\nu}}{\partial a_{k\nu}}\mathbf{E}\frac{\partial S_{p'\nu'}}{\partial a_{l\nu'}}\delta_{\nu\nu'} \tag{5.4}$$

where $\mathbf{E}$ is the covariance matrix for the efficiencies of emitters k and l and the delta function reflects the fact the the efficiencies are derived independently for each frequency. For objects other than the *Xcal* we have

$$\frac{\partial S_{p\nu}}{\partial a_{k\nu}} = \frac{P_\nu(T_k) - P_\nu(T)}{a_{x\nu}} \tag{5.5}$$

where T is the temperature of the bolometer. For the *Xcal* efficiency $a_{x\nu}$ we have

$$\frac{\partial S_{p\nu}}{\partial a_{x\nu}} = \frac{-S_{p\nu}}{a_{x\nu}} \tag{5.6}$$

The error in this case is a gain error which multiplies each spectrum. These errors are referred to in the literature of [Fixsen 94b] as PEP errors since the efficiency covariance (E) is sandwiched between two Planck functions (P).

5.3 Random Temperature Errors

We can use the the temperature corrections dT_k obtained through the calibration scheme to model the covariance due to temperature errors in the sky spectra. This covariance has the form

$$\sigma_T^2(pp'\nu\nu') = \sum_{k\neq x}\sum_{l\neq x}\frac{\partial S_{p\nu}}{\partial T_k}U_{kl}\frac{\partial S_{p'\nu'}}{\partial T_l}\delta_{pp'} \tag{5.7}$$

where U_{kl} is the covariance between the temperatures of emitters k and l. Here we have

$$\frac{\partial S_{p\nu}}{\partial T_k} = -\frac{a_{k\nu}}{a_{x\nu}}\frac{\partial P_\nu(T_k)}{\partial T_k} \tag{5.8}$$

These errors are known as the PUP errors since the temperature error covariance matrix (U) is multiplied on the left and right by a Planck function (P). The PUP errors are well approximated by the error due to the *Ical* temperature alone since this object has the largest efficiency.

5.4 *Xcal* Temperature Error

The covariance due to errors in the *Xcal* temperature measurement propagate through to errors in the efficiencies and the bolometer parameters. The dependence of the spectrum on the *Xcal* temperature T_x is given by

$$\begin{aligned}\frac{\partial S_{p\nu}}{\partial T_x} &= \frac{\partial}{\partial T_x}\frac{1}{a_{x\nu}}\left[\frac{Y_{p\nu}}{Z_\nu B_{\nu\vec{\beta}}} - \sum_{k\neq x} a_{k\nu}P(T_k) - C_\nu\right] \\ &= -\frac{S_{p\nu}}{a_{x\nu}}\frac{\partial a_{x\nu}}{\partial T_x} + \frac{1}{a_{x\nu}}\frac{\partial}{\partial T_x}\left[\frac{Y_{p\nu}}{Z_\nu B_{\nu\vec{\beta}}} - \sum_{k\neq x} a_{k\nu}P(T_k) - C_\nu\right]\end{aligned} \tag{5.9}$$

where we have omitted the phase correction factor in the above formula. By taking the derivative of the calibration equation 4.2 we have

$$\begin{aligned}\frac{\partial}{\partial T_x}\left[\frac{Y_{p\nu}}{Z_\nu B_{\nu\vec{\beta}}} - \sum_{k} a_{k\nu}P(T_k) - C_\nu\right] &= 0 \\ \Longrightarrow \quad \frac{\partial}{\partial T_x}\left[\frac{Y_{p\nu}}{Z_\nu B_{\nu\vec{\beta}}} - \sum_{k\neq x} a_{k\nu}P(T_k) - C_\nu\right] &= \frac{\partial}{\partial T_x}a_{x\nu}P_\nu(T_x)\end{aligned} \tag{5.10}$$

Thus equation 5.9 becomes

$$\begin{aligned}\frac{\partial S_{p\nu}}{\partial T_x} &= -\frac{S_{p\nu}}{a_{x\nu}}\frac{\partial a_{x\nu}}{\partial T_x} + \frac{1}{a_{x\nu}}\frac{\partial}{\partial T_x}a_{x\nu}P_\nu(T_x) \\ &= \left.\frac{\partial P_\nu(T)}{\partial T}\right|_{T_x} + \frac{P_\nu(T_x) - S_{p\nu}}{a_{x\nu}}\frac{\partial a_{x\nu}}{\partial T_x} \end{aligned} \tag{5.11}$$

The second term contains the uncertainty of the *Xcal* efficiency due to the uncertainty in its temperature and depends on the actual spectra measured. This term is included in the covariance of all the calibration parameters which are discussed in section 4.5 . Thus the covariance due to errors in the *Xcal* thermometry becomes

$$\sigma^2_{T_x}(pp'\nu\nu') = \left.\frac{\partial P_\nu(T)}{\partial T}\right|_{T_x} (\delta T_x)^2 \left.\frac{\partial P_{\nu'}(T)}{\partial T}\right|_{T_x} \tag{5.12}$$

These errors are known as the PTP errors since we are sandwiching the *Xcal* temperature error (T) between two Planck functions (P).

5.5 Bolometer Parameters

The bolometer parameters found in the calibration have covariances among themselves and also covariances with the efficiencies. Since the bolometer parameters depend only on the instrument state and not on any particular pixel or frequency, these errors are correlated across the sky and across frequencies. [Fixsen 94b] gives the following formula in deriving the covariance of calibration parameters

$$\mathbf{J}_{p\nu} = \Psi\frac{\partial S_{p\nu}}{\partial \vec{\beta}} - \Phi\frac{\partial S_{p\nu}}{\partial a_{k\nu}} \tag{5.13}$$

where the Ψ and Φ are functions of the Hessian of the calibration parameters and its inverse. The covariance involving the bolometer parameters and their interplay with the efficiencies is approximated by

$$\sigma^2_{\vec{\beta}}(pp'\nu\nu') \approx \mathbf{J}^T_{p\nu}\mathbf{J}_{p'\nu'} \tag{5.14}$$

which is referred to as the JCJ error term.

5.6 Summing the Errors

The covariances due to each source of error are added in quadrature so that the frequency-frequency covariance of the spectrum in pixel p with the spectrum of pixel p' is given by

$$\sigma^2 = \sigma_D^2 + \sigma_E^2 + \sigma_T^2 + \sigma_{T_x}^2 + \sigma_{\vec{\beta}}^2 \tag{5.15}$$

where the terms, in order of appearance, are referred to as D, PEP, PUP, PTP, JCJ. These errors are plotted in figure 5-1 for the two channels LLSS and RHSS. In the figures the D term gives the detector noise for a single interferogram so that for a typical number of interferograms ($\sim$ 10), this detector noise is reduced by $\sqrt{10}$. The spikes in the D vector at 10.7 cm^{-1} and 73 cm^{-1} account for the increased uncertainty due to vibrations at these frequencies. Since the PEP term is dependent upon the actual spectrum observed, the terms plotted are for out of plane viewing when all parts of the instrument were cold. The JCJ term can and does go negative at certain frequencies; thus, the absolute value of the JCJ term has been plotted to give one a feel for the order of magnitude of this term.

Stripes were detected in the sky data which matched the geometry with which the FIRAS scans the sky, indicating a systematic drift in the instrument. These artifacts were shown to depend on the time at which the data were taken. The data was divided into 10 periods corresponding to times of differing instrument states and, by assuming that the sky spectrum in each pixel was the same, a correction was applied to bring spectra from the different periods into agreement. For the low frequency data this correction was in the form of an offset spectrum while at high frequencies a gain correction was more appropriate. While these corrective measures give us smoother sky maps, they play havoc on the JCJ error determinations. For this reason I must regrettably ignore their role in the data. One may take heart in the fact that for the low frequencies the dominant error term, other than detector noise, is the PTP, while for high frequencies it is the PEP.

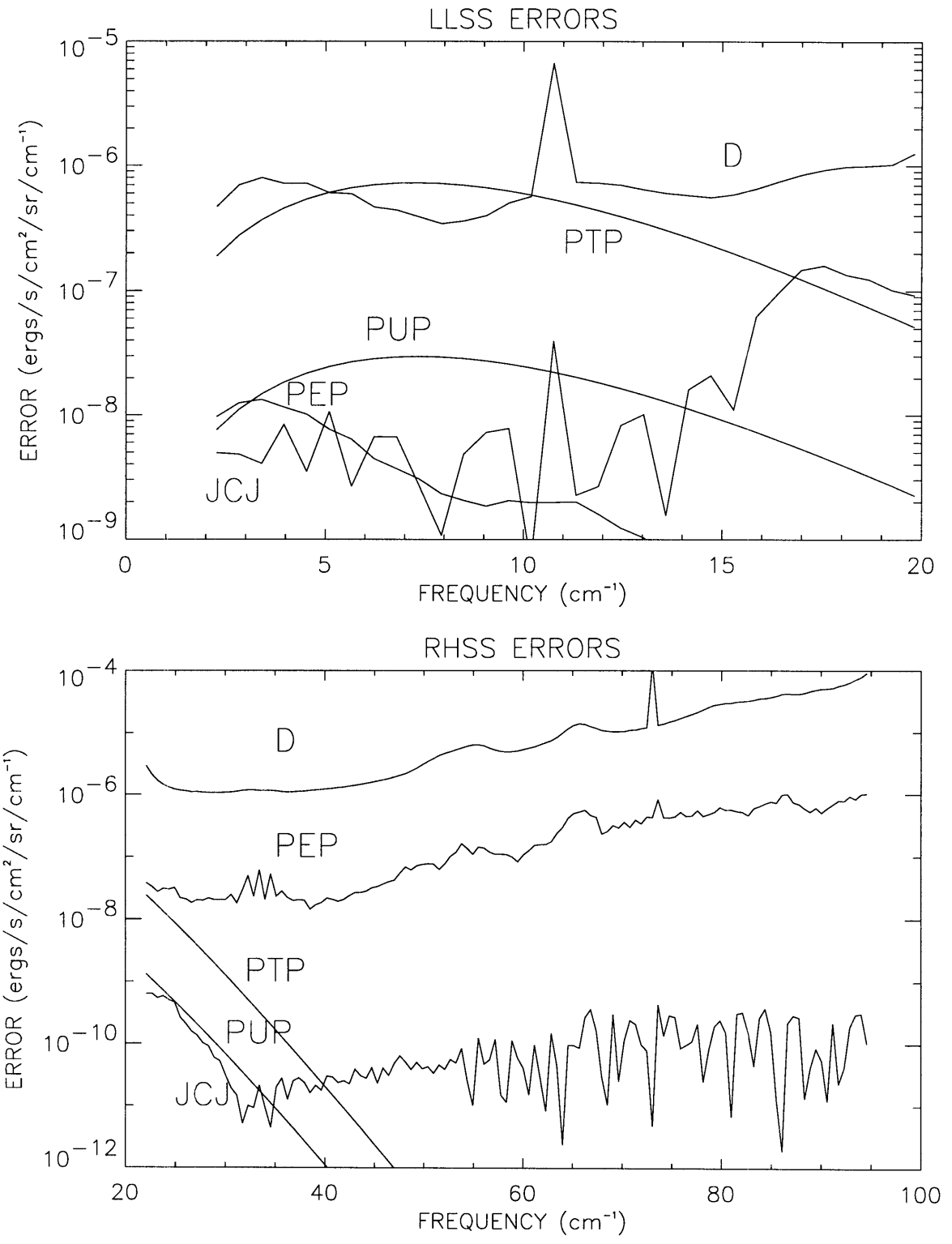

Figure 5-1: LLSS and RHSS Errors

Chapter 6

Data

The physical signals present in the data are the CBR monopole, the CBR dipole, zodiacal emission, and galactic emission. To focus on the emission from galactic dust and gas we need to excise both the extragalactic and interplanetary signals.

[Mather 94a] determine that the CBR monopole fits well to a Planck curve at a temperature of 2.726 ± 0.005 K with a rms deviation of 0.005% of the peak brightness of the spectrum. This determination was based on data taken during the last six weeks of the mission ("mini-cal" period) when the instrument was very stable and calibrated frequently. The data for the whole sky, however, were taken over the entire 10 month duration of the flight and may show a different CBR temperature. In order to subtract the monopole and dipole emission evidenced in the data we are using, we use the spatial template technique employed by [Fixsen 94a].

We posit that the low frequency data have 3 distinctive sources of emission each with its own spatial structure. The CBR monopole template is constant across the sky. The CBR dipole has a $\cos\theta$ dependence across the sky where θ is the angle from its hot pole located at $(l_0, b_0) = (264.4^\circ \pm 0.3^\circ , 48.4^\circ \pm 0.5^\circ)$ as determined by [Kogut 93] from the *COBE* Differential Microwave Radiometer (DMR) experiment. As in [Fixsen 94a] we take the integral of the high frequency power ($25 - 80$ cm^{-1}) as the galactic template. This template determination assumes that the low frequency dust signal is tracked by the high frequency power. To minimize the effect of galactic contamination on our determination of the monopole and dipole spectra, we exclude data with $|b| < 20^\circ$.

We derive the monopole and dipole spectra by fitting the data to these 3 spatial templates

independently for each frequency. Let $\mathbf{S}$ denote the $M \times N$ matrix containing the N point spectrum in each of the M pixels to be fit and $\mathbf{A}$ denote the $M \times 3$ matrix containing our 3 spatial models. Let $\mathbf{W}$ be $M \times M$ weights matrix containing the number of interferograms for each pixel along its diagonal, to weight each spectrum by its integration time. The normal equation for this least-squares problem is

$$\mathbf{A}^T\mathbf{W}\mathbf{A}\mathbf{M} = \mathbf{A}^T\mathbf{W}\mathbf{S}$$

whose solution is given by

$$\mathbf{M} = (\mathbf{A}^T\mathbf{W}\mathbf{A})^{-1}\mathbf{A}^T\mathbf{W}\mathbf{S}$$

where $\mathbf{M}$ is the $3 \times N$ matrix containing the best fit coefficients of each map for each frequency. The best fit spectra are shown in figure 6-1.

We fit the monopole spectrum to a Planck function and, in order to account for residual dust emission present, a dust spectrum with a fixed emissivity index (1.5) and a fixed dust temperature (20 K). The best fit monopole temperature is $T_{\rm cbr} = 2.72567 \pm 0.00001$ K where the uncertainty is statistical and we have not accounted for systematic temperature errors as was done by [Mather 94a]. For this fit $\chi^2/\mathrm{DOF} = 3.70$ which is high but, since we have neglected the systematic errors which come into play when we do large scale averages, not unexpected. We fit the galactic spectrum for a dust temperature having fixed the emissivity index at 1.5. The best fit dust temperature is $T_{\rm dust} = 13.89 \pm 0.76$ K with a $\chi^2/\mathrm{DOF} = 0.88$. The dipole spectrum is fit to the temperature derivative of the Planck function at the monopole temperature found above. The best fit dipole amplitude is $dT = 3.319 \pm .008$ mK with a $\chi^2/\mathrm{DOF} = 1.19$. The best fit models for these spectra are also plotted in figure 6-1.

Even though the monopole and dipole spectra were obtained from data greater than 20° off the galactic plane, we know their spatial dependence everywhere. These spectra, multiplied by their spatial templates, were subtracted from both the low frequency and high frequency data sets. Also subtracted were the measured FIRAS line intensities of CO, C^0, and N^+ [Gales 93]. These intensities were determined for each spectrum by first subtracting the best fit blackbody and dust ($\alpha = 2$) model. The residual spectrum was then fit with a 20^{th} order Legendre polynomial and line profiles at the accepted frequencies.

The emission due to zodiacal dust is a bit trickier to handle because the signal is weak and

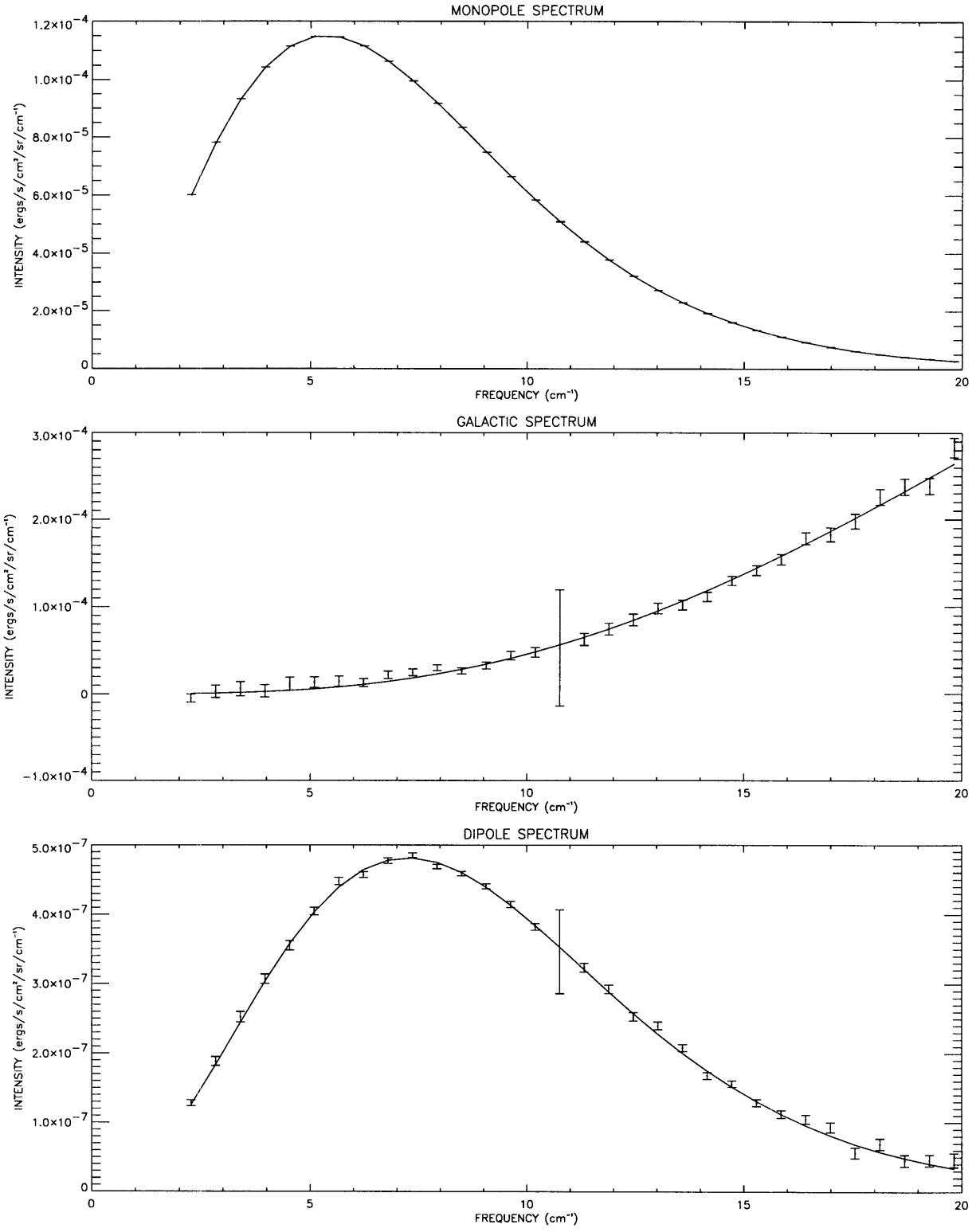

Figure 6-1: Monopole, Galactic and Dipole Spectra

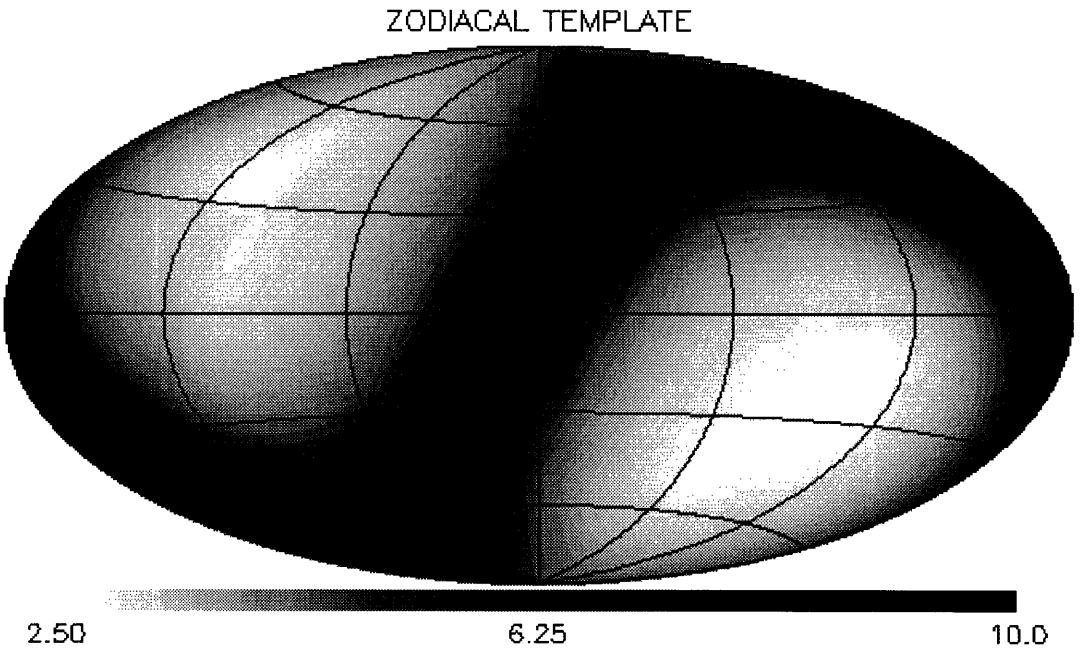

Figure 6-2: Zodiacal emission template

the FIRAS instrument is less efficient at the higher frequencies where the emission is stronger. The Diffuse InfraRed Background Experiment (DIRBE), also flown onboard the COBE satellite, measured this emission at wavelengths of 240 μm, 100 μm and smaller. [Fixsen 94c] has used a DIRBE determination of the zodiacal dust's spatial dependence, given in figure 6-2, to perform a template fit for the average zodiacal spectrum seen by FIRAS. No attempt has been made to allow the spectral changes due to differing elongation angles. The fit was performed on a combined FIRAS data set which included both low and high frequencies and the other templates included were a spatial monopole, a spatial dipole, and the integrated power of the high frequency channel which tracks the galactic dust emission. The resulting spectrum for the zodiacal emission, given in figure 6-3, is modeled by the dust spectrum

$$I_{\rm zod}(\nu) = 3.19 \times 10^{-9} \left(\frac{\nu}{\nu_0}\right)^{\alpha} B(\nu, T_{\rm zod})$$

where we have assumed $\alpha = 2$, $T_{\rm zod} = 250\,{\rm K}$, $\nu_0 = 40\,{\rm cm}^{-1}$ and we only fit for the optical depth. This spectrum, in combination with the zodiacal template in figure 6-2, was used to subtract the interplanetary emission from the high frequency data set. The low frequency data is unaffected by this contaminant.

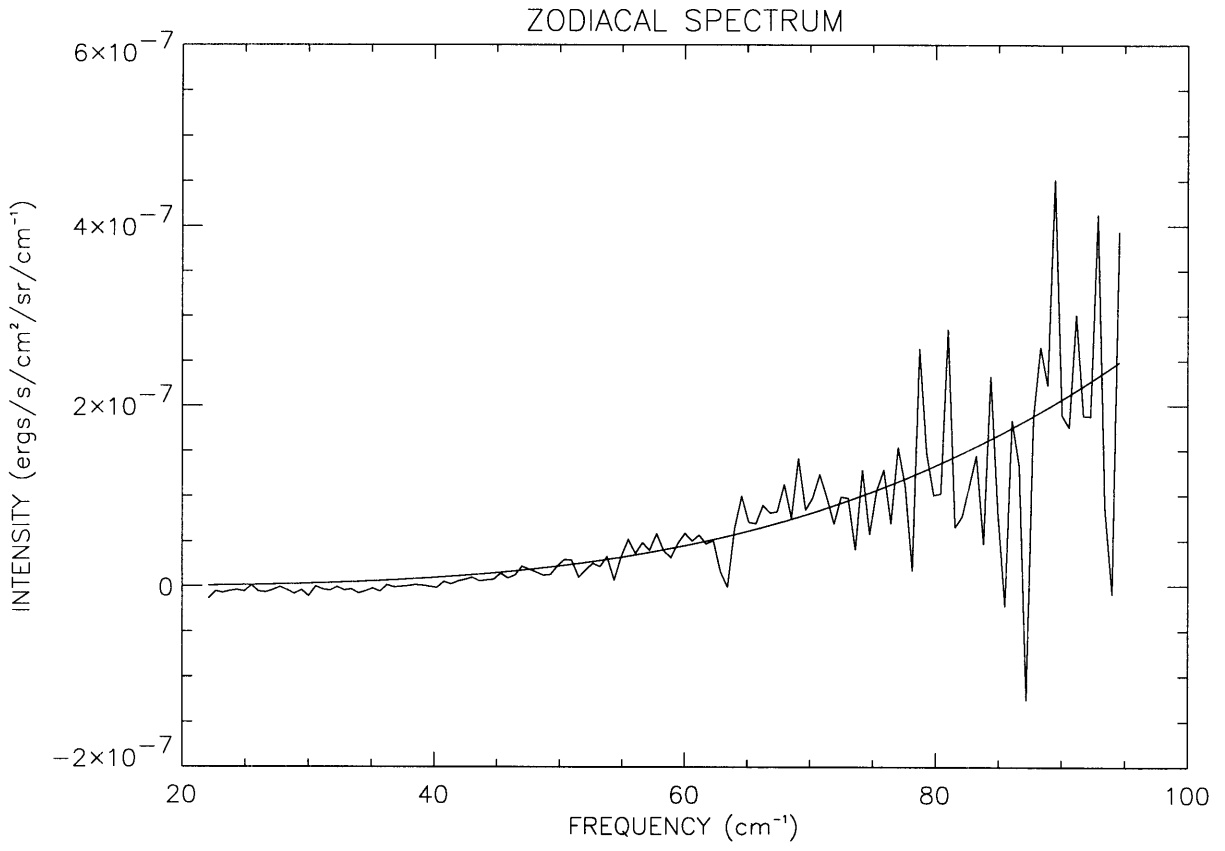

Figure 6-3: Zodiacal spectrum and model

The uncertainties in the subtraction of the zodiacal emission were taken to be 10% of the modeled spectrum and were propagated through to the final errors on the high frequency spectra. The errors due to removal of the CBR were not accounted for in either data set because the PTP calibration errors already include them.

Chapter 7

Principal Component Analysis

7.1 Motivation

Having removed the CBR, zodiacal, CO, C^0, and N^+ emission, our data set consists of $\sim$ 5000 spectra, each with $\sim$ 150 frequency bins, which sample the emission from dust and gas over the entire sky. A simple method of extracting the physical parameters of emission requires fitting each individual spectrum to a particular dust and gas model. The variability of the dust signal in the Galaxy makes it impossible to have one dust model with a single temperature describe all the spectra. The high latitude dust resides in an environment different from that of the low latitude dust and spectra from the inner Galaxy most certainly samples dust at different temperatures along the line of sight. We must thus decide how many dust components, each with its own optical depth, temperature, and emissivity index to fit to each spectrum. Matters are made more complicated because these three parameters are all highly correlated with each other. This fitting scheme will result in at least three dust parameters for each of the 5000 spectra in the data set.

This large collection of separately fitted parameters makes it difficult to compose definitive statements concerning the global value of the emissivity index or the subtleties of cold dust. The fitted values may suffer from a low signal-to-noise ratio (SNR) and they ignore correlations with neighboring spectra. While averaging many spectra together will increase the SNR of the average spectrum, this process also washes out any variations between the spectra.

These three concerns — fitting the data globally, enhancing the data's SNR, and maintaining

the data's spectral variations — have led us to employ the method of Principal Component Analysis (PCA). The goal of PCA is to find a new coordinate system in which only a few basis spectra are needed to describe most of the data in all its variations. By successfully modeling these few spectra we are actually modeling the entire data set. The basis spectra are linear combinations of the original data, so the SNR of these spectra are very high. In the following sections and chapters we explain how PCA was applied to the data and how the resulting basis vectors were modeled.

7.2 Analysis

PCA is a tool used in multivariate data analysis to find which linear combinations of variates describe most of the data. In this way we can determine if there exists a simpler expression for the data which, while retaining all of the information in the data, provides an easier method of analysis. PCA is described in books on multivariate statistics [Anderson 84], [Morrison 76], and has been applied many ways in astronomy (most recently by [Mathis 92] and [Francis 92]). For an extensive bibliography and fine presentation consult [Murtagh 87]. Here we present the geometrical interpretation of PCA as it relates to our data.

Our data consist of M spectra each containing N frequency bins. This set can be thought of as describing a cloud of M points in an N-dimensional frequency space. Although the data live in an N-dimensional space, each with a coordinate along each of the N-axes, the points may restrict themselves to variations within a small neighborhood or subspace. This subspace can be described by a set of preferred axes, which are rotations of the original axes, along which the points most commonly wander. The objective of PCA is to identify the orthogonal set of these preferred directions and then use them to reparameterize the data.

PCA first finds the direction along which the data vary the most by minimizing the distance between the new axis and the data points. Once this axis, or spectral component, is determined, the data points are projected onto it. The map of these projections make up the spatial component dual to this spectral component. The data points now live in an $(N-1)$ dimensional space and the process is repeated to find the next pair of spectral and spatial components under the constraint that they be orthogonal to the first pair. When we have exhausted all the dimensions available to us, we have a new set of orthogonal N-dimensional axes, determined

from the data, which are ordered according to how valuable they are in representing the data.

To implement this analysis, we must cast our data into matrix form. We create a mapping which transforms the two-dimensional sky position into a one-dimensional pixel number. All the subsequent pixel dependent information is put back on the sky with the inverse mapping. For our M pixels and N frequencies, we now refer to the data set as an $M \times N$ matrix $\mathbf{S}$ and take advantage of all the magic of matrix algebra. Letting $\mathbf{A} = \mathrm{diag}(1/\sqrt{\eta_1}, 1/\sqrt{\eta_2}, \ldots, 1/\sqrt{\eta_M})$ where η_i is the number of observations in pixel i, and $\mathbf{B} = \mathrm{diag}(\delta_1, \delta_2, \ldots, \delta_N)$ where δ_j is the nominal detector noise for frequency bin j, we scale the data to unit detector noise by defining

$$\mathbf{Z} = \mathbf{A}^{-1}\mathbf{S}\mathbf{B}^{-1} \tag{7.1}$$

This scaling takes the data into a signal-to-noise space so that large fluctuations due to detector noise are de-emphasized. We are not actually dividing by the true uncertainties in the data, only by those due to detector noise. The other uncertainties in the data (PTP, PUP, PEP) are taken into account when we try to fit a physical model to the resulting principal components.

The spectral and spatial components of the data set are based on the eigenvectors of the spectral and spatial correlation matrices of the data set. These eigenvectors and their associated eigenvalues, are determined by the method of Singular Value Decomposition (SVD). SVD is an matrix decomposition algorithm which allows us to represent $\mathbf{Z}$ by

$$\mathbf{Z} = \mathbf{U}\mathbf{W}\mathbf{V}^T \tag{7.2}$$

where the $M \times N$ matrix $\mathbf{U}$ contains the spatial eigenvectors, or eigenmaps, in its columns, the $N \times N$ matrix $\mathbf{V}$ contains the spectral eigenvectors, or eigenspectra, in its columns, and the $N \times N$ matrix $\mathbf{W} = \mathrm{diag}(\sqrt{\lambda_1}, \sqrt{\lambda_2}, \ldots, \sqrt{\lambda_N})$ where the λ's are the eigenvalues of the decomposition. SVD is just a short cut to solving the two eigenvalue problems

$$\mathbf{Z}^T\mathbf{Z}\mathbf{V} = \mathbf{V}\mathbf{\Lambda} \qquad \mathbf{Z}\mathbf{Z}^T\mathbf{U} = \mathbf{U}\mathbf{\Lambda} \tag{7.3}$$

where the $N \times N$ matrix $\mathbf{\Lambda} = \mathrm{diag}(\lambda_1, \lambda_2, \ldots, \lambda_N)$. Both eigenvector matrices are orthonormal so that $\mathbf{V}^T\mathbf{V} = \mathbf{I}$ and $\mathbf{U}^T\mathbf{U} = \mathbf{I}$. With this normalization, the ordered eigenvalues in $\mathbf{W}$ measure how much signal resides in each dual pair of eigenvectors. $\mathbf{S}$ is now represented by

$$\mathbf{S} = \mathbf{A}\mathbf{Z}\mathbf{B} = \mathbf{A}\mathbf{U}\mathbf{W}\mathbf{V}^T\mathbf{B} \tag{7.4}$$

We will refer to the eigenvectors transformed back into the space of physical units as components. Thus we have **AU** as our spatial components and **BVW** as our spectral components where we have chosen **W** to scale the spectral components.

Since the goal of this analysis is to use the components to fit physical models to the data we need to derive the uncertainties of the components. The eigenspectra are related to the original spectra by

$$\mathbf{V} = \mathbf{B}^{-1}\mathbf{S}^{T}\mathbf{A}^{-1}\mathbf{U}\mathbf{W}^{-1} \tag{7.5}$$

Thus their errors are given by

$$\sigma^2(V_{ij}) = \sum_{k=1}^{M} \frac{\sigma^2(S_{ki})U_{kj}^2}{B_{ii}^2 A_{kk}^2 W_{jj}^2} \tag{7.6}$$

This error determination for the eigenspectra may be a bit naive. It rests on the assumption that there are no uncertainties in **U** and **W** so that the errors in **V** are solely a linear combination of the errors in our data **S**. A more rigorous treatment would start with characteristic equation

$$\left|\mathbf{Z}^{T}\mathbf{Z} - \lambda\mathbf{I}\right| = \mathbf{0} \tag{7.7}$$

to determine how the eigenvalues $\lambda_i (= W_{ii}^2)$ depend on $\mathbf{Z}^T\mathbf{Z}$. Once this relation is found, and it is certainly beyond the capabilities of this author to find it, the uncertainties in the data can be propagated through to uncertainties in **W**. These can be taken as the source of error in the decomposition, or one could try to propagate them through to uncertainties in the eigenspectra.

In the above derivation, the total amount of error in the data ends up in the eigenspectra, with no amount being attributed to either the eigenvalues or the eigenmaps. Although lacking rigor, these derived eigenspectra errors can be viewed as reasonable estimates of the uncertainties.

The SVD representation of **S** is exact. All we have done is cast the data into a different N-dimensional space. The utility of PCA is judged by how many of these dimensions, or components, can be ignored. If we can show that there are only r components, where $r \ll N$, which contain all of the signal, with the latter $(N-r)$ components containing only noise, we can discard these noise components from our analysis. In terms of dimensionality we have reduced the number independent basis vectors of the data from N down to r.

For the purpose of illustration we have performed PCA on the low frequency data set LLSS for data with $|b| > 20^\circ$. With this galactic cutoff the number of pixels is 3475 and the number

of frequencies is 32. The only physical signals we expect to see are due to the CBR monopole, CBR dipole, and thermal emission from galactic dust. This allows for easier interpretation in chapter 8 . For this simple case we take the data uncertainty to be only due to detector noise so that $\sigma^2(S_{ki}) = \delta_i^2/\eta_k = B_{ii}^2 A_{kk}^2$. From equation 7.6 our component errors are now given by

$$\sigma^2(V_{ij}) = \sum_{k=1}^{M} \frac{\sigma^2(S_{ki})U_{kj}^2}{B_{ii}^2 A_{kk}^2 W_{jj}^2} = \sum_{k=1}^{M} \frac{B_{ii}^2 A_{kk}^2 U_{kj}^2}{B_{ii}^2 A_{kk}^2 W_{jj}^2} = \sum_{k=1}^{M} \frac{U_{kj}^2}{W_{jj}^2} = \frac{1}{W_{jj}^2} = \frac{1}{\lambda_j} \tag{7.8}$$

since $\mathbf{U}^T\mathbf{U} = \mathbf{I}$. This shows the elegant relationship of the component uncertainties to the component eigenvalues.

The are several methods of determining which components one needs to retain to achieve a good description of the data. The quickest method of component determination involves just examining a plot of the eigenvalue spectrum of the decomposition. The eigenvalues have the units of χ^2. To see this, suppose that the data set $\mathbf{S}$ has no signal in it, it just has detector noise in each spectral point in each pixel. So the χ^2 for this data set is given by

$$\begin{aligned}
\chi^2 &= \sum_{i=1}^{M}\sum_{j=1}^{N} \frac{S_{ij}^2}{\sigma_{ij}^2} = \sum_{i=1}^{M}\sum_{j=1}^{N} Z_{ij}^2 = \sum_{i=1}^{M}\sum_{j=1}^{N} Z_{ji}^T Z_{ij} = \sum_{j=1}^{N} (\mathbf{Z}^T\mathbf{Z})_{jj} = \mathrm{tr}(\mathbf{Z}^T\mathbf{Z}) \\
&= \mathrm{tr}\left(\left[\mathbf{U}\mathbf{W}\mathbf{V}^T\right)\right]^T \left[\mathbf{U}\mathbf{W}\mathbf{V}^T\right]\Big) = \mathrm{tr}\left(\mathbf{V}\mathbf{W}\mathbf{U}^T\mathbf{U}\mathbf{W}\mathbf{V}^T\right) = \mathrm{tr}\left(\mathbf{V}\mathbf{W}^2\mathbf{V}^T\right) \\
&= \mathrm{tr}\left(\mathbf{W}^2\mathbf{V}^T\mathbf{V}\right) = \mathrm{tr}\left(\mathbf{W}^2\right) = \mathrm{tr}\left(\mathbf{\Lambda}\right) = \sum_{i=1}^{N} \lambda_i
\end{aligned} \tag{7.9}$$

where we have utilized the theorem that if $\mathbf{A}$ and $\mathbf{B}$ are two matrices then $\mathrm{tr}(\mathbf{AB}) = \mathrm{tr}(\mathbf{BA})$. From equation 7.9 we see that the eigenvalues have units of χ^2 and that their sum yields the total χ^2 for the $M \times N$ degrees of freedom (DOF). When signal *is* present in the data and we model it exactly, the same total amount of χ^2 will result.

Examining the spectrum of the LLSS eigenvalues in figure 7-1 we can see the only the first several eigenvalues have values far greater than the majority of points which are assumed to be noise terms. A more refined method of component determination examines the χ^2/DOF as a function of eigenvalue index. In figure 7-2 we plot

$$\frac{\sum_{i=r}^{N} \lambda_i}{\mathrm{DOF}} \qquad \text{for} \quad r = 1, \ldots, N \tag{7.10}$$

The plot shows how the smaller eigenvalues account for more and more of the noise in the data and that their sum approaches $\chi^2/\mathrm{DOF} \approx 1$. From this plot we can determine how many components we need to retain to achieve an appropriate value for the reduced χ^2.

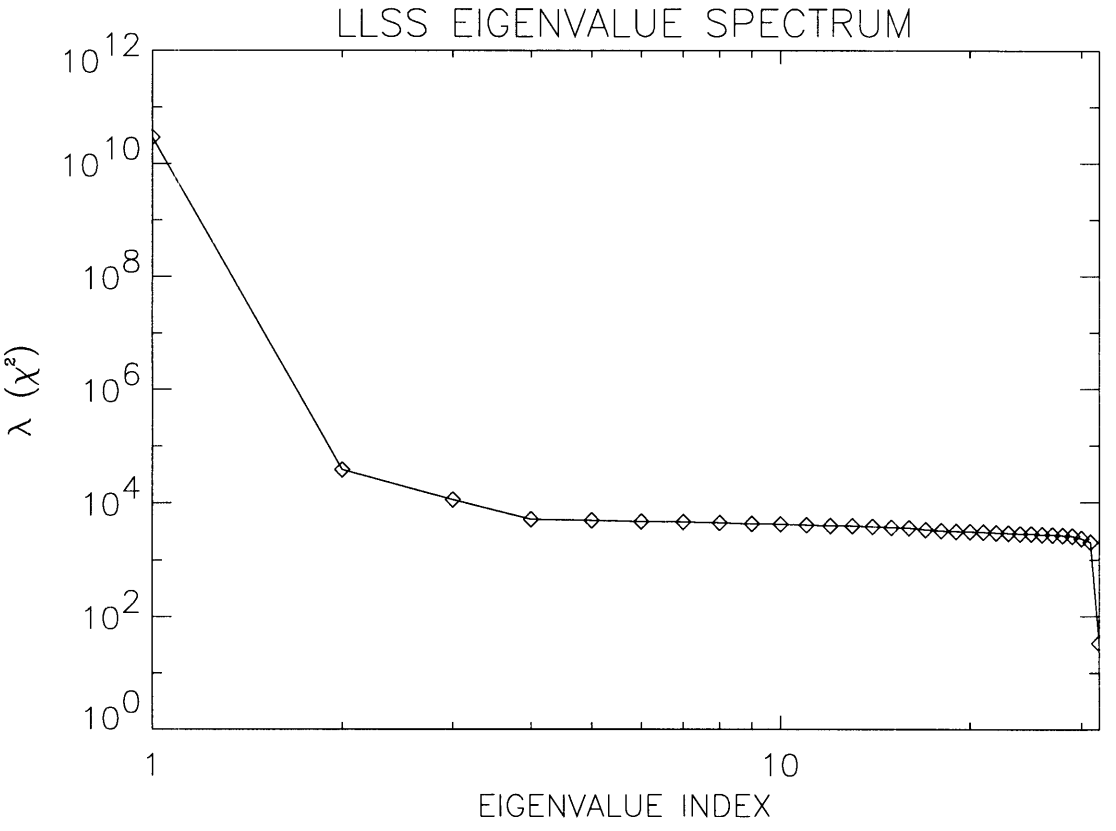

Figure 7-1: Eigenvalue spectrum for LLSS

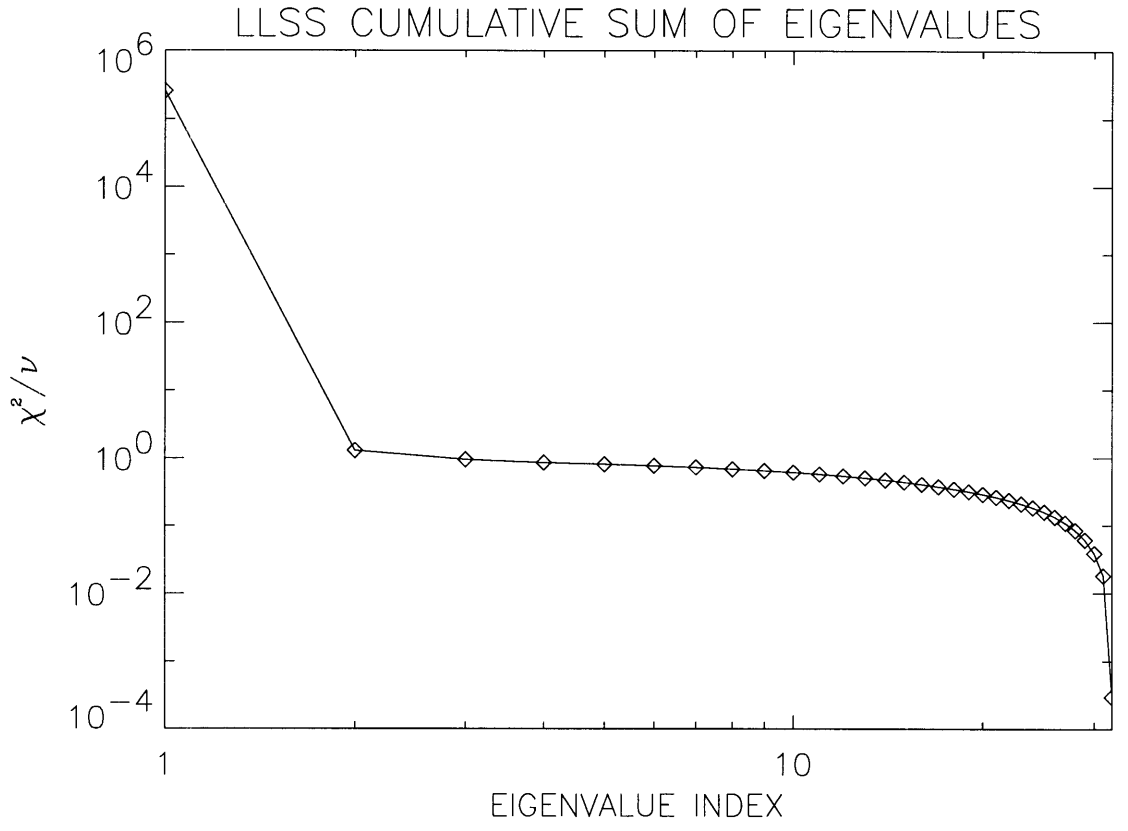

Figure 7-2: Plot of $\sum_{i=r}^{N} \lambda_i$/DOF *vs.* eigenvalue index r for LLSS

The best method for choosing which components contain useful information is to *look* at them. Examining the the first four spectral components for LLSS in figure 7-3 we see that only the first 3 components have discernable physical signal. The plots for components 3 and 4 are on the same scale, but only component 3 has anything resembling signal in it. Compared to the first two components, component 3 has a larger amount of scatter to the size of its signal indicating that noise plays a larger role in it. Component 4 is void of any continuum emission and its periodicity is characteristic of the apodization process. This highlights PCA's ability to pick out not only physical signals but also systematic effects in the data. The high value of χ^2 in this component is merely an artifact of the ordering of the eigenvalues. The last components have individual χ^2's which are low, so that, taken as a group, these noisy components do indeed contain the expected total value of χ^2.

The corresponding spatial components are given in figures 7-4 – 7-7 and indicate that there are clear signals in components 1, 2 and 3, although spatial component 3 again shows significantly more noise than the other two. The blank portions of the figures show the regions where we have excluded data ($|b| < 20^\circ$) or where no data were available. In figure 7-7 we have plotted not the spatial *component* ($= \mathbf{AU}$) but the *eigenmap* ($= \mathbf{U}$) associated with component 4 to bring out its noisy nature. In this way we see exactly what the SVD algorithm detected when it made its determination of this component. Viewing the components suggests that only the first three pairs of spatial and spectral components are necessary to describe this data set. These three components indicate that only three independent processes are responsible for the signal in the data. This is valuable statement to be able to make regarding *any* data set.

For the galactic data treated later, the most sensitive method of component determination is to concentrate on the spatial components. If a spatial component has structure along the galactic plane then the spectral component must have a related galactic signal in it. In fact this method was extremely useful in exploratory data analysis because even when the spectral components showed noise, the maps showed structure indicative of the scan pattern, telling us there were systematic instrumental problems in the data which had survived the calibration procedure. Subtler systematic errors were found by looking for rogue pixels in the first few components which were more than 3σ above their neighbors. Since the pixelization scheme

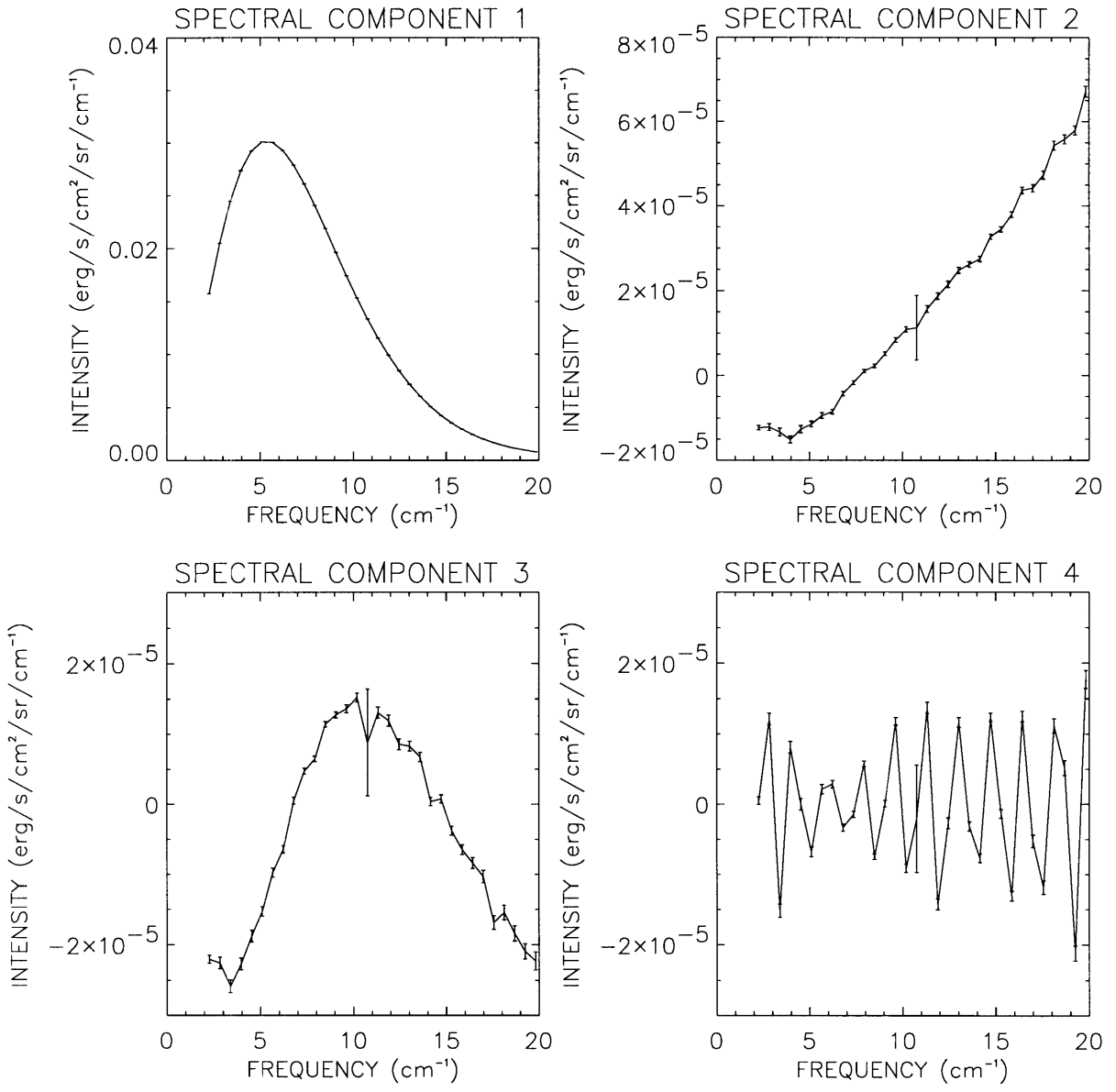

Figure 7-3: First 4 spectral components for LLSS

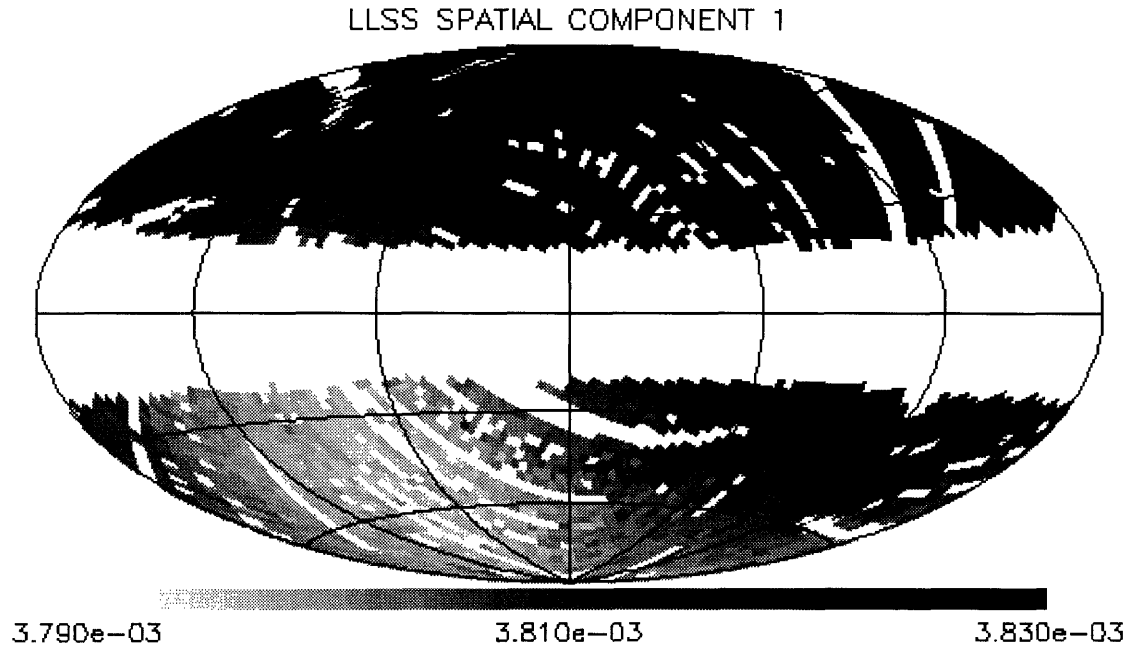

Figure 7-4: LLSS spatial component 1

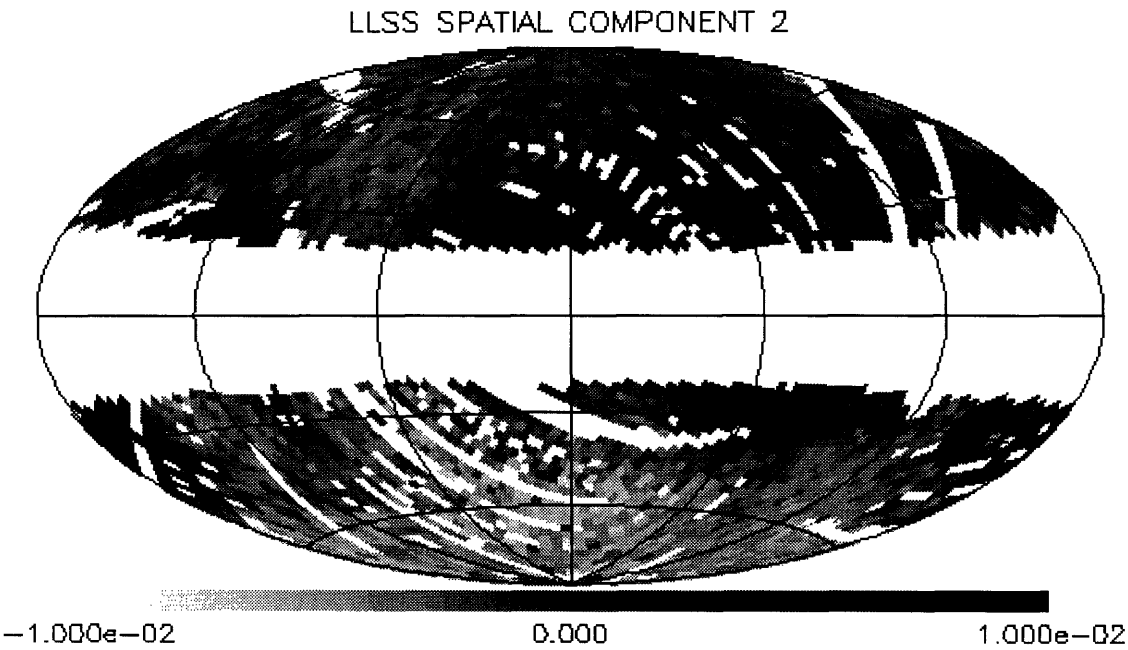

Figure 7-5: LLSS spatial component 2

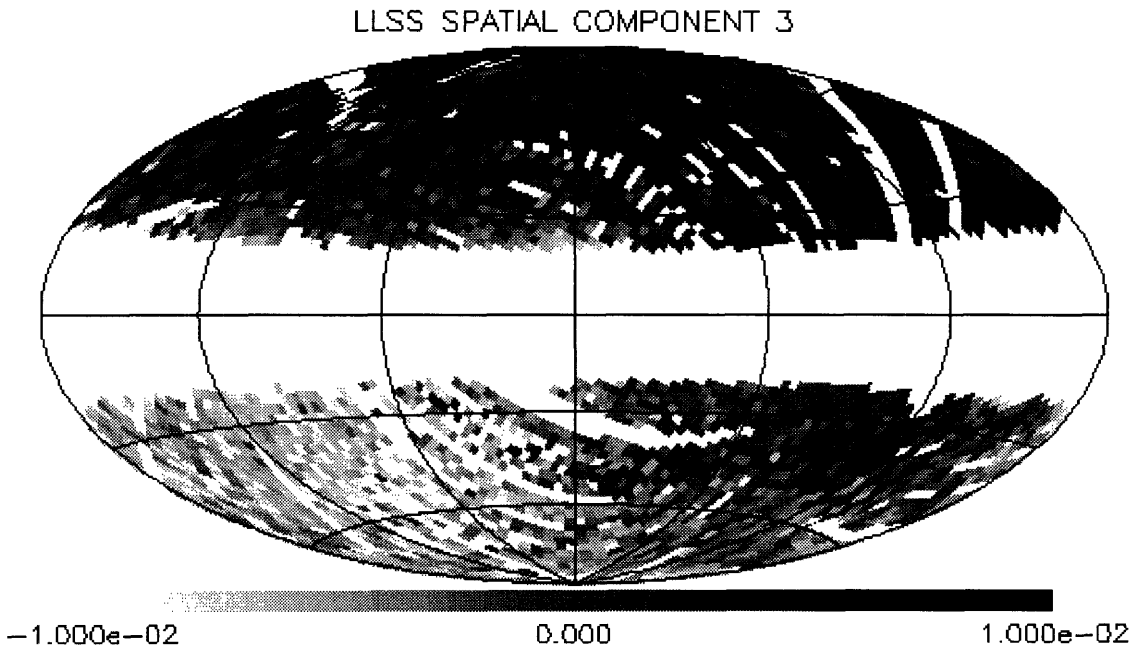

Figure 7-6: LLSS spatial component 3

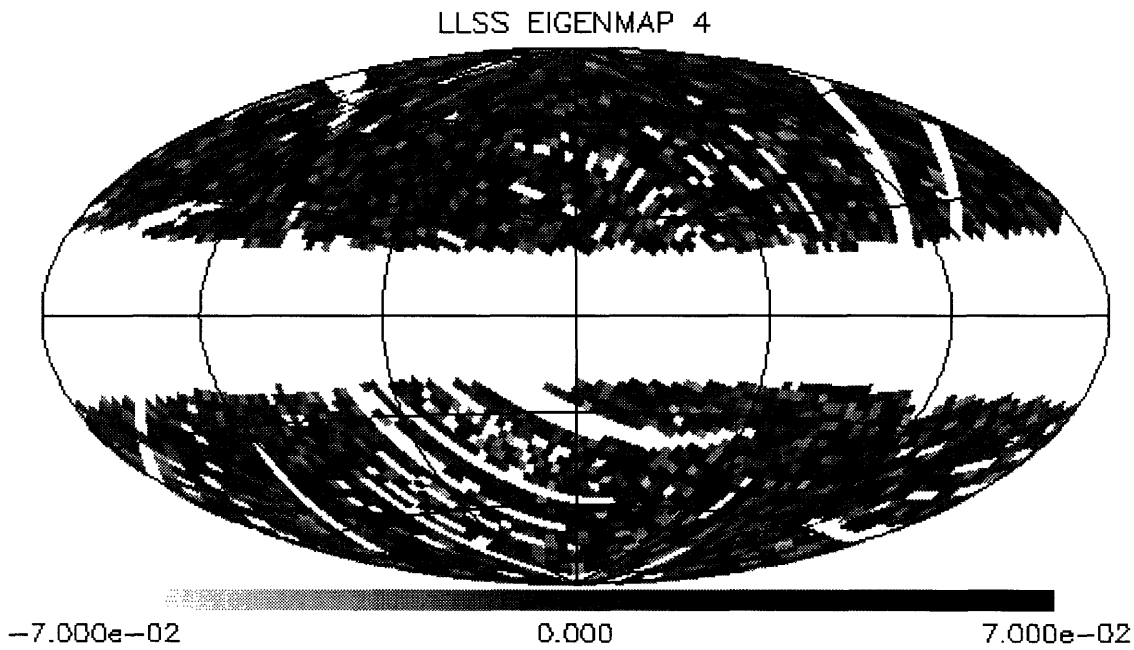

Figure 7-7: LLSS eigenmap 4

oversamples the data, the physical beamwidth is a few pixels across. If a physical signal is present, then it is present in more than one pixel, so that a lone hot pixel must be due to a systematic error in the processing. A first look at the RHSS data indicated that ~ 20 pixels were suspect. Cutting these pixels out of the data significantly decreased the number of prominent components.

By examination of these first several components we determine how many contain most of the useful information. Except for the first few components, the majority look like noise. With no discernible signal in evidence beyond a certain component with index r, we split the data into two pieces

$$\mathbf{S} = \mathbf{S}_s + \mathbf{S}_n = \mathbf{A}\mathbf{U}_s\mathbf{W}_s\mathbf{V}_s^T\mathbf{B} + \mathbf{A}\mathbf{U}_n\mathbf{W}_n\mathbf{V}_n^T\mathbf{B} \tag{7.11}$$

where the subscripts s and n refer to *signal* and *noise* respectively. The matrices $\mathbf{U}_s, \mathbf{V}_s$, and $\mathbf{W}_s$ have dimensions $M \times r, N \times r$, and $r \times r$ and contain the first r spatial and spectral eigenvectors and their corresponding eigenvalues. In a similar fashion $\mathbf{U}_n, \mathbf{V}_n$, and $\mathbf{W}_n$ have dimensions $M \times (N-r), N \times (N-r)$, and $(N-r) \times (N-r)$ and contain the remaining eigenvectors and eigenvalues.

We test whether $\mathbf{S}_n$ is consistent with noise by calculating the reduced χ^2 for this part of the data, assuming a model of zero signal. In our example we have determined that the signal resides in components 1, 2 and 3 so that components 4 through 32 contain only noise. The χ^2 for these noise components is given by the sum of their eigenvalues

$$\chi_n^2 = \sum_{i=1}^{M}\sum_{j=1}^{N}\frac{S_{n_{ij}}^2}{\sigma^2(S_{ij})} = \sum_{i=r+1}^{N}\lambda_i = \sum_{i=4}^{32}\lambda_i = 94615 \tag{7.12}$$

To calculate the the number of degrees of freedom (DOF) involved in these components, we must look at the algorithm that determined them. Since we have M pixels and N frequencies, the first eigenmap contains $M-1$ DOF and the first eigenspectrum contains $N-1$ DOF since both eigenvectors must satisfy a normalization constraint. There is an additional DOF contained in the first eigenvalue. The next set of eigenvectors each contain one less DOF due to the orthogonality constraint. Proceeding in this manner the number of DOF in the kth component is given by

$$\mathrm{DOF}(U_k) = M - k \quad \mathrm{DOF}(V_k) = N - k \quad \mathrm{DOF}(W_k) = 1 \tag{7.13}$$

so that the total DOF in the decomposition is given by

$$\sum_{k=1}^{N} \mathrm{DOF}(U_k) + \mathrm{DOF}(V_k) + \mathrm{DOF}(W_k) = \sum_{k=1}^{N} (M-k) + (N-k) + 1 = M \times N \qquad (7.14)$$

With $M = 3475$ and $N = 32$ the total DOF contained in components $4 - 32$ is 100688. Thus the noise components have $\chi_n^2/\mathrm{DOF} = .94$, which tells us that they contain only noise. Since these components describe only noise in the data set, we will no longer concern ourselves with them. The χ^2/DOF is lower than expected indicating that the estimate of the detector noise is too large.

We now concentrate on the first r components. They are the basis vectors which span the subspace which describes the data to within noise limits. We have reduced our problem from describing data in $M \times N$ dimensions to describing data in $r \times (M + N)$ dimensions. We now drop the subscript s and our matrices now refer to those whose r columns relate to our r components.

Chapter 8

Component Modeling

So far we have mathematically isolated most, if not all, of the data's physical signals into the first few components of the data set. But PCA has done this without any regard to the different physical processes involved in producing them. Inherent in the PCA decomposition are two processes, orthogonalization and rotation, that mix up the different physical processes among all the components. Looking at component 1 in our example we see its spectrum dominated by the Planck curve due to the CBR monopole and its map showing not only the monopole, evidenced by the rather constant level of the color bar, but also the dipole. Component 2's spectra shows something akin to dust emission, while its map contains not only galactic signatures but also a large number of negative values indicating the presence of a negative monopole. PCA is strictly a mathematical device. The trick now is to extract the physics.

In our example the three evident physical processes are the CBR monopole, the CBR dipole, and thermal emission from galactic dust. The models for these processes are given by

$$I_{\rm mono}(\nu, l, b) = B_\nu(T_{\rm cbr}) \tag{8.1}$$

$$I_{\rm dip}(\nu, l, b) = \cos\theta \left.\frac{\partial B_\nu(T)}{\partial T}\right|_{T_{\rm cbr}} dT \tag{8.2}$$

$$I_{\rm dust}(\nu, l, b) = \tau(l, b) \left(\frac{\nu}{\nu_0}\right)^\alpha B_\nu(T_{\rm dust}) \tag{8.3}$$

which show their dependence on position, given in galactic coordinates (l, b), and frequency ν. The monopole is taken to be constant across the sky and has a spectrum consistent with a Planck function. The dipole emission arises from the Doppler shift of the CBR due to the

Sun's motion with respect to the frame of the monopole. The angle θ is the angle between the line of sight (l, b) and the hot spot of the dipole (l_0, b_0). The dipole amplitude is dT. The spectrum of the dust is given by a Planck function at the dust temperature $T_{\rm dust}$ multiplied by the emissivity law $(\nu/\nu_0)^\alpha$ where α is the emissivity index. The empirical template $\tau(l, b)$ accounts for the variations in the dust optical depth as a function of position.

In chapter 6 we used the template method and determined the monopole temperature to be $T_{\rm cbr} = 2.72567 \pm .00001\,{\rm K}$, and the dipole amplitude to be $dT = 3.319 \pm .008\,{\rm mK}$ with a hot spot located at $(l_0, b_0) = (264.4^\circ \pm 0.3^\circ\ , 48.4^\circ \pm 0.5^\circ\ )$ [Kogut 93]. Using an optical depth template taken from the total integrated power in the high frequency channel (which is dominated by dust emission) , the galactic dust temperature was found to be $T_{\rm dust} = 13.89 \pm .76\,{\rm K}$ with α fixed at 1.5 for data with $|b| > 20^\circ$. This chapter will show how to use either the spectral or the spatial components to derive these physical parameters.

8.1 Spectral Component Modeling

SVD has given us r spectral components $\mathbf{BV}$ describing the data which span a subspace of the N dimensional frequency space. We want to determine an equivalent number of physical components which best span the same subspace. Even if we know the correct physical models, a problem arises in that, most likely, these models do not look anything like the components. In order to quantitatively compare the two we need to understand the constraints satisfied by the components and construct the physical models accordingly.

Since we have r eigenspectra in the columns of $\mathbf{V}$, we must have r physical models arrayed in our model matrix $\mathbf{C}_\nu(\vec{p})$ where $\vec{p}$ is a vector containing the model parameters. The number of rows in $\mathbf{C}$ match the number of frequencies N and the models are given in units of erg $\rm s^{-1}$ $\rm cm^{-2}$ $\rm ster^{-1}$ cm. Since the eigenspectra are determined in a space in which we have divided out the frequency dependent detector noise, the models also must be cast into this space by premultiplying with the detector noise matrix $\mathbf{B}$ defined in the previous chapter. In this space the eigenspectra are orthogonal so we must also orthogonalize the models. Even if the orthogonalized models and the eigenspectra span the same noise normalized space, they

may still differ by a rotation. Thus our spectral model of $\mathbf{V}$ is described by the matrix

$$\mathbf{D}_\nu(\vec{p},\vec{\theta}) = \mathbf{B}^{-1}\mathbf{C}_\nu(\vec{p})\mathbf{F}(\vec{p})\mathbf{G}(\vec{\theta}) \tag{8.4}$$

where premultiplication by $\mathbf{B}^{-1}$ casts our physical model $\mathbf{C}$ into the dimensionless units of $\mathbf{V}$, the matrix $\mathbf{F}$ orthogonalizes the matrix $\mathbf{B}^{-1}\mathbf{C}$, and $\mathbf{G}$ performs the rotation that accounts for the mixing of physical signals among the eigenspectra. $\mathbf{G}$ is only necessary when the number of components is greater than one.

Another way to look at $\mathbf{G}(\vec{\theta})$ is to consider that two sets of basis vectors, in this case $\mathbf{V}$ and $\mathbf{D}$, that span the same space may differ from each other by a rotation in that space. To describe a rotation in r dimensions we need the $r(r-1)/2$ angles contained in the vector $\vec{\theta}$. Thus $\mathbf{G}(\vec{\theta})$ is the product of $r(r-1)/2$ r-dimensional rotations

$$\mathbf{G}(\vec{\theta}) = \prod_{i=1}^{r(r-1)/2} \mathbf{G}_i(\theta_i) \tag{8.5}$$

where $\mathbf{G}_i$'s refer to the $r(r-1)/2$ Givens matrices of order r and θ_i are the individual angles of rotation. The general form of a Givens matrix $\mathbf{G}_{ab}$ of order r is an identity matrix except for four elements: $g_{aa} = g_{bb} = \cos\theta_{ab}$ and, for $a > b$, $-g_{ab} = g_{ba} = \sin\theta_{ab}$ [Searle 82].

Since $\mathbf{G}$ is a rotation and $\mathbf{F}$ orthogonalizes the matrix product $\mathbf{B}^{-1}\mathbf{C}$, then $\mathbf{D}$ becomes orthogonal by construction

$$\mathbf{D}^T\mathbf{D} = \mathbf{G}^T(\mathbf{B}^{-1}\mathbf{C}\mathbf{F})^T(\mathbf{B}^{-1}\mathbf{C}\mathbf{F})\mathbf{G} = \mathbf{G}^T\mathbf{G} = \mathbf{I} \tag{8.6}$$

We are thus modeling the orthogonal eigenspectra with orthogonal spectral models. Once we have successfully fit for the spectral parameters $\vec{p}$ and the rotational parameters $\vec{\theta}$ in $\mathbf{D}_\nu(\vec{p},\vec{\theta})$ the model for the data set is given by

$$\mathbf{M}(\vec{p},\vec{\theta}) = \mathbf{AUWD}_\nu(\vec{p},\vec{\theta})^T\mathbf{B} = \mathbf{AUWG}(\vec{\theta})^T\mathbf{F}(\vec{p})^T\mathbf{C}_\nu(\vec{p})^T \tag{8.7}$$

We see that the spatial extent of the spectral models in $\mathbf{C}$ are contained in

$$\mathbf{P}(\vec{p},\vec{\theta}) = \mathbf{AUWG}(\vec{\theta})^T\mathbf{F}(\vec{p})^T \tag{8.8}$$

which can thus be used to check if the spatial character of these emission processes makes sense.

Following equation 8.4 we fit the three significant spectral components given in figure 7-3 to the following spectral models

$$C_{\rm mono}(\nu) = B_\nu(T_{\rm cbr}) \tag{8.9}$$

$$C_{\rm dip}(\nu) = \left.\frac{\partial B_\nu(T)}{\partial T}\right|_{T_{\rm cbr}} \tag{8.10}$$

$$C_{\rm dust}(\nu) = \left(\frac{\nu}{\nu_0}\right)^{1.5} B_\nu(T_{\rm dust}) \tag{8.11}$$

using the Levenberg-Marqurdt algorithm and weighting each eigenspectrum by its eigenvalue. The resulting physical and rotational parameters are

$$T_{\rm cbr} = 2.726 \pm .017\,{\rm K} \tag{8.12}$$

$$T_{\rm dust} = 18.41 \pm .56\,{\rm K} \tag{8.13}$$

$$\vec{\theta} = \begin{bmatrix} -1.76(-3) \\ 3.39(-4) \\ -1.50(-1) \end{bmatrix} \pm \begin{bmatrix} 3.77(-3) \\ 4.94(-3) \\ 5.25(-3) \end{bmatrix} \tag{8.14}$$

$$\chi^2_s = 673 + 77 + 94 = 844 \tag{8.15}$$

where we have summed over the χ^2 for the individual components. The number of DOF contained in these three spectral components is given by equation 7.13 to be 31, 30, and 29 respectively. The χ^2 are too high since we have ignored that the JCJ errors which come into play when averaging over large regions of the sky. We see that dust temperature does not agree with that determined from the template analysis. This is probably due to the slippery nature of the dust model when we fit to only the Rayleigh-Jeans portion of the dust spectrum. The difference between the two models is $\sim 30\%$ at the higher frequencies where the weight is the lowest.

We use the rotational parameters to form the maps described by equation 8.8 and present them in figures 8-1 – 8-3. We see that the maps do indeed follow the expected signatures of the three physical processes. We can't use these maps directly because we ignore any spatial variations when we fit for spectral parameters. With the spectral models given by the matrix **D** we assume that the spatial models are in fact the spatial components so that the model of the data set is given by

$$\mathbf{M} = \mathbf{AUWD}^T\mathbf{B} \tag{8.16}$$

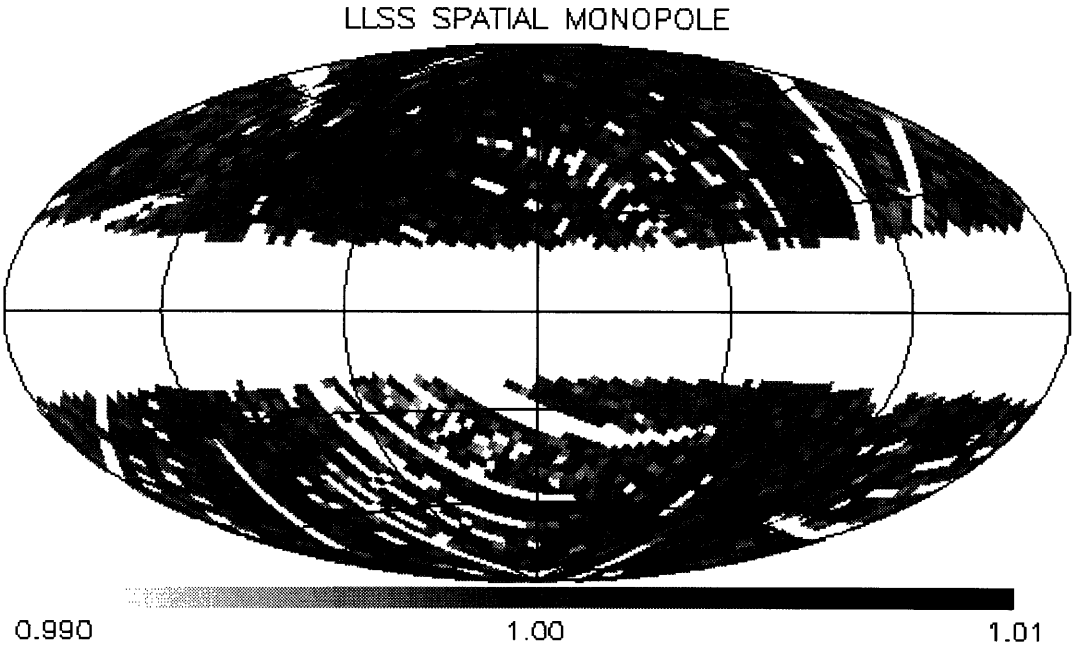

Figure 8-1: Spatial monopole derived from spectral rotational parameters

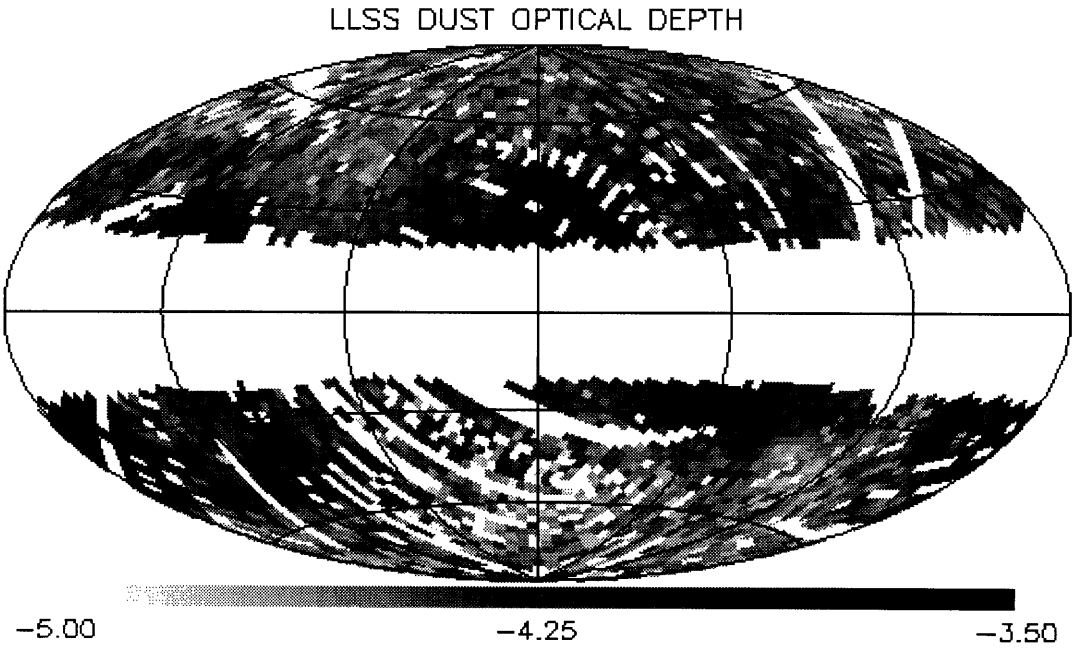

Figure 8-2: Dust optical depth derived from spectral rotational parameters

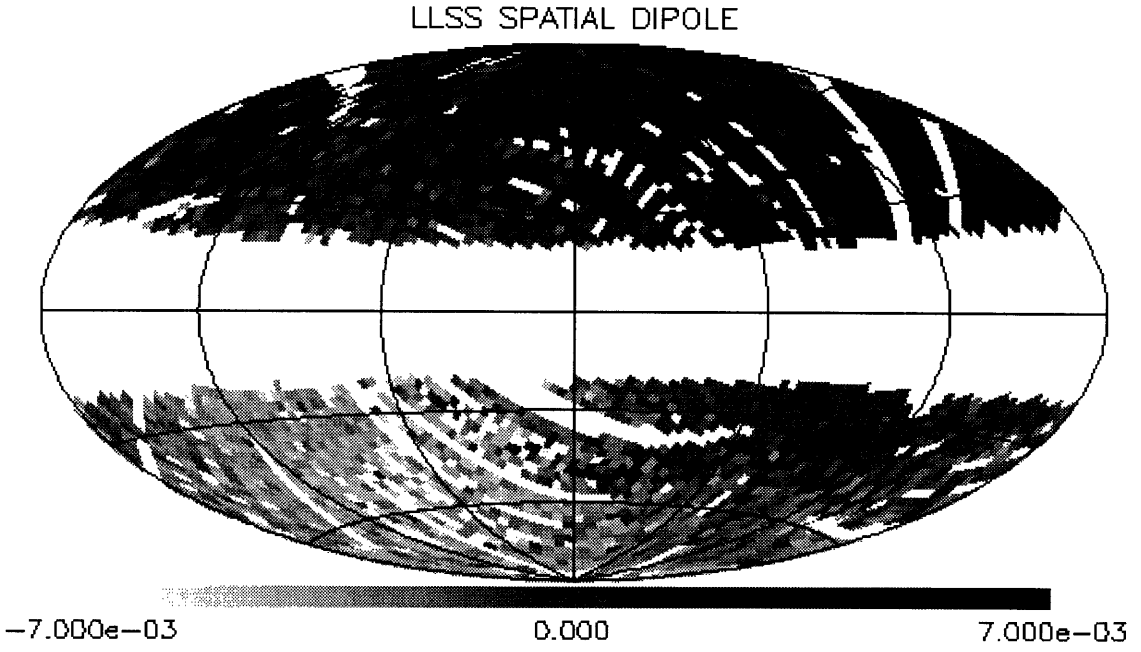

Figure 8-3: Spatial dipole derived from spectral rotational parameters

The χ^2 function thus used to derive the spectral and rotational parameters is

$$\begin{aligned}
\chi^2 &= \sum_{i=1}^{M}\sum_{j=1}^{N}\frac{(S_{ij}-M_{ij})^2}{\sigma_{ij}^2} \\
&= \mathrm{tr}\left(\mathbf{A}^{-1}\left[\mathbf{S}-\mathbf{M}\right]\mathbf{B}^{-2}\left[\mathbf{S}-\mathbf{M}\right]^T\mathbf{A}^{-1}\right) \\
&= \mathrm{tr}\left(\left[\mathbf{U}\mathbf{W}\mathbf{V}^T-\mathbf{U}\mathbf{W}\mathbf{D}^T\right]\left[\mathbf{U}\mathbf{W}\mathbf{V}^T-\mathbf{U}\mathbf{W}\mathbf{D}^T\right]^T\right) \\
&= \mathrm{tr}\left(\left[\mathbf{V}-\mathbf{D}\right]\mathbf{W}^2\left[\mathbf{V}-\mathbf{D}\right]^T\right) \qquad (8.17)
\end{aligned}$$

where the spatial information has been ignored. We can only say that the maps derived with equation 8.8 correspond to our best fit spectral models.

In order to fit for the spatial parameters, we use our best fit spectral models in the template method of [Fixsen 94a]. In chapter 6 we used this linear least-squares method to find the best fit spectra associated with predetermined spatial structures. Here we use it find the best fit spatial coefficients associated with each of the spectral models determined above. This procedure yields a map of coefficients for the monopole spectrum, the dipole spectrum, and the dust spectrum. We then fit for the dipole parameters and the constant of proportionality between our galactic template and the resulting map of the dust optical depth. The monopole

model is taken to be unity across the sky. The fit yields

$$\chi^2_{\rm monopole} = 3220 \tag{8.18}$$

$$\tau_{\rm dust} = 3.85(-2) \pm 1.23(-4) \quad \chi^2_{\rm dust} = 5392 \tag{8.19}$$

$$dT = 3.214 \pm .036\,{\rm mK} \quad (l_0, b_0) = (263.8^\circ \pm 1.1^\circ\,, 47.9^\circ \pm .9^\circ) \quad \chi^2_{\rm dipole} = 3681 \tag{8.20}$$

Since each of these maps has 3475 degrees of freedom, the χ^2 for the monopole and dipole maps are expected. The χ^2 for the dust optical depth map shows that our galactic template generally follows the low frequency dust emission, but not to within statistical error.

8.2 Spatial Component Modeling

The preceeding analysis used the eigenspectra to fit spectral models of emission which were then used to derive their spatial parameters. The duality between the eigenspectra and the eigenmaps allows us to go in the other direction: from fitting spatial models to the eigenmaps to deriving the parameters describing the spectral emission processes. With $\mathbf{P}_x(\vec{p})$, where x denotes spatial dependence, as our matrix of spatial models with spatial parameters $\vec{p}$, we can similarly fit our eigenmaps to the model

$$\mathbf{D}_x(\vec{p},\vec{\theta}) = \mathbf{A}^{-1}\mathbf{P}_x(\vec{p})\mathbf{F}(\vec{p})\mathbf{G}(\vec{\theta}) \tag{8.21}$$

where $\mathbf{A}$ contains the spatially dependent noise and once again $\mathbf{F}$ and $\mathbf{G}$ orthogonalize and rotate $\mathbf{P}$. The model for the data set is now given as

$$\mathbf{M}(\vec{p},\vec{\theta}) = \mathbf{A}\mathbf{D}_x(\vec{p},\vec{\theta})\mathbf{W}\mathbf{V}^T\mathbf{B} = \mathbf{P}_x(\vec{p})\mathbf{F}(\vec{p})\mathbf{G}(\vec{\theta})\mathbf{W}\mathbf{V}^T\mathbf{B} \tag{8.22}$$

We form the spectra corresponding to these spatial models

$$\mathbf{C}(\vec{p},\vec{\theta}) = \mathbf{B}\mathbf{V}\mathbf{W}\mathbf{G}(\vec{\theta})^T\mathbf{F}(\vec{p})^T \tag{8.23}$$

and can thus examine $\mathbf{C}$ for various models of spectral emission.

To model the three physical processes we use a spatial monopole, the dust template determined in chapter 6 from the integral of the high frequency power, and a spatial dipole with its hot spot located at (l_0, b_0). We fit the spatial components given in figures 7-4 – 7-6 for the physical parameters $\vec{p} = (l_0, b_0)$ as well as the three rotational parameters $\vec{\theta}$ of the decomposition and obtain

$$(l_0, b_0) = (265.4^\circ \pm .2^\circ\ , 48.4^\circ \pm .1^\circ\ ) \tag{8.24}$$

$$\vec{\theta} = \begin{bmatrix} -9.50(-4) \\ -2.10(-3) \\ -3.56(-1) \end{bmatrix} \pm \begin{bmatrix} 1.12(-5) \\ 7.26(-6) \\ 4.51(-3) \end{bmatrix} \tag{8.25}$$

$$\chi^2_s = 4226 + 3650 + 3741 = 11617 \tag{8.26}$$

where we have summed over the χ^2 due to each fitted component. The DOF in each map are 3474, 3473, and 3472 indicating that the spatial components are not as susceptible to JCJ errors as the spectral components.

Following equation 8.23, we form the spectra corresponding to these maps and present them in figure 8-4. The spectra show the signals due to the monopole, the galactic template, and the dipole. Since we have merely performed a rotation on the spectral components, the spectral wiggles in component 3 show up as artifacts in the dipole spectrum.

In order to fit for the spectral parameters, we use our best fit spatial models in the template method. As is chapter 6 we fit the resulting three spectra to a Planck function with a residual dust ($T = 20\mathrm{K}, \alpha = 1.5$), a dust model with $\alpha = 1.5$, and a temperature derivative of the Planck function. The derived parameters are

$$T_{\mathrm{cbr}} = 2.72567 \pm .00001\,\mathrm{K} \qquad \frac{\chi^2}{\mathrm{DOF}} = 3.45 \tag{8.27}$$

$$T_{\mathrm{dust}} = 13.98 \pm .77\,\mathrm{K} \quad \tau = 5.48(-2) \pm 6.25(-3) \qquad \frac{\chi^2}{\mathrm{DOF}} = .86 \tag{8.28}$$

$$dT = 3.316 \pm .008\,\mathrm{mK} \qquad \frac{\chi^2}{\mathrm{DOF}} = 1.134 \tag{8.29}$$

and the residuals are given in figure 8-5 In the first fit, the χ^2/DOF is high because we have again neglected the JCJ errors. The dipole fit does not suffer from this problem because during every orbit the FIRAS samples both positive and negative contributions from the dipole. The positive and negative errors due to the bolometer uncertainties thus cancel.

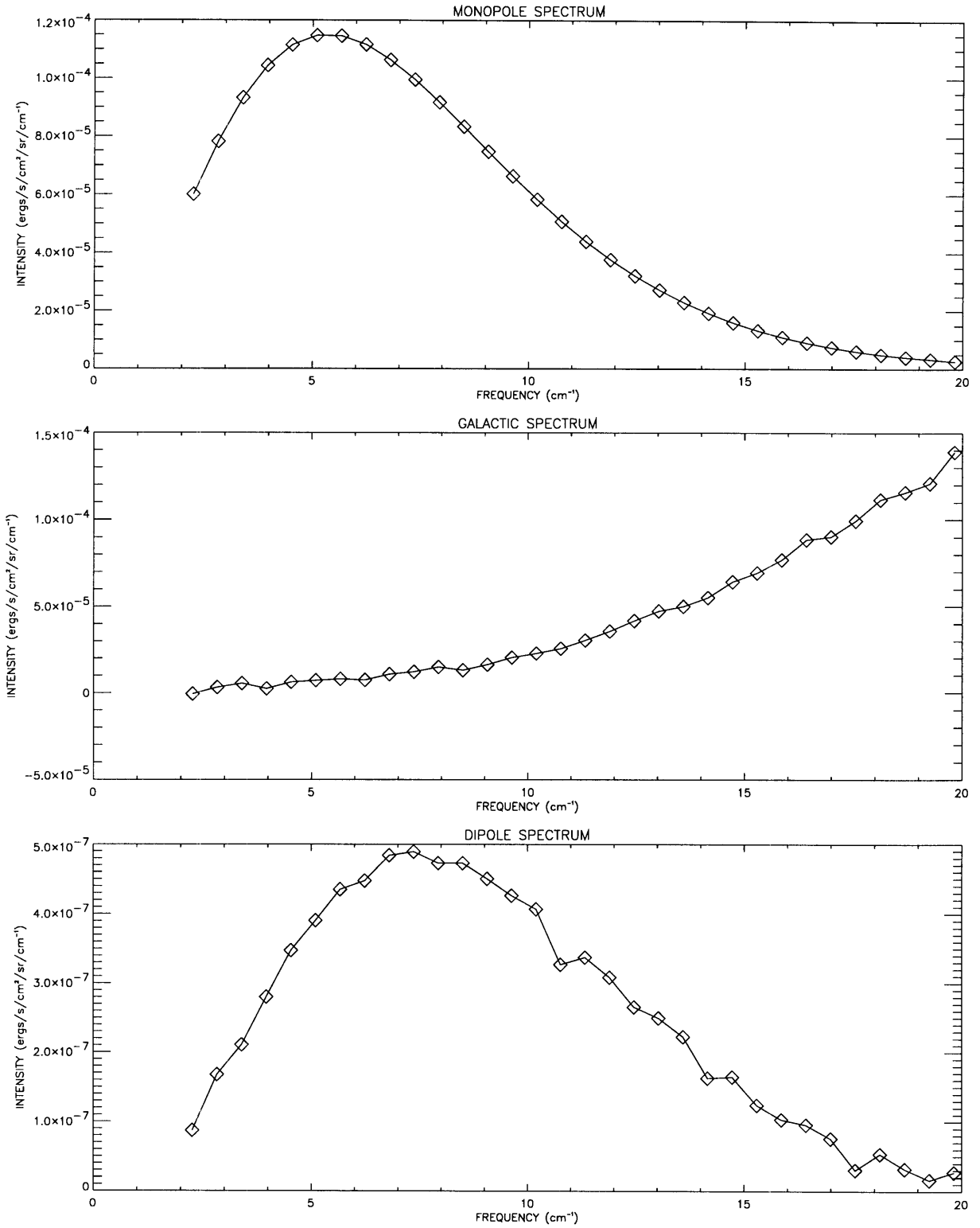

Figure 8-4: Spectra derived from spatial components

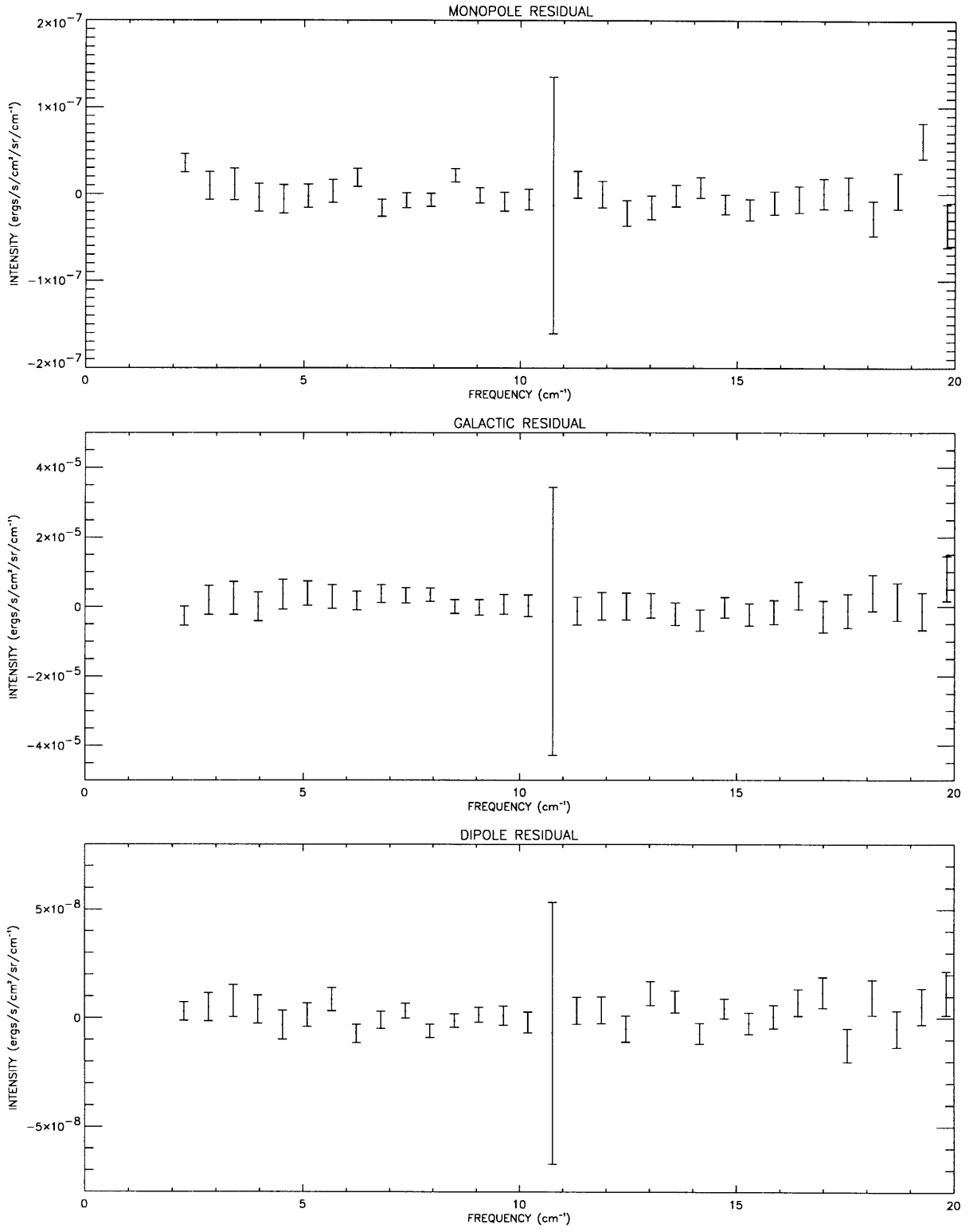

Figure 8-5: Residuals from template spectra

8.3 Comparision of Techniques

In comparing the parameters from modeling the spatial components and from those obtained with the template method we see that they agree very well. This is not surprising since the only difference between the two methods is a $\sim 1^{\circ}$ shift in the hot spot location of the dipole template. While the template method had to assume this location, spatial component modeling was able to determine it. Both methods, however, had to assume a template for the dust emission.

Modeling of the spectral components yields cosmological parameters in agreement with those obtained with the spatial components without having to assume any spatial dependencies. Using spatial component modeling, however, yields better results, in the form of smaller error bars, on both spectral and spatial parameters than when we start with fitting the spectral components. This is due to the fact we are constraining many more degrees of freedom when we model a map (3475 DOF) than when we model a spectrum (32 DOF). Table 8.1 list the characteristics of the three fitting techniques used in this example: template fitting [Fixsen 94b], spatial component modeling, spectral component modeling. When we fit for parameters describing the dust and gas in chapter 9, we have no prior information on how these processes change across the sky. Thus we cannot use either the template or spatial component modeling techniques and must rely solely on the spectral components to examine the physics of dust and gas emission.

Technique	Pros	Cons
template fitting	- small spectral parameter errors	- must assume spatial models and parameters
PCA spatial components	- determines spatial and spectral parameters - small parameter errors	- need spatial models
PCA spectral components	- determines spatial and spectral parameters - do not need spatial models to determine spectral parameters	- parameter errors are larger

Table 8.1: Comparision of fitting techniques

8.4 Model Merging

In our example using the low frequency data set, a dust model with a single temperature adequately described the galactic emission. To better describe the galactic dust emission we must use the high frequency data set at well. But we encounter a problem with having two separate data sets. Since the two sets contain different random and systematic errors, each must be treated separately using PCA. This may, depending on what part of the sky is analyzed, result in a different number of components, and hence a different number of models for each set. In order to fit models over the entire FIRAS frequency range we must figure out how to merge the models for one channel to perhaps a different number of models in the other. The data set with the greatest number of components determines the number of models to be fit over the entire frequency range, with the lower dimensional data set being fit to some linear combination of those models.

In order to derive an expression for this linear combination, let us assume that the low frequency data have fewer components than the high frequency data. If $[\mathbf{H}_l \quad \mathbf{H}_h]^T$ is the model matrix of spectral dust emission partitioned in frequency, we must have $\mathbf{C}_\mathrm{h} = \mathbf{H}_\mathrm{h}$ at high frequency and $\mathbf{C}_\mathrm{l} = \mathbf{H}_\mathrm{l}\mathbf{K}$ at low frequency, where $\mathbf{K}$ is vector which reduces the dimensionality of $\mathbf{H}_l$ down to that of $\mathbf{C}_l$. Similarly, the maps corresponding to the physical structures in the low frequency must be some linear combination of the high frequency maps

$$\mathbf{A}_l\mathbf{U}_l = \mathbf{A}_h\mathbf{U}_h\mathbf{L} \tag{8.30}$$

with $\mathbf{L}$ being the matrix containing the coefficients of the projection. Since we are only fitting spectral models we can use $\mathbf{L}$ (which is based on how the maps from the different data sets project onto each other) to determine $\mathbf{K}$, which specifies how the different sets of spectral models are related.

We can determine $\mathbf{L}$ by calculating the inner product of the high frequency maps with the low frequency maps

$$\mathbf{L} = (\mathbf{A}_h\mathbf{U}_h)^T(\mathbf{A}_l\mathbf{U}_l) \tag{8.31}$$

which is coefficient matrix of the projection of one set of maps onto another. By looking a little deeper we can derive an aid in estimating which components are important.

In order to facilitate the interpretation, we perform the Gram-Schmidt orthogonalization procedure on both sets of maps. Both $\mathbf{U}_l$ and $\mathbf{U}_h$ contain sets of maps whose members are orthogonal among themselves by construction, but they both exist in the statistical space particular to their corresponding data sets. Once we return to physical dimensions, by premultiplying by $\mathbf{A}_l$ and $\mathbf{A}_h$ respectively, the maps are no longer orthogonal. We find the orthogonalizing matrices $\mathbf{Q}_l$ and $\mathbf{Q}_h$ such that

$$\mathbf{R}_l = \mathbf{A}_l\mathbf{U}_l\mathbf{Q}_l \qquad \mathbf{R}_l^T\mathbf{R}_l = \mathbf{I}_l \tag{8.32}$$

$$\mathbf{R}_h = \mathbf{A}_h\mathbf{U}_h\mathbf{Q}_h \qquad \mathbf{R}_h^T\mathbf{R}_h = \mathbf{I}_h \tag{8.33}$$

where $\mathbf{R}_l$ and $\mathbf{R}_h$ contain linearly independent and normalized representations of both sets of maps.

We calculate the inner product $\mathbf{R}_h^T\mathbf{R}_l$ to arrive at the normalized coefficients of the projection. If the components were perfectly noiseless and all of the spatial structure seen at low frequency were contained in the high frequency maps, then the inner product of this matrix with itself would be the identity. Let us define this product to be $\mathbf{T}$ so that

$$\mathbf{T} = (\mathbf{R}_h^T\mathbf{R}_l)^T(\mathbf{R}_h^T\mathbf{R}_l) \tag{8.34}$$

For the noiseless case $\mathbf{T} = \mathbf{I}$. In other words, the low frequency maps exist in the space spanned by the high frequency maps and the sum of the squares of the the coefficients of each map in that space has unit value. We are merely mapping a unit vector from one space into another space. Alas, the components are not noiseless. As we look at each successive component we see that the lesser components, associated with the smaller eigenvalues, get increasingly noisy. When we form $\mathbf{T}$ using real world data, the values along its diagonal measure how much of the signal in the lower dimensional maps can be expressed in the higher dimensional space. If this value is much less than unity, then we can surmise that the component in question has mostly noise in it, which the higher dimensional maps do not reproduce. This is used as an aid in determining which components to retain.

Having found how the high and low frequency spatial components are related through their inner product $\mathbf{L}$, we can use this relationship to determine how the different sets of spectral models are connected. The object to find is $\mathbf{K}$, which projects the higher dimensional spectral

models into the lower dimensional space. To model the low frequency components we have $\mathbf{C}_l = \mathbf{H}_l\mathbf{K}$. With the projection coefficients defined above, we have for the low and high frequency spatial and spectral models

$$\mathbf{M}_l = \mathbf{A}_l\mathbf{U}_l\mathbf{W}_l\mathbf{C}_l^T = \mathbf{A}_h\mathbf{U}_h\mathbf{L}\mathbf{W}_l\mathbf{K}^T\mathbf{H}_l^T \tag{8.35}$$

$$\mathbf{M}_h = \mathbf{A}_h\mathbf{U}_h\mathbf{W}_h\mathbf{G}_h^T\mathbf{F}_h^T\mathbf{C}_h^T = \mathbf{A}_h\mathbf{U}_h\mathbf{W}_h\mathbf{G}_h^T\mathbf{F}_h^T\mathbf{H}_h^T \tag{8.36}$$

where, again, $\mathbf{F}_h$ orthogonalizes the spectral models in $\mathbf{H}_h$, $\mathbf{G}_h$ performs a rotation on the high frequency models, and $\mathbf{K}$ reduces the low frequency spectral models (whose dimension is equal to that of the high frequency models) down to the number of low frequency components. We have also substituted the high frequency map representation of the low frequency maps. The model which includes both low and high frequency models becomes

$$\mathbf{M} = [\mathbf{A}_h\mathbf{U}_h\mathbf{L}\mathbf{W}_l\mathbf{K}^T\mathbf{H}_l^T \quad \mathbf{A}_h\mathbf{U}_h\mathbf{W}_h\mathbf{G}_h^T\mathbf{F}_h^T\mathbf{H}_h^T] \tag{8.37}$$

where we have partitioned the matrix in frequency. Continuity between the two frequency ranges demands that

$$\mathbf{L}\mathbf{W}_l\mathbf{K}^T = \mathbf{W}_h\mathbf{G}_h^T\mathbf{F}_h^T \tag{8.38}$$

so that

$$\mathbf{K} = \mathbf{F}_h\mathbf{G}_h\mathbf{W}_h(\mathbf{L}^{-1})^T\mathbf{W}_l^{-1} \tag{8.39}$$

Since we now know $\mathbf{K}$ we can model the low frequency components $\mathbf{V}_l$ with

$$\mathbf{D}_l = \mathbf{B}^{-1}\mathbf{H}_l\mathbf{K}\mathbf{F}_l \tag{8.40}$$

where $\mathbf{F}_l$ is the matrix which orthogonalizes $\mathbf{B}^{-1}\mathbf{H}_l\mathbf{K}$.

The careful reader may have noticed a problem with above formula for $\mathbf{K}$ in that we are taking the inverse of $\mathbf{L}$, which is not a square matrix but has dimensions of $h \times l$ where h denotes the number of high frequency components and l denotes the number of low frequency components. We again turn to the SVD algorithm to determine the left inverse or pseudoinverse of $\mathbf{L}$

$$\mathbf{L} = \mathbf{\Delta}\mathbf{\Xi}\mathbf{\Upsilon}^T \tag{8.41}$$

where the matrices $\mathbf{\Delta}, \mathbf{\Xi}$, and $\mathbf{\Upsilon}$ satisfy the relations $\mathbf{\Delta}^T\mathbf{\Delta} = \mathbf{I}$, $\mathbf{\Upsilon}^T\mathbf{\Upsilon} = \mathbf{I}$, $\mathbf{\Upsilon}\mathbf{\Upsilon}^T = \mathbf{I}$ and $\mathbf{\Xi}$ is the diagonal matrix containing the eigenvalues of the decomposition. The left inverse of $\mathbf{L}$ becomes

$$\mathbf{L}^{-1} = \mathbf{\Upsilon}\mathbf{\Xi}^{-1}\mathbf{\Delta}^T \quad \text{since} \quad \left(\mathbf{\Upsilon}\mathbf{\Xi}^{-1}\mathbf{\Delta}^T\right)\left(\mathbf{\Delta}\mathbf{\Xi}\mathbf{\Upsilon}^T\right) = \mathbf{I} \tag{8.42}$$

The end result of all the projecting, rotating and orthogonalizing are the models which are to be fit to the eigenspectra. Thus with the high frequency model given by

$$\mathbf{D}_h(\vec{p}, \vec{\theta}) = \mathbf{B}_h^{-1}\mathbf{H}_h(\vec{p})\mathbf{F}_h(\vec{p})\mathbf{G}_h(\vec{\theta}) \tag{8.43}$$

the low frequency model becomes

$$\mathbf{D}_l(\vec{p}, \vec{\theta}) = \mathbf{B}_l^{-1}\mathbf{H}_l(\vec{p})\mathbf{K}(\vec{p}, \vec{\theta})\mathbf{F}_l(\vec{p}, \vec{\theta}) = \mathbf{B}_l^{-1}\mathbf{H}_l(\vec{p})\mathbf{F}_h(\vec{p})\mathbf{G}_h(\vec{\theta})\mathbf{W}_h(\mathbf{L}^{-1})^T\mathbf{W}_l^{-1}\mathbf{F}_l(\vec{p}, \vec{\theta}) \tag{8.44}$$

Elegance has never looked so ugly.

Chapter 9

Results and Interpretation

In this chapter we use spectral component modeling to derive the physical parameters describing galactic dust and gas emission observed by FIRAS. The component errors are given by equation 7.6 and include the D, PTP, PUP, and PEP error terms discussed in chapter 5. We have removed the emissions due to the CBR monopole, the CBR dipole, the zodiacal dust, and the CO, C^0, and N^+ lines as described in chapter 6. The only signals left in the data should be due to galactic dust and the C^+ line. In order to model just the dust emission, we cut out the spectral region ($61 - 66$ cm^{-1}) containing the C^+ line. We tried subtracting the emission due to this line as described in chapter 6, but, where the emission is strong, non-negligible residuals were left. Once we find a best fit dust model, we fit the data with the C^+ region left in to a combined model of dust and gas.

The PCA method provides a linearized description of the data. In order to obtain physical parameters for each individual spectra from this method, these parameters must themselves be linear coefficients. In chapter 8, after using the spectral components to determine the best fit basis spectra, we successfully modeled each spectrum with three linear coefficients: the monopole coefficient, the dipole coefficient (dT), and the dust optical depth (τ). If the data cannot be described by a linearized physical model, the PCA method fails to yield reasonable physical parameters. For data along the galactic plane, in which the FIRAS beam samples a wide range of dust temperatures in each pixel, PCA modeling suffers for this reason.

The data set was divided into five galactic latitude ranges to give PCA smaller portions of data to linearize and to search for any latitudinal variations. The regions are given in table 9.1

Region	Range in $\sin b$	Range in b°	Distinguished Citizens
B5	0.8 – 1.0	53.13 – 90.0	NGP
	-1.0 – -0.8	-53.13 – -90.0	SGP
B4	0.6 – 0.8	36.87 – 53.13	
	-0.8 – -0.6	-53.13 – -36.87	
B3	0.4 – 0.6	23.58 – 36.87	
	-0.6 – -0.4	-36.87 – -23.58	LMC
B2	0.1 – 0.4	5.74 – 23.58	Oph
	-0.4 – -0.1	-23.58 – -5.74	Orion
B1	-0.1 – 0.1	-5.74 – 5.74	GC, Cyg
			tons of dust

Table 9.1: Regions under surveillance

and they are outlined in figure 9-1 against a map of the high frequency power. The following sections present the results of PCA analysis and modeling as it was applied to these areas and the interpretation of the dust and C^+ emission in terms of the PDR model.

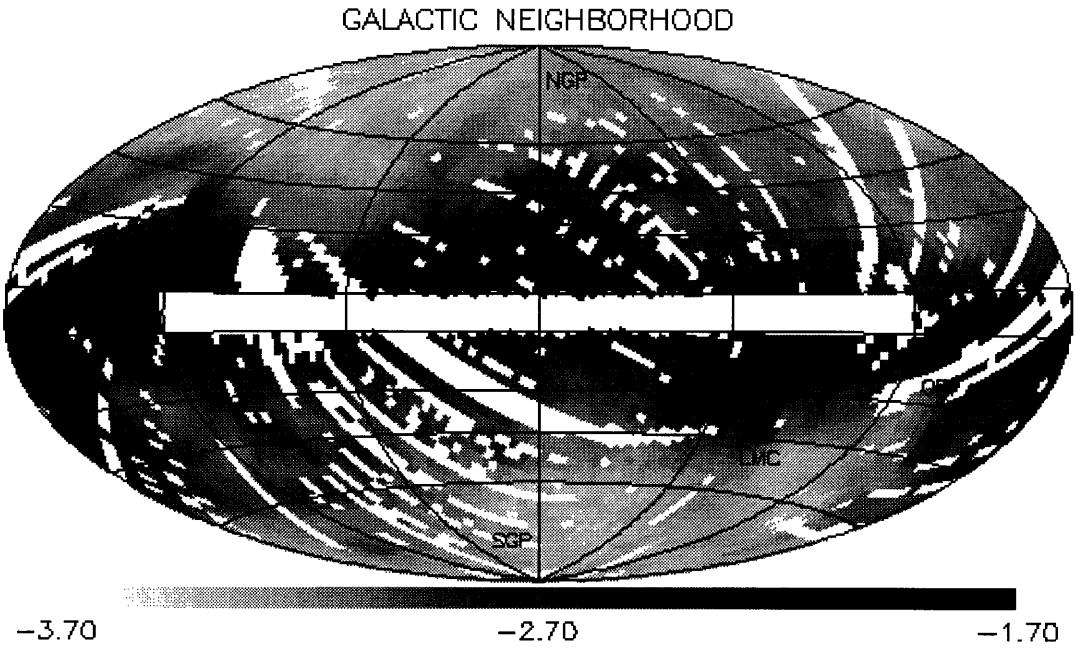

Figure 9-1: Galactic neighborhood

9.1 Region B5 : High Latitudes

At high galactic latitudes ($|b| > 53°$) only one principal component is significant in both the low and high frequency channels. The χ^2/DOF for their noise components are presented in table 9.3 where the DOF were determined from equation 7.13. The two models we fit to the significant components are

$$\left(\frac{\nu}{\nu_0}\right)^{\alpha_1} B_\nu(T_1) \tag{9.1}$$

$$\left(\frac{\nu}{\nu_0}\right)^{\alpha_1} B_\nu(T_1) + \frac{\tau_2}{\tau_1}\left(\frac{\nu}{\nu_0}\right)^{\alpha_2} B_\nu(T_2) \tag{9.2}$$

where $\nu_0 = 40$ cm^{-1}, α is the emissivity index, T is the dust temperature, and τ_i is the dust optical depth for a particular dust component. In equation 9.2 the parameter that interests us is the dust optical depth ratio τ_2/τ_1 between the two dusts. We refer to the models in equations 9.1 and 9.2 as the single dust and the two dust models respectively.

The best fit parameters for these models are given in table 9.2 along with χ^2 and the DOF for each fit. Also in table 9.2 are the results from fitting the same data to the same models but using the template method where the template is taken to be the integral of the high frequency power. The parameters from this method, the χ^2, and the DOF are presented below the corresponding PCA values. The uncertainties cited are 1σ. We see that the derived parameters from the two methods agree reasonably well with each other in each model. The parameters in the first two columns do not, however, agree within statistical error. The χ^2 for the fits are a factor $\sim 10 - 15$ higher than expected for the number of DOF. This large χ^2 can be attributed to our neglect of the JCJ errors in the data which come into play when averaging over large areas of the sky. The corresponding parameter uncertainties from the fits are therefore too low. We discuss only the last two models since their χ^2's are the lowest. These models and the spectral components are given in figure 9-2.

We can perform an F-test on the two competing models to test whether the two dust model is significantly better than the single dust model. [Bevington 69] gives the following definition for the F-test

$$F_\chi = \frac{\Delta\chi^2}{\chi^2/\mathrm{DOF}} \tag{9.3}$$

where $\Delta\chi^2$ is the difference in χ^2 between the two fits. [Bevington 69] also gives a table of probabilities for a given value of F_χ which for DOF $\sim \infty$ lists a probability of 0.001 for

Model	1 dust	1 dust	2 dust
T_1	$15.93 \pm .05$	$24.35 \pm .56$	$18.88 \pm .31$
	$15.61 \pm .05$	$24.15 \pm .44$	$18.82 \pm .26$
α_1	2	$.88 \pm .05$	2
	2	$.89 \pm .03$	2
T_2			$8.33 \pm .38$
			$8.31 \pm .26$
α_2			2
			2
τ_2/τ_1			$8.15 \pm .82$
			$8.07 \pm .49$
χ^2	2233	1752	1726
	2409	1611	1594
DOF	149	148	147
	150	149	148

Table 9.2: Region B5 PCA and template results

Channel	χ^2_n	DOF	χ^2_n/DOF
Low	26697	33666	.793
High	120874	129234	.935

Table 9.3: B5 Noise components

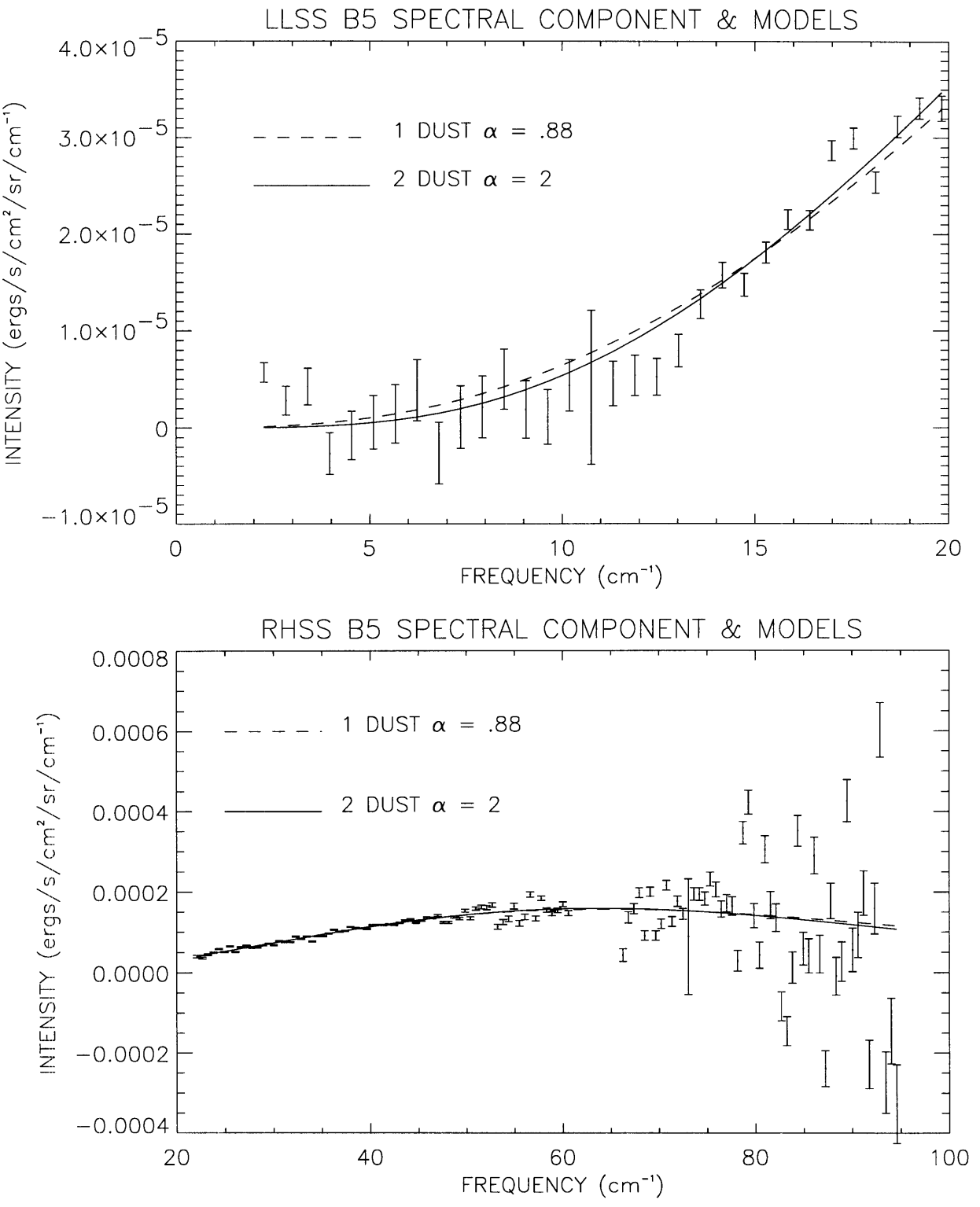

Figure 9-2: LLSS and RHSS components and models for B5

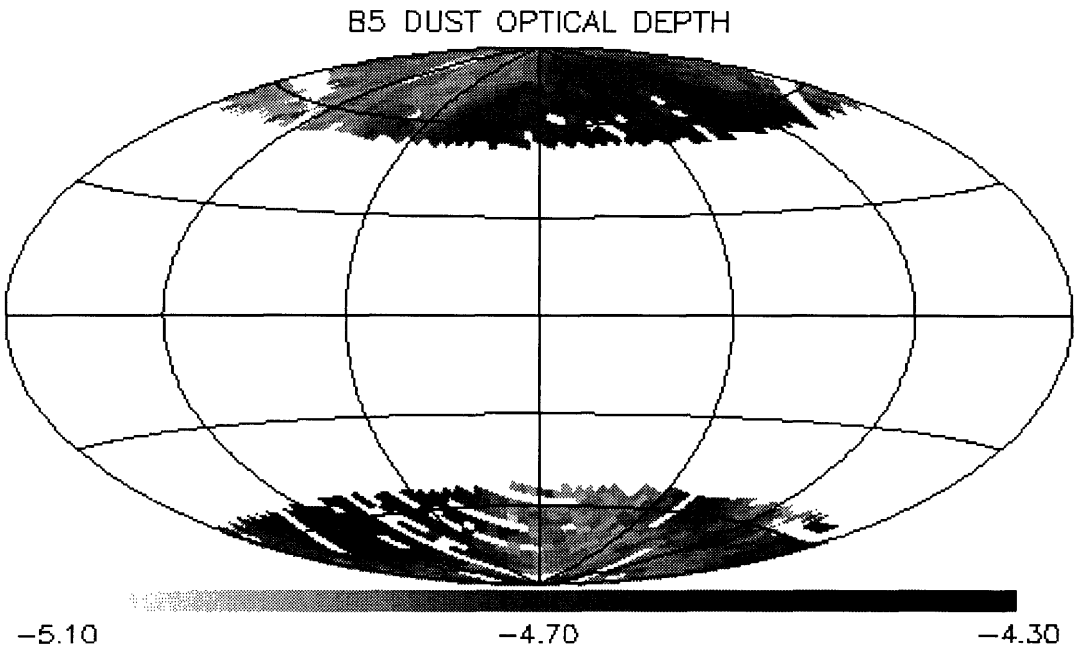

Figure 9-3: Log-scaled optical depth for two dust model

$F_\chi > 10.8$. Both the PCA and template fits have $F_\chi < 3$ indicating the the two dust model does not fit significantly better than the single dust model.

We use the parameters for the single dust model to form a spectral template for dust emission. As a second template we use the instrument profile of the C^+ line. With the data in the C^+ line region included, we model each spectrum with

$$I_\nu = \tau_1 D_\nu(T_1) + I\left(C^+\right) L_{C+} \tag{9.4}$$

where τ_1 is the dust optical depth, $D_\nu(T)$ denotes the dust spectrum $(\nu/\nu_0)^\alpha B_\nu(T)$, $I(C^+)$ is the C^+ line intensity and L_{C+} is the instrument line profile. The line profile is discussed in depth in [Bennett 94] and depends on the apodization function and the electronics transfer function. The frequency integral of L_{C+} is normalized to unity so that the coefficient $I(C^+)$ gives the line intensity in ergs s^{-1} cm^{-2} sr^{-1}. We fit each spectrum for τ_1 and $I(C^+)$ and the resulting reduced χ^2 is 0.82 summed over all pixels. The map of dust optical depth is given in figure 9-3. No pixels exhibited appreciable ($> 4\sigma$) C^+ emission.

The PDR model discussed in section 2.3 predicts two dust temperatures for a cloud with several magnitudes of extinction. Since this portion of the data only calls for a single dust

model, we surmise that clouds with sufficient extinction to develop cold cores do not dominate the high latitude FIR emission.

The lack of C^+ line intensity has two possible explanations: the PDR surfaces responsible for the dust emission do not have enough density to produce detectable line emission, or the PDR surfaces themselves are not present at high latitudes. In first scenario, the dust emission is produced by shallow PDR surfaces, with small optical depths, which do not produce enough photoelectrons to efficiently heat the gas. In the second case the dust emission originates not from PDR surfaces but from warmer regions. In these warm regions other transitions, which have higher excitation energies, are available to cool the gas.

Model	1 dust	1 dust	2 dust
T_1	$16.65 \pm .03$	$20.32 \pm .24$	$17.49 \pm .08$
	$16.41 \pm .03$	$21.34 \pm .21$	$17.46 \pm .08$
α_1	2	$1.42 \pm .03$	2
	2	$1.28 \pm .02$	2
T_2			$6.30 \pm .22$
			$6.28 \pm .19$
α_2			2
			2
τ_2/τ_1			7.96 ± 1.25
			$8.20 \pm .85$
χ^2	1049	700	645
	1598	735	631
DOF	149	148	147
	150	149	148

Table 9.4: Region B4 PCA and template results

9.2 Region B4 : High Intermediate Latitudes

Similar to region B5, data from the latitude range $37° < |b| < 53°$ exhibit only one significant component. The information on the noise components is given in table 9.5. The component models are the same as those given for the high latitudes. The results of fitting the spectral components to the single dust model in equation 9.1 and the two dust model in equation 9.2 are given in table 9.4 along with the parameters determined using the template method. We again see the consistency between the PCA and template fitting methods if allowances are made for the large χ^2 of the fits. Performing an F-test on the models in the last two columns indicates that both methods favor the two dust model. Figure 9-4 contains the low and high frequency components and these two models.

Using the two dust model as the dust template, we fit for the optical depth of the hot

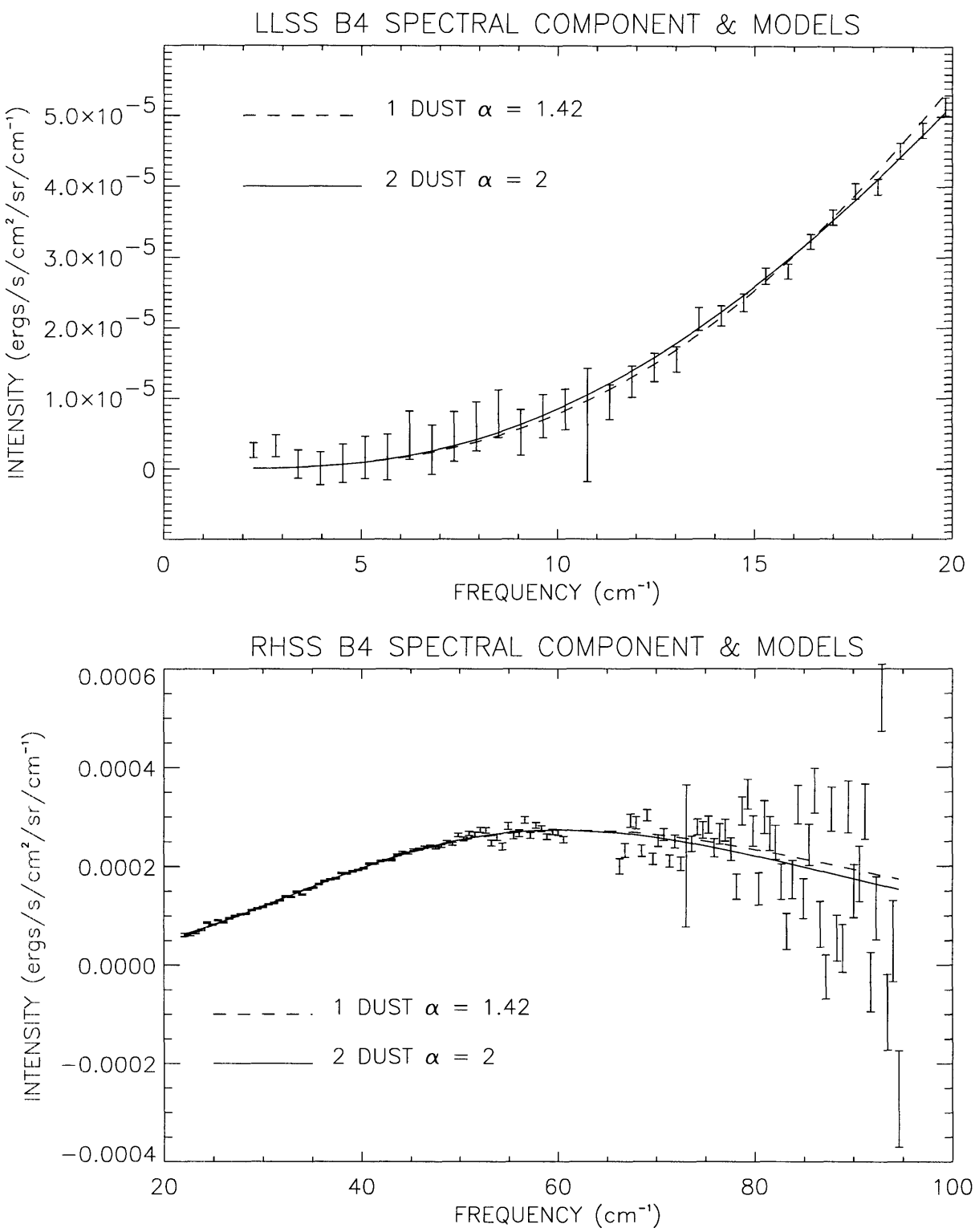

Figure 9-4: LLSS and RHSS components and models for B4

Channel	χ^2_n	DOF	χ^2_n/DOF
Low	29909	32767	.913
High	118516	125783	.942

Table 9.5: B4 Noise components

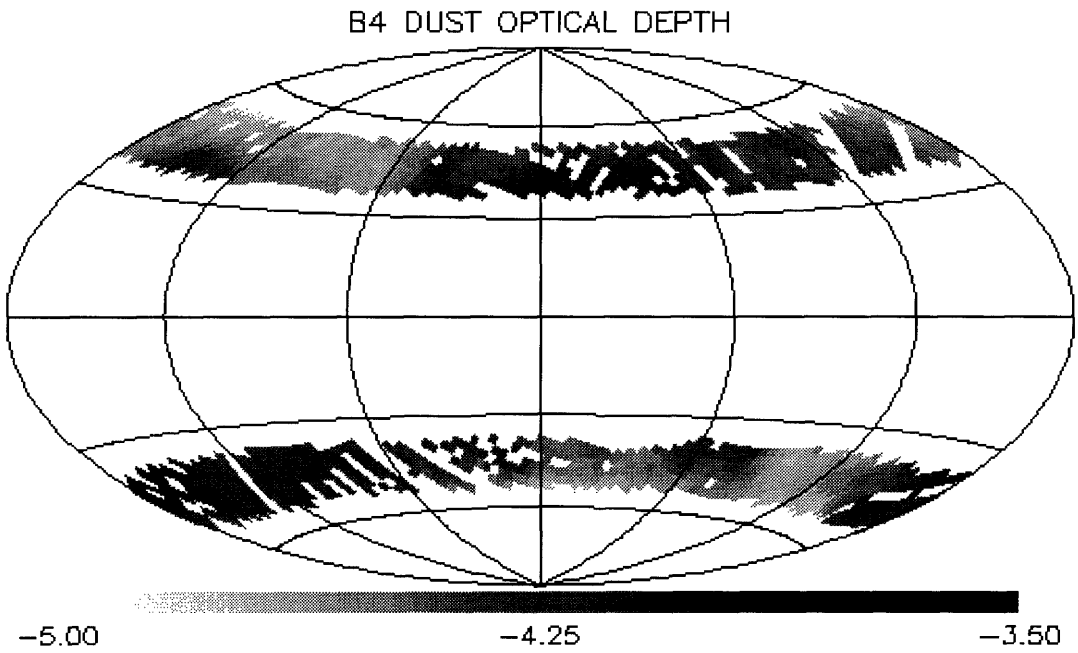

Figure 9-5: Log-scaled optical depth for two dust model

component and also the C^+ line intensity in each pixel. The reduced χ^2 for the entire region is 0.82. The resulting map of the hot dust optical depth is given in figure 9-5. With a 4σ cutoff for the C^+ line detection, the average of $I(C^+)/\tau_1$ for this region is 3.9e-2 $\pm$ 4.9e-3. We examine the *ratio* between the C^+ intensity and the optical depth of the surface layer of hot dust to cancel the effect of a changing filling fraction of the PDR within the FIRAS beam.

Examining the two dust model in terms of the PDR framework, we use the hot dust temperature in equation 2.22 to predict the dust temperature structure of the PDR region. The plot of the structure in figure 9-6 shows a predicted minimum dust temperature of 6.8 K which is consistent with the observed value. The observed optical depth ratio of the cold and

hot dust components ($\sim$ 8) is consistent with the PDR model assuming a linear relationship between optical depth and visual extinction.

To test the PDR predictions for the C^+ line intensity, we use the hot dust temperature and emissivity index in equation 2.18 and calculate an FUV flux of 4.3 ± 1.9 Habing units. The cited error is due to the 3 K uncertainty in the measurements of [Whitcomb 81] used to calibrate the PDR model. The predicted values for $I(C^+)/\tau_1$ range from 2.7e-2 – 5.8e-2 for neutral hydrogen densities n between 10 cm^{-3} and 100 cm^{-3}. The observed value agrees with PDR of density of $\sim$ 20 cm^{-3}. Caution must be used when comparing observed intensities with those predicted due to uncertainties in the model. A possible source of error is that PDR model is only one-dimensional and geometrical factors have been ignored. Another possible error is that the dust optical depth, determined by equation 2.21 based on the emissivity index and the measurements of [Whitcomb 81], is underestimated if radiation below 6 eV is responsible for a significant amount of dust heating.

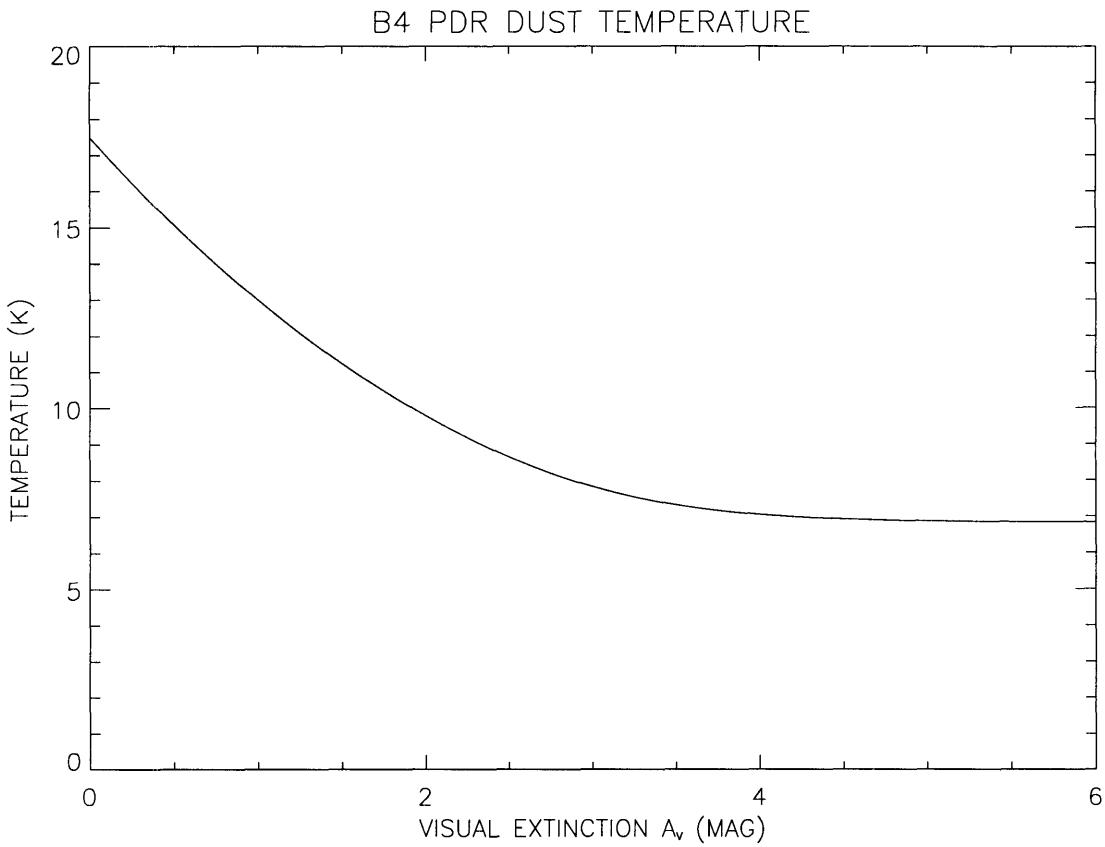

Figure 9-6: PDR dust temperature for B4

9.3 Region B3 : Low Intermediate Latitudes

The latitude region $24^\circ < |b| < 37^\circ$ includes the LMC and the area above the dusty region in Ophiuchus. One component is significant in the low frequency data and two are significant in the high frequency data. The noise component information is given in table 9.7. Since we have two components at high frequency we must model them with two physical models. The single dust model has the constituents

$$\left(\frac{\nu}{\nu_0}\right)^{\alpha_1} B_\nu(T_1) \qquad \left(\frac{\nu}{\nu_0}\right)^{\alpha_1} \left.\frac{\partial B_\nu(T)}{\partial T}\right|_{T_1} \tag{9.5}$$

and the two dust model has the constituents

$$\left(\frac{\nu}{\nu_0}\right)^{\alpha_1} B_\nu(T_1) + \frac{\tau_2}{\tau_1}\left(\frac{\nu}{\nu_0}\right)^{\alpha_2} B_\nu(T_2) \qquad \left(\frac{\nu}{\nu_0}\right)^{\alpha_1} \left.\frac{\partial B_\nu(T)}{\partial T}\right|_{T_1} \tag{9.6}$$

where we have assumed that the second component is due to a variation in the dust temperature. We model this with a temperature derivative of the dust model. The best fit PCA parameters are given in table 9.6 along with the χ^2. Checking these results is more difficult than in the previous cases because now we have a dust signal whose temperature changes with position. The template method, while yielding parameters averaged over some large area, cannot reflect a changing dust temperature. We give the resulting template parameters below their PCA counterparts in table 9.6 along with the goodness of fit (χ^2).

We see the PCA values for T_1 are all lower than the template determinations. While PCA can account for the hotter temperatures with the temperature derivative constituent, the template method can only give an average temperature for the same data. The two methods do however yield the same emissivity index for the single dust model. In the two dust model, the template determination of the cold dust optical depth is a factor ~ 2 greater than the PCA determination. This is perhaps an artifact of averaging many spectra at different temperatures. The hotter spectra may contribute enough signal at the low frequencies which can masquerade as cold dust with large optical depth. Comparing the χ^2 for the single dust and two dust models, we see that both methods favor the two dust model. The spectral components and the single and two dust models are given in figures 9-7 and 9-8.

We use the parameters for the two dust model to form spectral templates and determine the spatial coefficients of the data projected onto these templates. The spectrum in each pixel

Model	1 dust	1 dust	2 dust
T_1	$16.80 \pm .22$	$17.82 \pm .11$	$16.50 \pm .16$
	$17.05 \pm .01$	$20.43 \pm .11$	$17.71 \pm .03$
α_1	2	$1.45 \pm .03$	2
	2	$1.49 \pm .01$	2
T_2			$7.58 \pm .28$
			$5.91 \pm .13$
α_2			2
			2
τ_2/τ_1			$3.37 \pm .31$
			$8.07 \pm .74$
θ	-1.36e-2 $\pm$ 8.11e-3	-8.38e-2 $\pm$ 7.04e-3	-6.67e-2 $\pm$ 1.16e-2
χ^2	2121	1393	1338
	2305	864	593
DOF	266	265	264
	150	149	148

Table 9.6: Region B3 PCA and template results

Channel	χ^2_n	DOF	χ^2_n/DOF
Low	28306	31080	.911
High	114536	122248	.937

Table 9.7: B3 Noise components

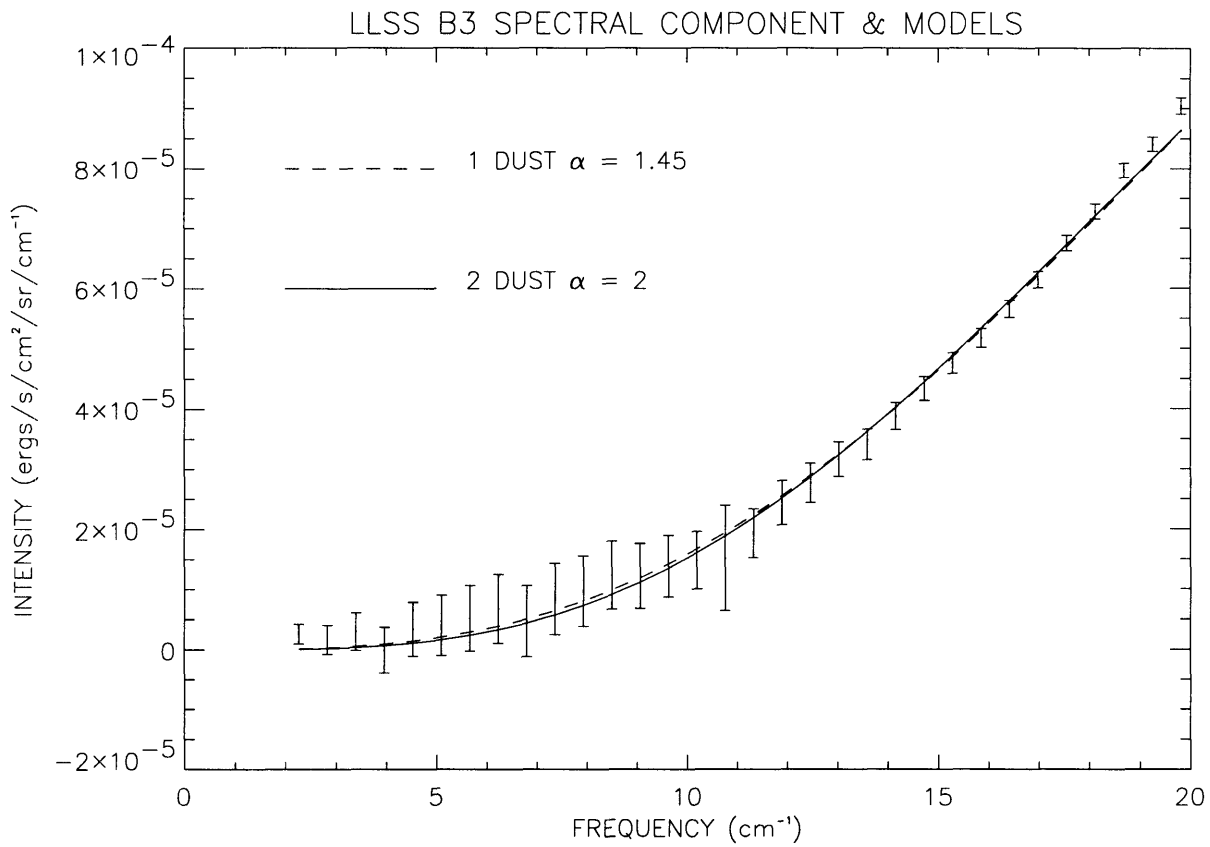

Figure 9-7: LLSS component and models for B3

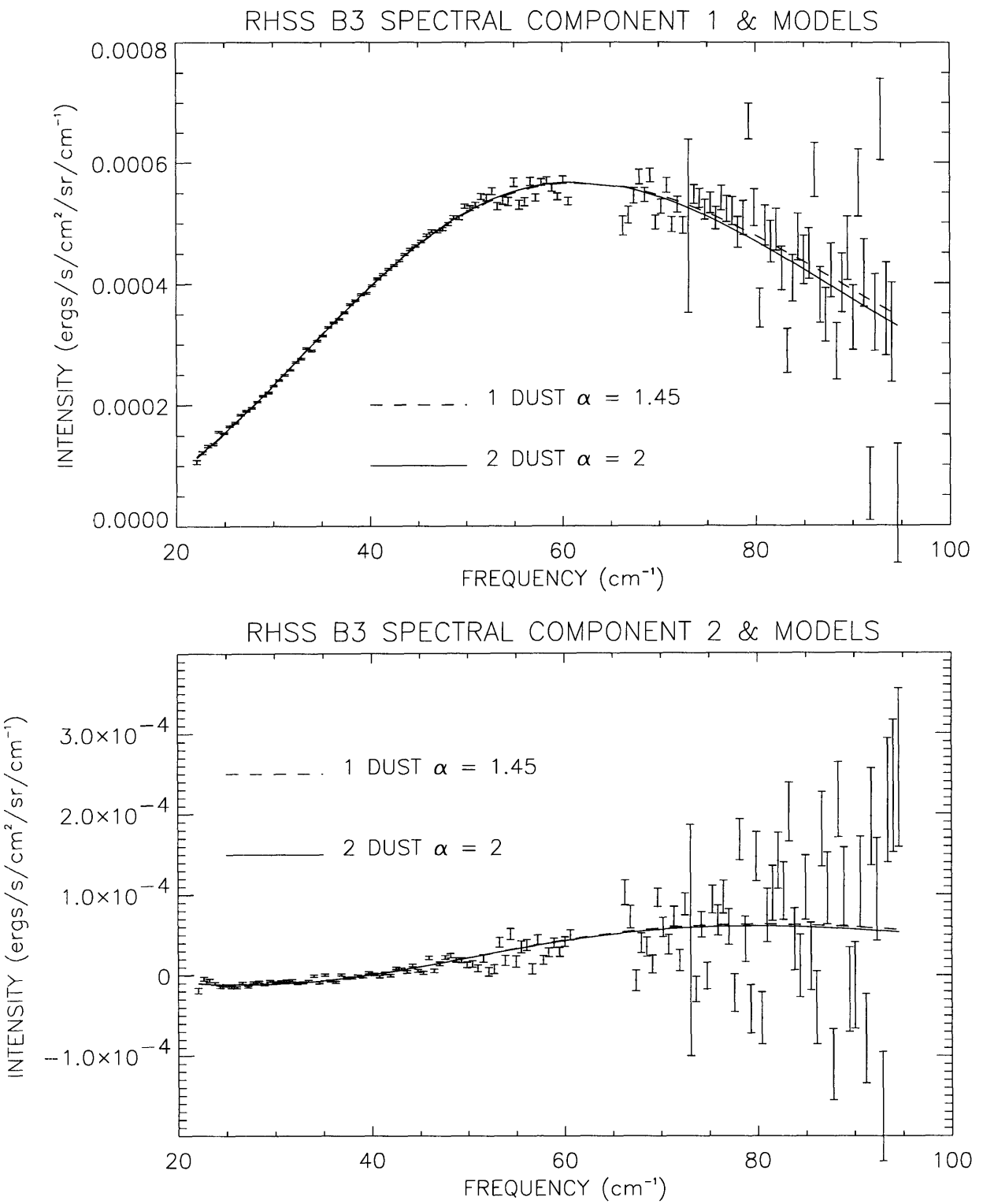

Figure 9-8: RHSS component and models for B3

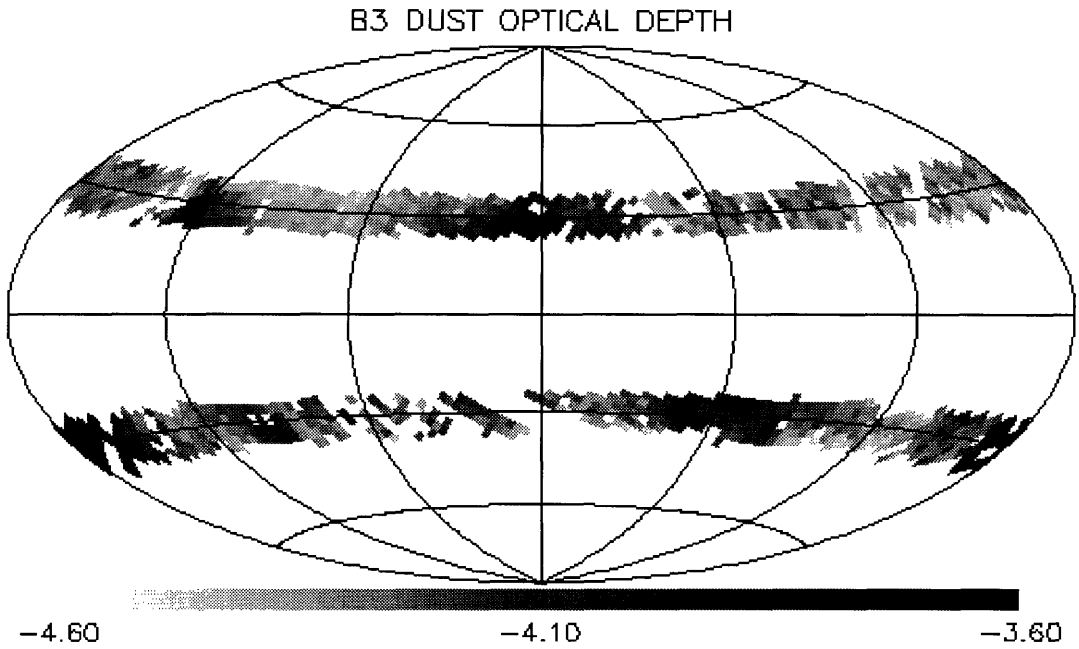

Figure 9-9: Log-scaled optical depth for hotter dust of the two dust model

is described by

$$I_\nu = \tau_1 \left[D_\nu(T_1) + \frac{\tau_2}{\tau_1} D_\nu(T_2) \right] + \tau_1' \left. \frac{\partial D_\nu(T)}{\partial T} \right|_{T_1} + I\left(\mathrm{C}^+\right) L_{\mathrm{C}^+} \tag{9.7}$$

where $D_\nu(T)$ denotes the dust spectrum, τ_1 and τ_1' are the coefficients of the two constituent spectra at the given pixel and $I(\mathrm{C}^+)$ is the line intensity. We fit for these coefficients and the resulting reduced χ^2 is 0.81 . If we interpret τ_1' as $\tau_1 dT_1$ we then have

$$I_\nu = \tau_1 \left[D_\nu(T_1 + dT_1) + \frac{\tau_2}{\tau_1} D_\nu(T_2) \right] + I\left(\mathrm{C}^+\right) L_{\mathrm{C}^+} \tag{9.8}$$

This interpretation yields the hot dust's temperature and optical depth and the C^+ intensity as they vary across the sky. These parameters are presented in figures 9-9, 9-10, and 9-11 . The errors on the temperatures are taken from the projection coefficient errors since

$$T = T_1 + dT_1 = T_1 + \frac{\tau_1'}{\tau_1} \tag{9.9}$$

Figure 9-10 excludes pixels where the dust temperature error is greater than 2 K which account for only $\sim 3.5\%$ of the pixels. Comparing the optical depth and temperature maps, we notice that there are some differences. The high temperature regions are found at the LMC,

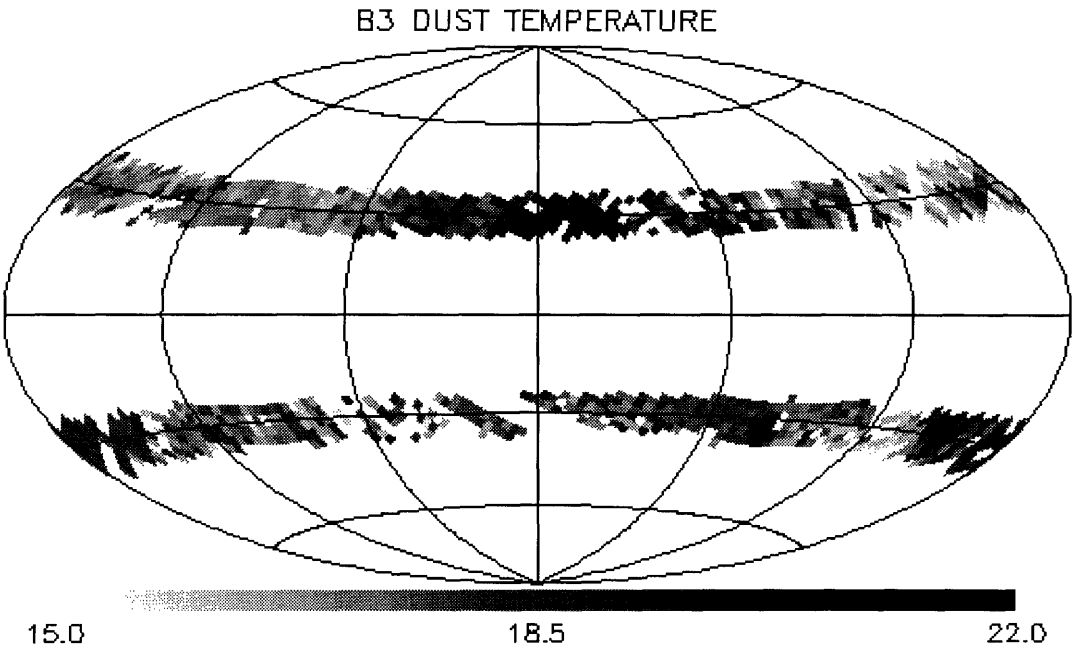

Figure 9-10: Temperature (K) for hotter dust of the two dust model

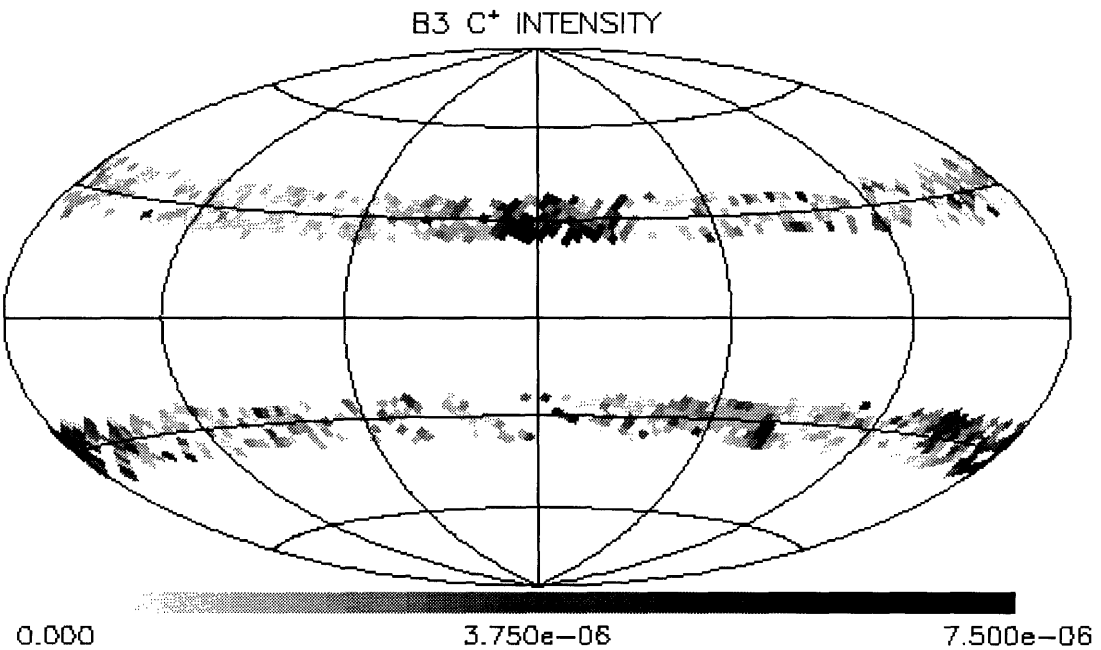

Figure 9-11: $I(C^+)$ in ergs s^{-1} cm^{-2} sr^{-1}

$(l, b) \sim (280^\circ, -30^\circ)$, and near Ophiuchus, $(l, b) \sim (0^\circ, 30^\circ)$. Large optical depths are evident in these regions and elsewhere $(l, b) \sim (120^\circ, 30^\circ), (310^\circ, -30^\circ)$. These differences exhibit the ability of PCA to separate the effects of these two highly correlated model parameters. Comparing the C^+ map with the hot dust temperature map, we see a high degree of correlation indicating the dependence of line emission on the FUV flux traced by the dust temperature.

To compare the fit parameters with the PDR model, we use the hot dust temperature and emissivity index to determine the FUV flux. For the temperature range 15 – 25 K the implied FUV flux is in the range $1.7 \pm .7$ to 37 ± 16 Habing units. The cold dust temperature for the minimum and maximum values of G ranges from 5.6 K to 10.8 K which agrees with the observed value of 7.58 K.

To examine the observed C^+ emission in the PDR framework, we average the intensities greater than 4σ in 1 K temperature bins and plot them in figure 9-12. The line emission is a function not only of the FUV flux, measured by the hot dust temperature, but also of the PDR density. This averaging ignores any density variations and will be dominated by the denser regions due to their stronger emergent intensities. Also plotted in the figure are the predicted values of $\frac{I(C^+)}{\tau_1}$ for n equal to 10 cm^{-3} and 100 cm^{-3}. In the PDR model the dust optical depth may be underestimated and to allow for this error we have divided the model intensities by a factor of 2. Accounting for this factor brings the predicted and observed C^+ intensity as a function of dust temperature into rough agreement.

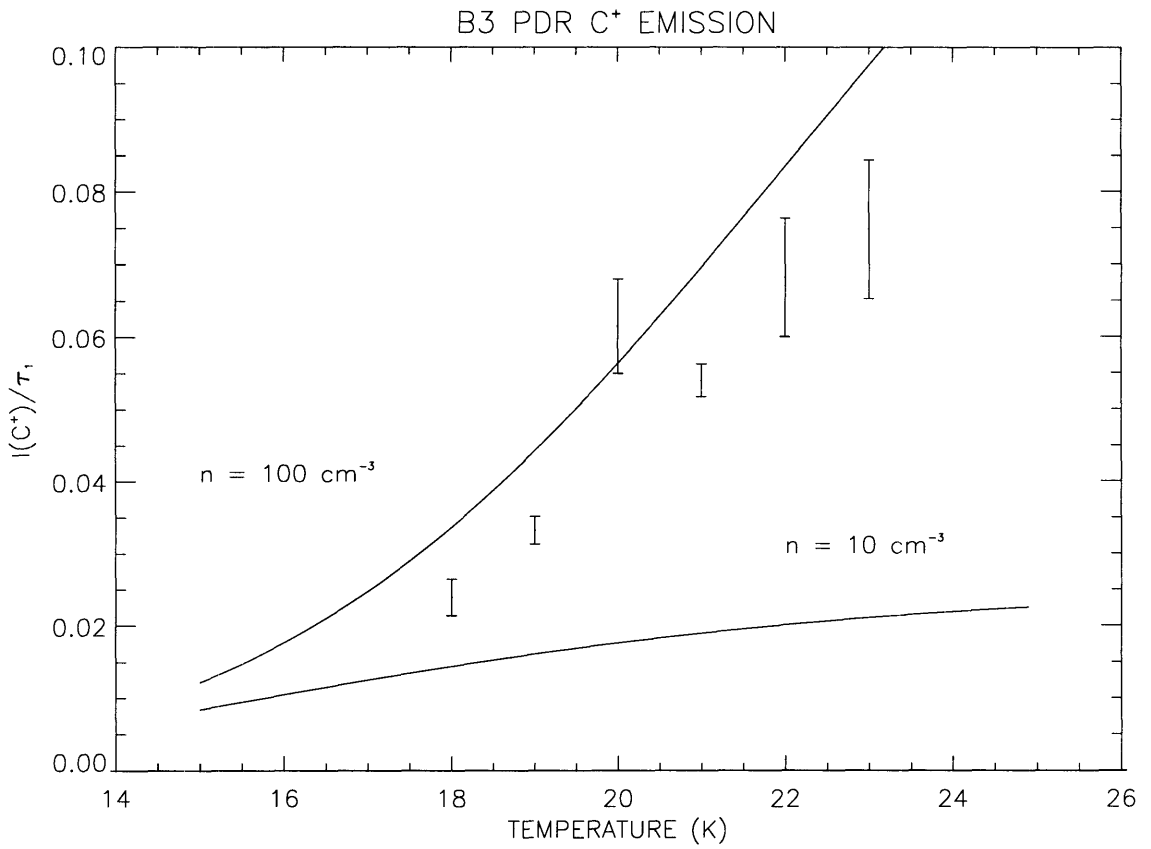

Figure 9-12: PDR C^+ emission for B3

Model	1 dust	1 dust	2 dust
T_1	$17.55 \pm .08$	$19.26 \pm .11$	$18.89 \pm .09$
	$17.32 \pm .01$	$19.35 \pm .03$	$17.65 \pm .01$
α_1	2	$1.81 \pm .01$	2
	2	$1.68 \pm .01$	2
T_2			$6.75 \pm .10$
			$5.23 \pm .05$
α_2			2
			2
τ_2/τ_1			$2.15 \pm .14$
			$8.49 \pm .40$
θ	3.96e-3 $\pm$ 2.76e-2	2.09e-2 $\pm$ 2.69e-3	3.84e-2 $\pm$ 2.67e-3
χ^2	2688	1496	1163
	8551	3176	868
DOF	266	265	264
	150	149	148

Table 9.8: Region B2 PCA and template results

9.4 Region B2 : Low Latitudes

The latitude region $6^\circ < |b| < 24^\circ$ contains the strong FIR emission regions associated with the Ophiuchus and Orion. In this region one component is significant at low frequencies and two at high frequencies. Information on the noise components is given in table 9.9. Since this case is similar to region B3 the reader is referred to equations 9.5 and 9.6 for the models examined.

The best fit parameters for these models are given in table 9.8 along with the corresponding parameters determined by a template fit to the data. The dust parameters of the two methods are rather consistent except for the two dust model where we again see a template optical depth ratio much higher than the PCA determination. In comparing the χ^2's, both PCA and the template method prefer the two dust model. The models from the last two columns in table

Channel	χ_n^2	DOF	χ_n^2/DOF
Low	42547	47027	.905
High	169909	178888	.950

Table 9.9: B2 Noise components

9.8 are plotted along with the spectral components in figures 9-13 and 9-14

As we did in region B3, we use the two dust model and the C^+ line profile to construct spectral templates which are then fit to each spectrum. The reduced χ^2 for this fit is 0.84. The resulting optical depth τ_1, dust temperature T and line intensity $I(C^+)$ are given in figures 9-15, 9-16, and 9-17.

As the dust temperature varies from 15 K, in the outer Galaxy away from the plane, to 22 K, at Ophiuchus and Orion, the implied FUV flux ranges from $1.7 \pm .7$ to 17.0 ± 7.4 Habing units. This determines a cold dust temperature between 5.6 – 9.2 K which agrees with the observed temperature of 6.8 K .

In order to examine the C^+ emission in terms of the PDR model, we ignore the density dependence of the line intensity and determine the average value of $I(C^+)/\tau_1$ as a function of temperature. A weighted average was performed for pixels where the measured line intensity was 4σ above the uncertainty. The results are plotted in figure 9-18. The models found in the figure are for hydrogen atom densities of 10 and 100 cm^{-3} but have been divided by the factor of 2 to account for an underestimated model optical depth. Except for the factor of 2, the higher density model does follow the average dependence of line intensity as a function of temperature.

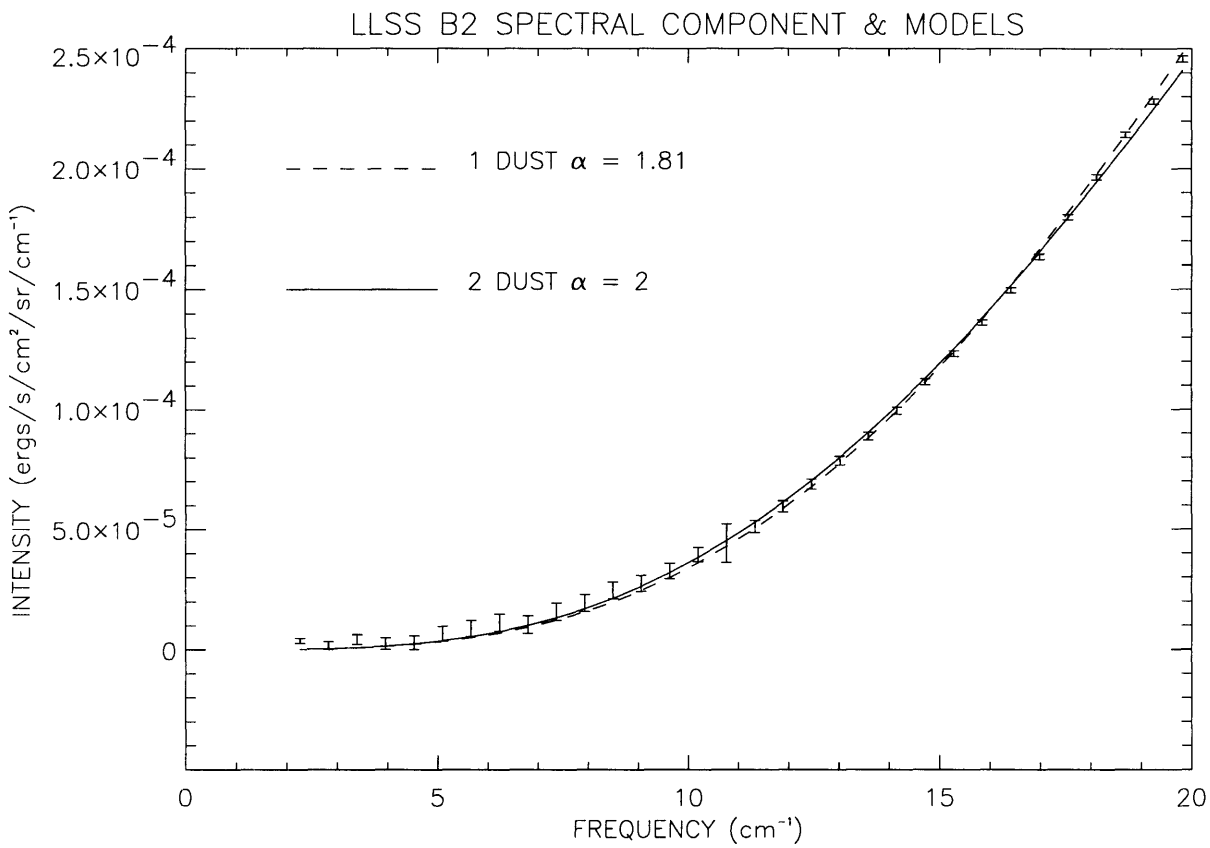

Figure 9-13: LLSS component and models for B2

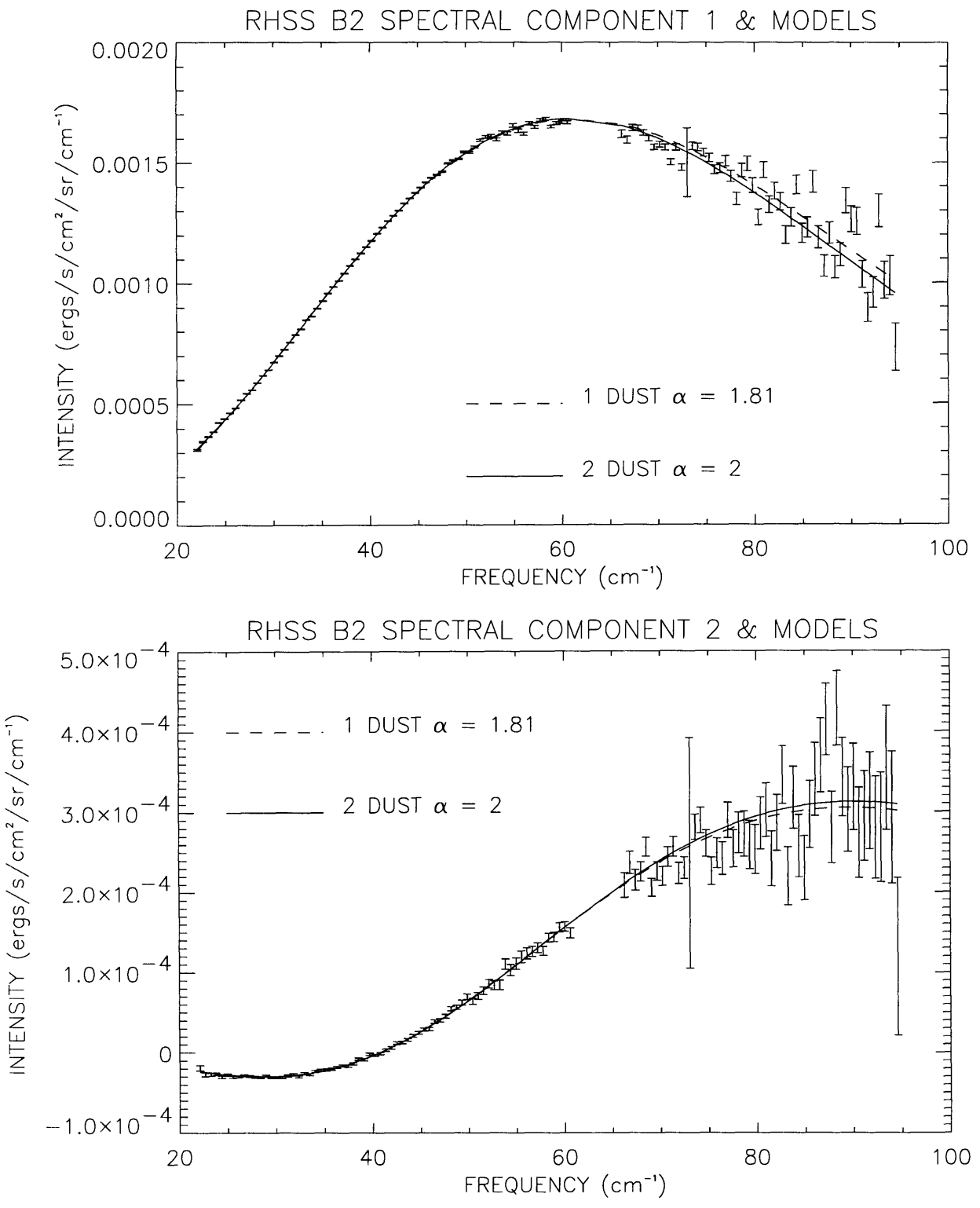

Figure 9-14: RHSS component and models for B2

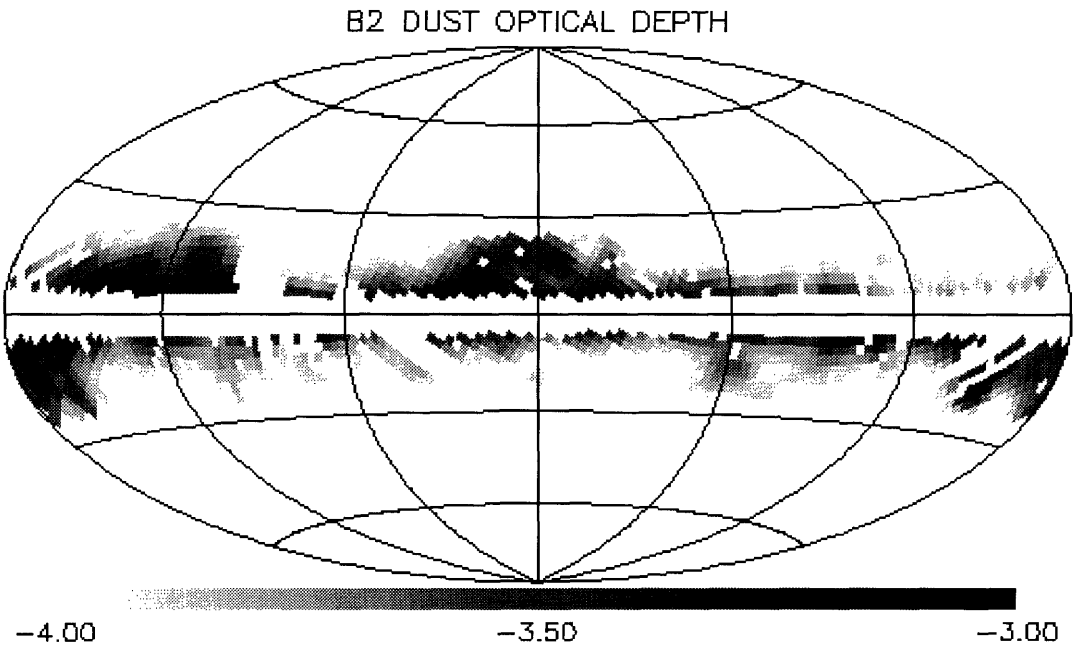

Figure 9-15: Log-scaled optical depth for hotter dust of the two dust model

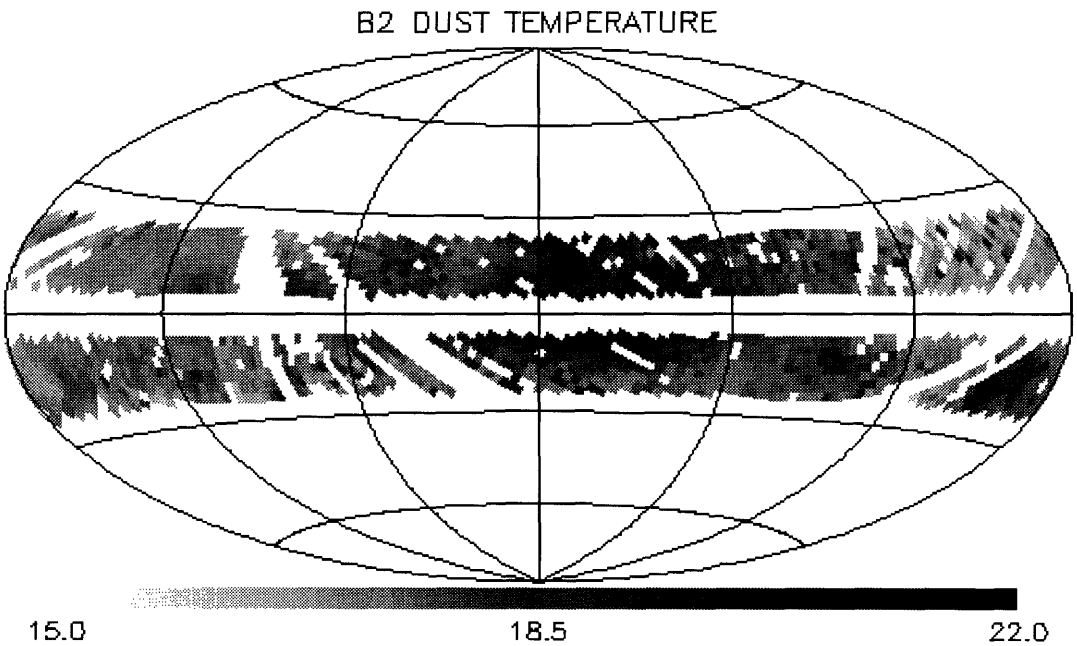

Figure 9-16: Temperature (K) for hotter dust of the two dust model

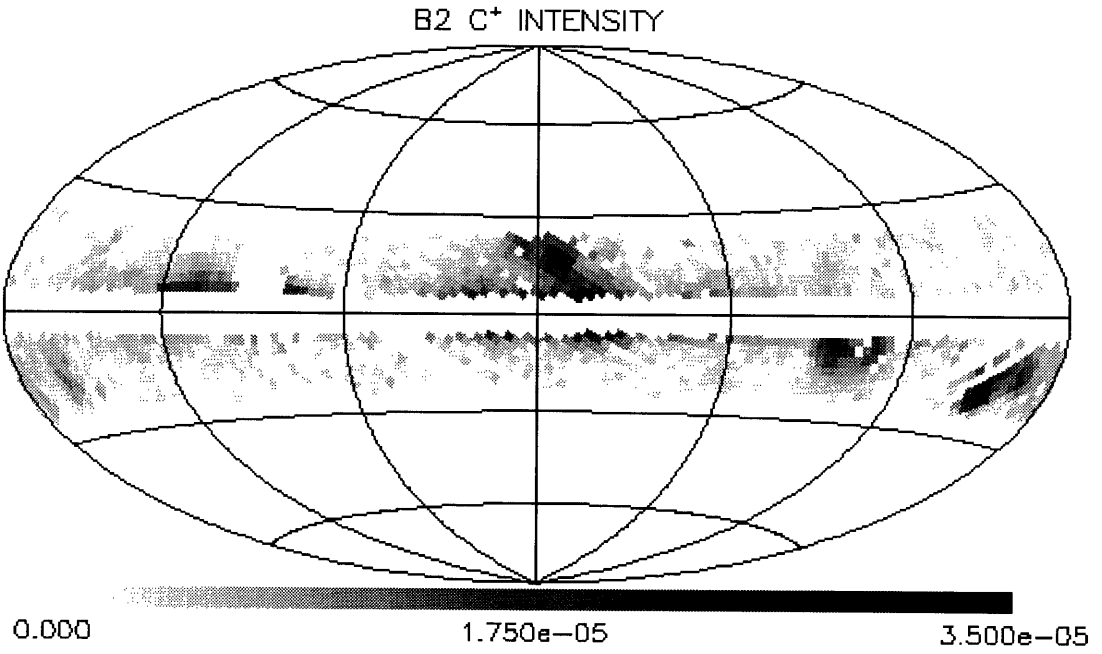

Figure 9-17: $I(C^+)$ in ergs s^{-1} cm^{-2} sr^{-1}

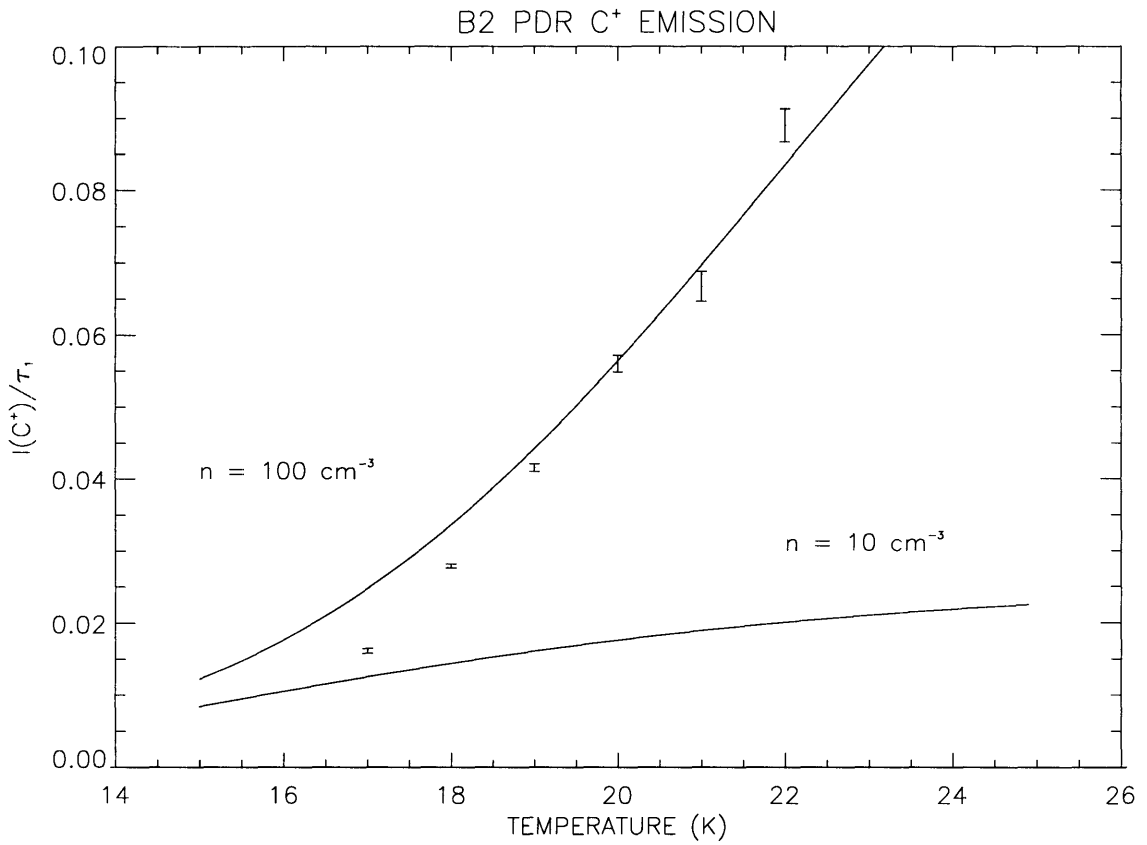

Figure 9-18: PDR C^+ emission for B2

9.5 Region B1 : Galactic Plane

The galactic plane is a source of strong dust emission. PCA modeling proved problematic when the entire plane was treated as a whole due to the large number (~ 5) of significant components. To ease our analysis we further subdivided the plane into more manageable pieces listed in table 9.10.

9.5.1 Outer Galaxy

The outer region of the Galaxy ($120° < l < 240°$) exhibited only one component at low frequencies and two at high frequencies when the C^+ line was excluded. This is the same case as was treated in region B3 and the reader is referred to that section for the model constituents. The best fit parameters and their template counterparts are given in table 9.11 and the noise component information is located in table 9.12.

Referring to table 9.11 we again see that the two dust model is preferred by both the PCA and template analyses. The models from the last two columns are plotted along with the components in figures 9-19 and 9-20.

We use the two dust model parameters in the model given in equation 9.7 to determine the dust optical depth, dust temperature, and C^+ intensity in the manner put forth previously. The reduced χ^2 for this fit is .84. The fit parameters are given in figures 9-21, 9-22 and 9-23. The dust temperature shows very little range in temperature, varying only by $\sim$ 2 K in this region. The implied FUV flux for the temperature range 16 – 18 K is 2.5 ± 1.1 to 5.1 ± 2.2 which is near the value expected for the solar neighborhood. The cold dust temperature for

Region	Range in $l°$
Outer Galaxy	120 – 240
Galactic Disk	5 – 60 , 300 – 355
Spiral Arms	60 - 120 , 240 – 300
Galactic Center	355 – 5

Table 9.10: Galactic plane longitude regions

Model	1 dust	1 dust	2 dust
T_1	$16.38 \pm .18$	$20.40 \pm .27$	$18.03 \pm .18$
	$16.32 \pm .01$	$18.59 \pm .04$	$16.72 \pm .01$
α_1	2	$1.67 \pm .01$	2
	2	$1.61 \pm .01$	2
T_2			$6.87 \pm .13$
			$5.41 \pm .07$
α_2			2
			2
τ_2/τ_1			$2.26 \pm .16$
			$6.73 \pm .38$
θ	-2.75e-3 $\pm$ 6.88e-3	6.06e-2 $\pm$ 4.51e-3	4.32e-2 $\pm$ 5.70e-3
χ^2	1645	668	547
	5251	1276	267
DOF	266	265	264
	150	149	148

Table 9.11: Outer Galaxy PCA and template results

this range of FUV flux varies between 6 – 7 K which agrees with the observed value.

We determine the average C^+ intensity as a function of dust temperature and the results are plotted in figure 9-24. We also plot the model intensity, yet again dividing by that pesky factor of two and we see agreement.

Channel	χ_n^2	DOF	χ_n^2/DOF
Low	4552	5146	.885
High	17825	19470	.916

Table 9.12: Outer Galaxy noise components

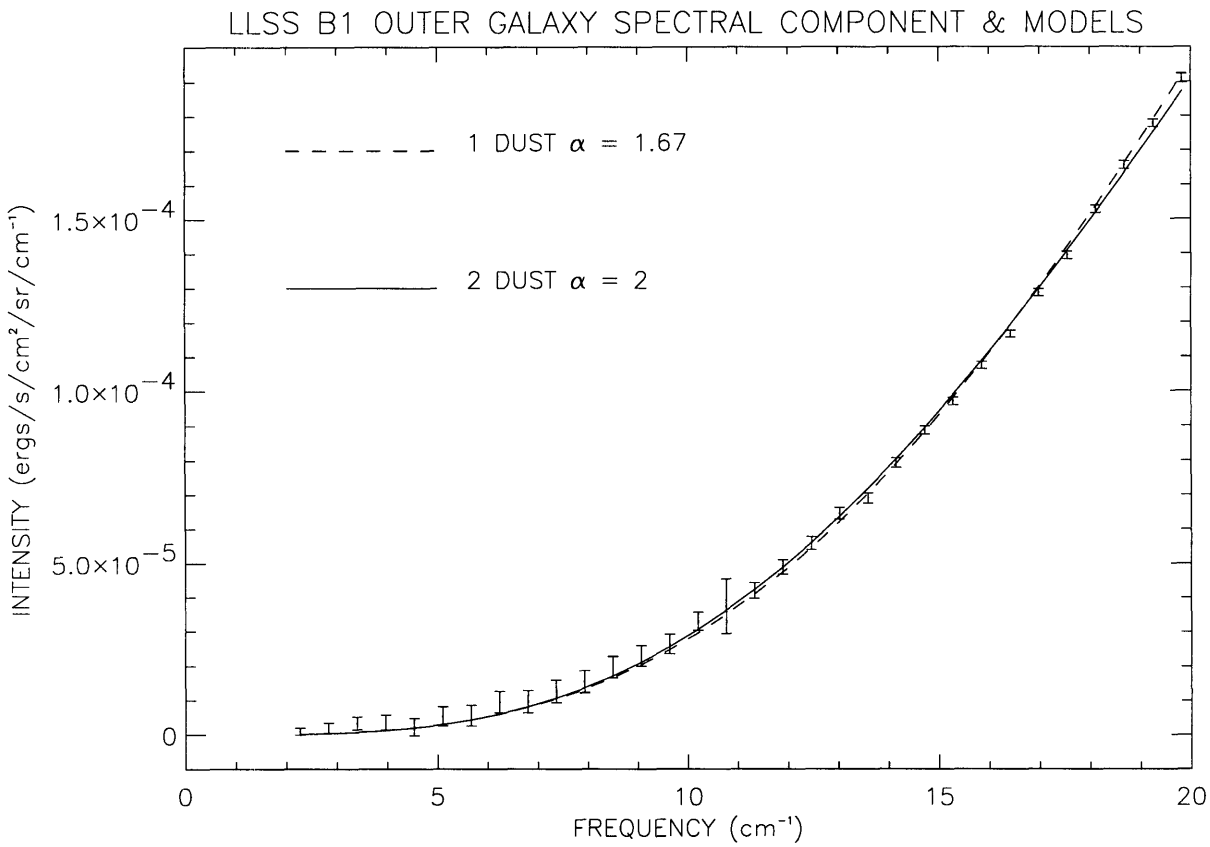

Figure 9-19: LLSS component and models for B1 outer galaxy

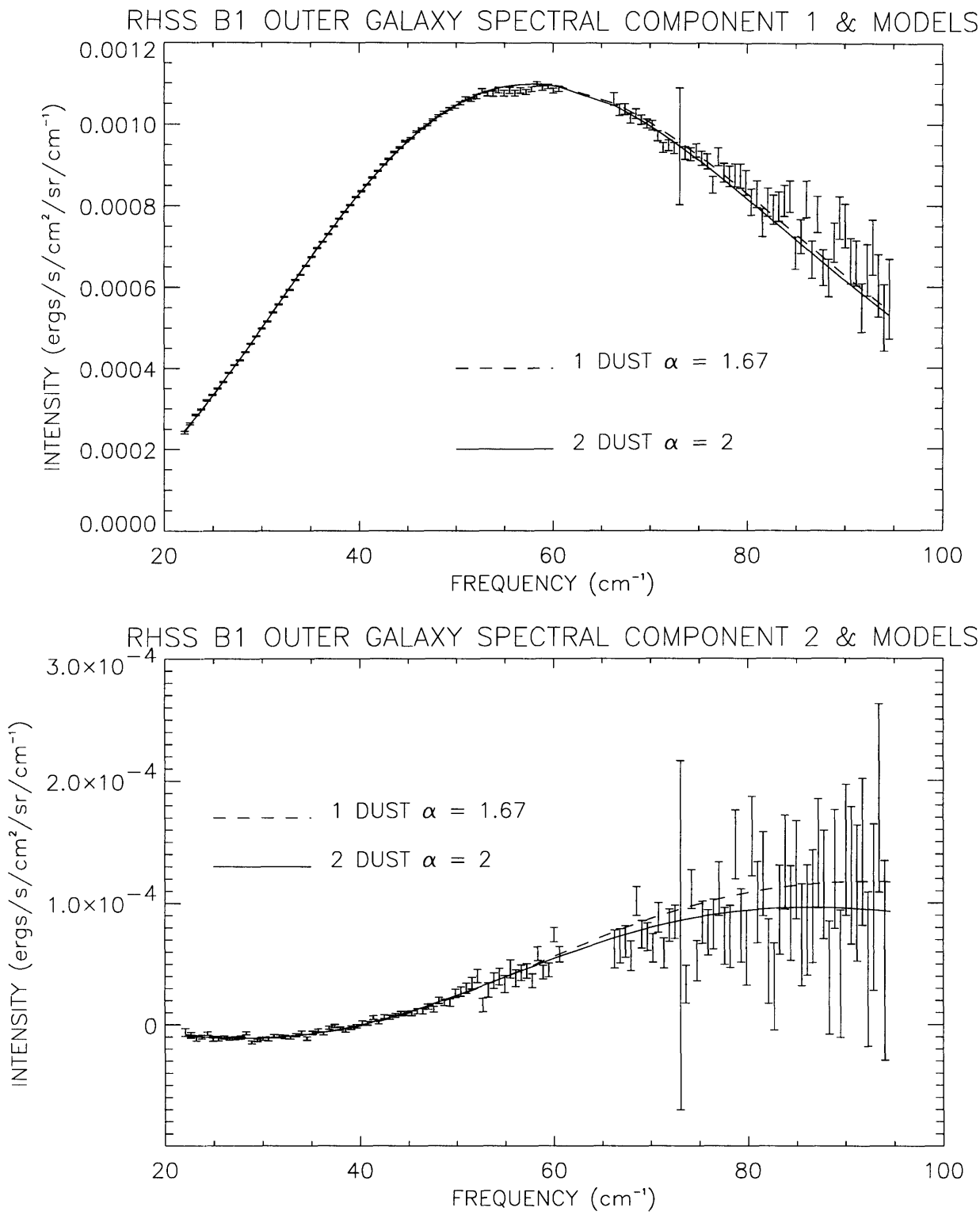

Figure 9-20: RHSS component and models for B1 outer galaxy

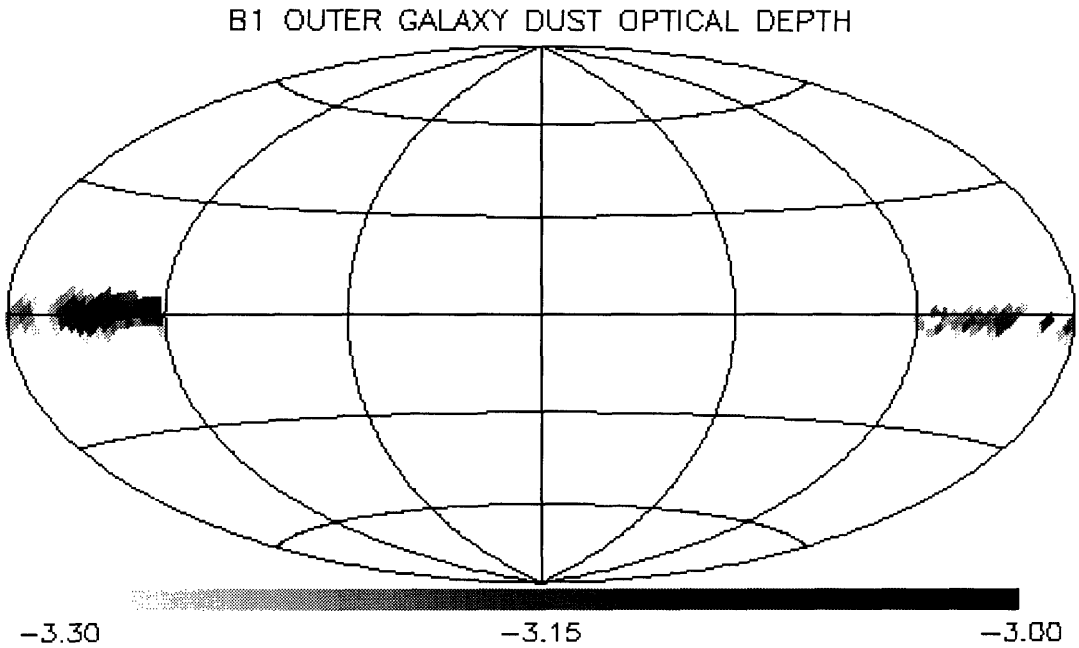

Figure 9-21: Log-scaled optical depth for hotter dust of the two dust model

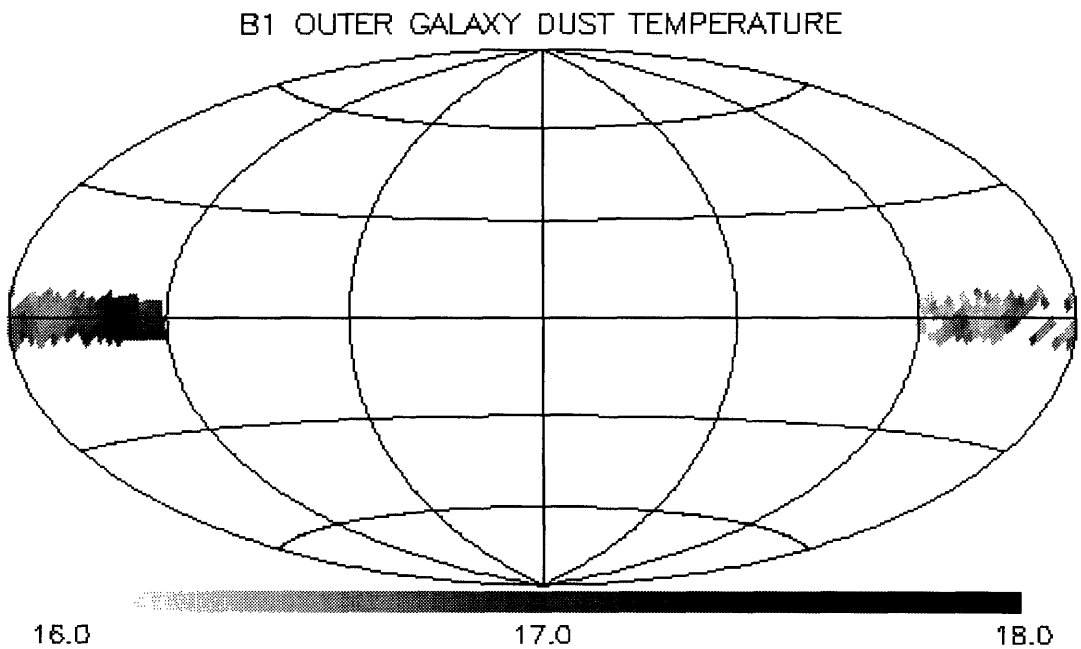

Figure 9-22: Temperature (K) for hotter dust of the two dust model

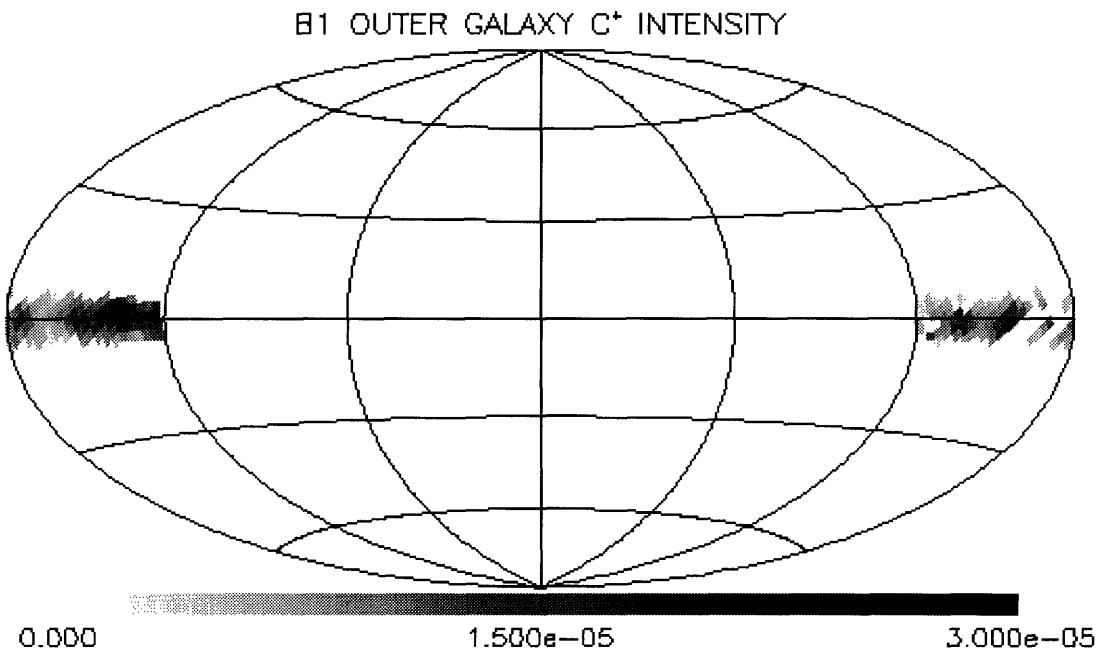

Figure 9-23: $I(C^+)$ in ergs s^{-1} cm^{-2} sr^{-1}

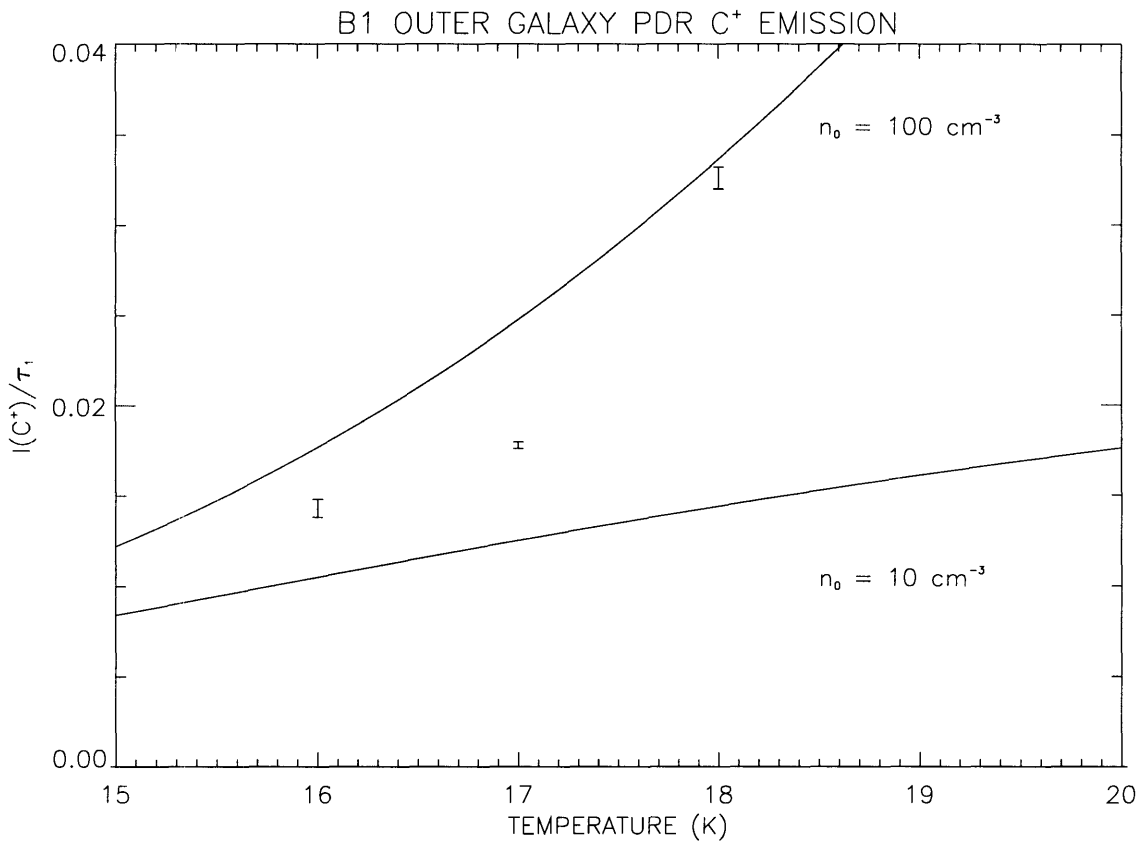

Figure 9-24: PDR C^+ emission for B1 outer galaxy

9.5.2 Galactic Disk

The galactic disk ($5^\circ < l < 60^\circ$ and $300^\circ < l < 355^\circ$) shows strong and variable dust emission evidenced by two significant low frequency components and four significant high frequency components when we ignore the C^+ spectral line region. The noise components are summarized in table 9.14.The four constituent models were taken to be

$$\left(\frac{\nu}{\nu_0}\right)^\alpha \frac{\partial^i B_\nu(T_1)}{\partial T^i} \qquad \text{for } i = 0, 1, 2, 3 \tag{9.10}$$

for the single dust model and

$$\left(\frac{\nu}{\nu_0}\right)^\alpha \left[\frac{\partial^i B_\nu(T_1)}{\partial T^i} + \frac{\tau_2^{(i)}}{\tau_1^{(i)}} \frac{\partial^i B_\nu(T_2)}{\partial T^i}\right] \qquad \text{for } i = 0, 1, 2, 3 \tag{9.11}$$

for the two dust model.

The best fit parameters are given in table 9.13 and we see that the two dust model is preferred although it has many more parameters at its disposal. The cold component of the two dust model has a temperature similar to what was seen at higher latitudes although the optical depth ratio is a factor ~ 2 larger than what was seen in region B2. This is expected as there are far more dust clouds along the plane. The models from the last two columns are plotted along with the components in figures 9-25 – 9-27. Examining the high frequency components 3 and 4 we notice the striking dissimilarity between the two models with the two dust model showing visible superiority over the one dust model.

We have successfully modeled the spectral components but now we must derive the physical parameters in each pixel. We postulate that the hot dust signal contains a distribution of dust temperatures so that its emission can be described by

$$I_\nu = \tau \left[D_\nu(T) + \frac{\sigma^2}{2} \frac{\partial^2 D_\nu(T)}{\partial T^2} + \frac{\mu^3}{6} \frac{\partial^3 D_\nu(T)}{\partial T^3}\right] \tag{9.12}$$

where $D_\nu(T)$ denotes the dust spectrum $(\nu/\nu_0)^2 B_\nu(T)$ at temperature T, τ is the dust optical depth and σ and μ are the width and skew of the distribution. Expanding $D_\nu(T)$ about the found temperature T_1 we can express the intensity from this distribution in terms of the two dust model as follows

$$I_\nu = \tau \left[D_\nu(T_1) + \frac{\tau_2}{\tau_1} D_\nu(T_2)\right] + \tau dT \left[\frac{\partial D_\nu(T_1)}{\partial T} + \frac{\tau_2'}{\tau_1'} \frac{\partial D_\nu(T_2)}{\partial T}\right]$$

Model	1 dust	1 dust	2 dust
T_1	$27.83 \pm .28$	$30.14 \pm .31$	$16.77 \pm .21$
α_1	2	$1.26 \pm .04$	2
T_2			$6.22 \pm .13$
α_2			2
τ_2/τ_1			$8.42 \pm .81$
τ_2'/τ_1'			$.311 \pm .066$
τ_2''/τ_1''			$.541 \pm .178$
τ_2'''/τ_1'''			$-.476 \pm .035$
θ_1	1.47e-1 $\pm$ 4.50e-3	1.37e-2 $\pm$ 6.14e-3	-1.57e-1 $\pm$ 1.09e-2
θ_2	5.62e-2 $\pm$ 2.07e-3	4.93e-2 $\pm$ 8.39e-4	3.06e-2 $\pm$ 3.16e-3
θ_3	-8.04e-3 $\pm$ 7.55e-4	-7.41e-3 $\pm$ 6.23e-4	-8.09e-3 $\pm$ 9.94e-4
θ_4	4.25e-1 $\pm$ 7.95e-3	2.40e-1 $\pm$ 8.76e-3	-1.80e-1 $\pm$ 1.95e-2
θ_5	-1.11e-3 $\pm$ 5.95e-3	9.19e-3 $\pm$ 4.09e-3	1.93e-2 $\pm$ 7.70e-3
θ_6	3.34e-1 $\pm$ 1.38e-2	1.87e-1 $\pm$ 1.33e-2	-3.24e-1 $\pm$ 1.79e-2
χ^2	13984	8619	4744
DOF	508	507	503

Table 9.13: Galactic disk PCA results

Channel	χ_n^2	DOF	χ_n^2/DOF
Low	4495	4830	.931
High	18701	18444	1.014

Table 9.14: Galactic disk noise components

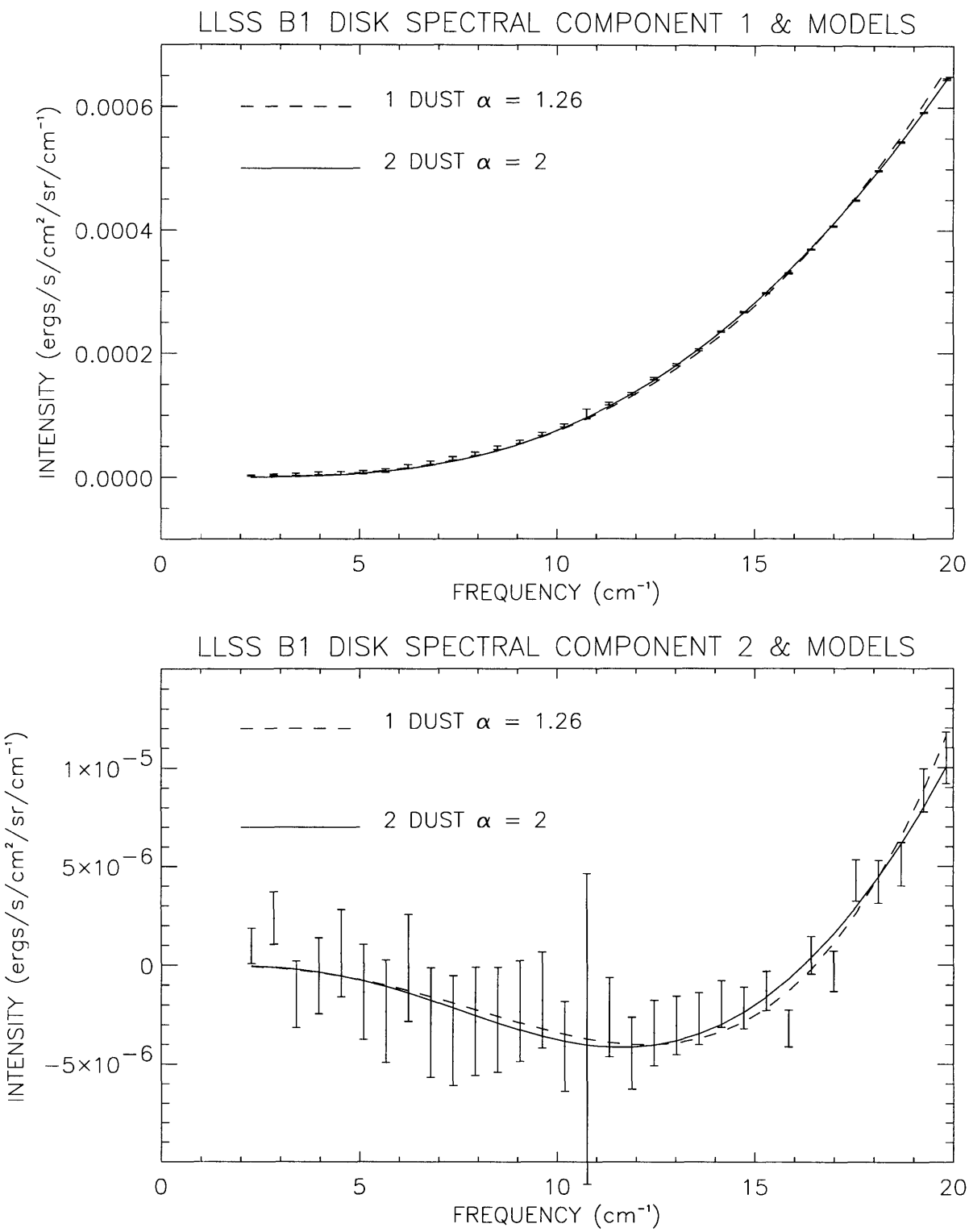

Figure 9-25: LLSS components and models for B1 galactic disk

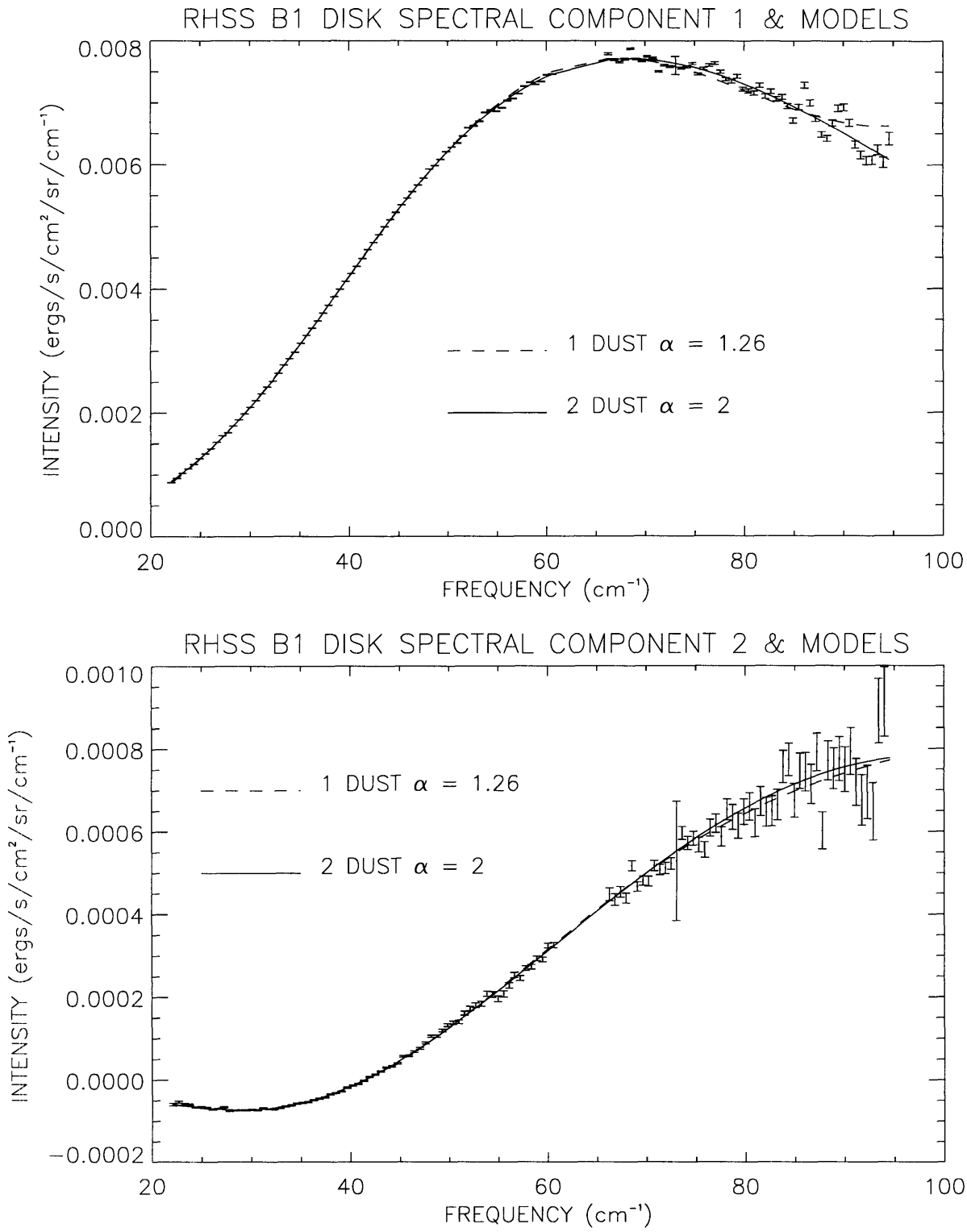

Figure 9-26: RHSS components 1 and 2 and their models for B1 galactic disk

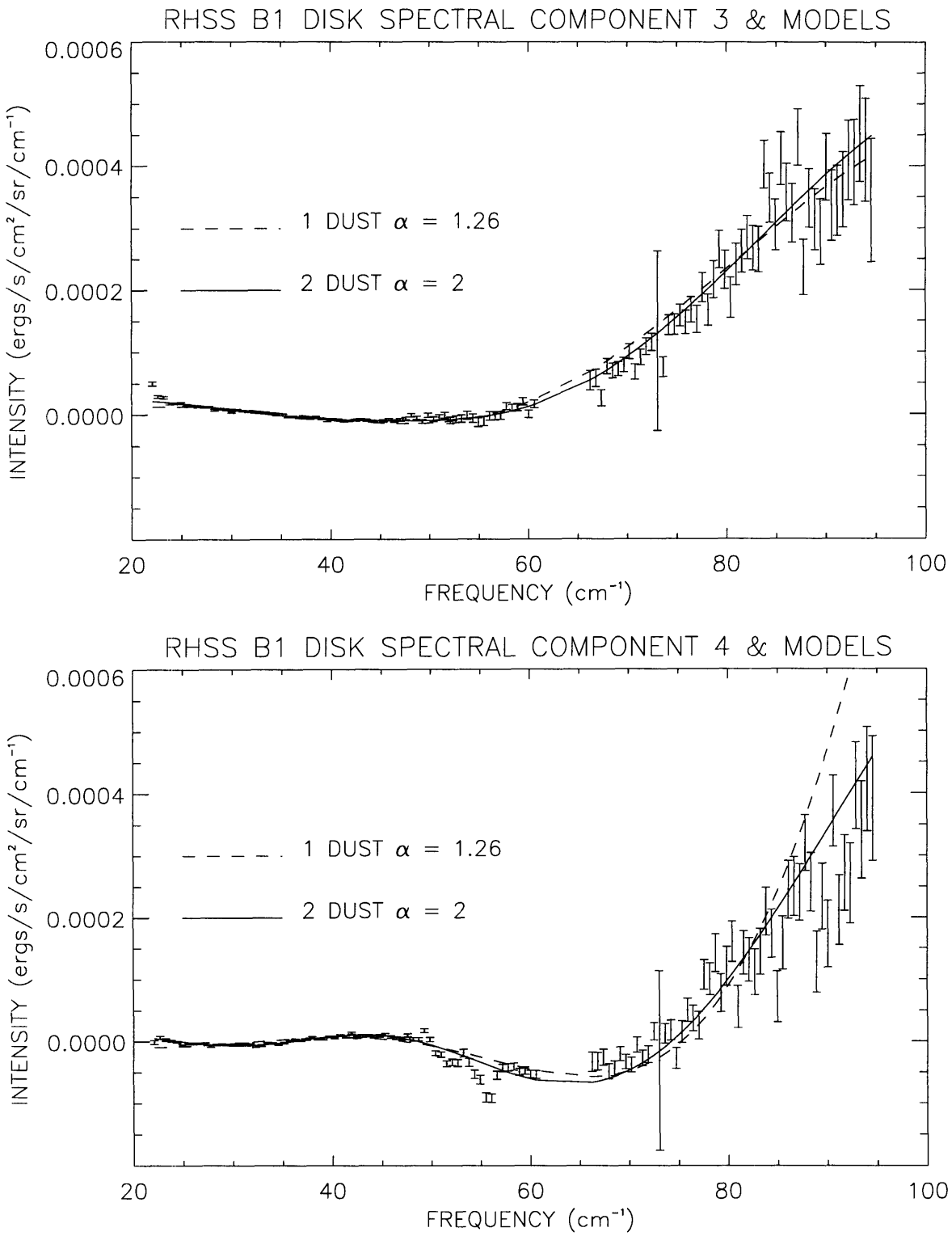

Figure 9-27: RHSS components 3 and 4 and their models for B1 galactic disk

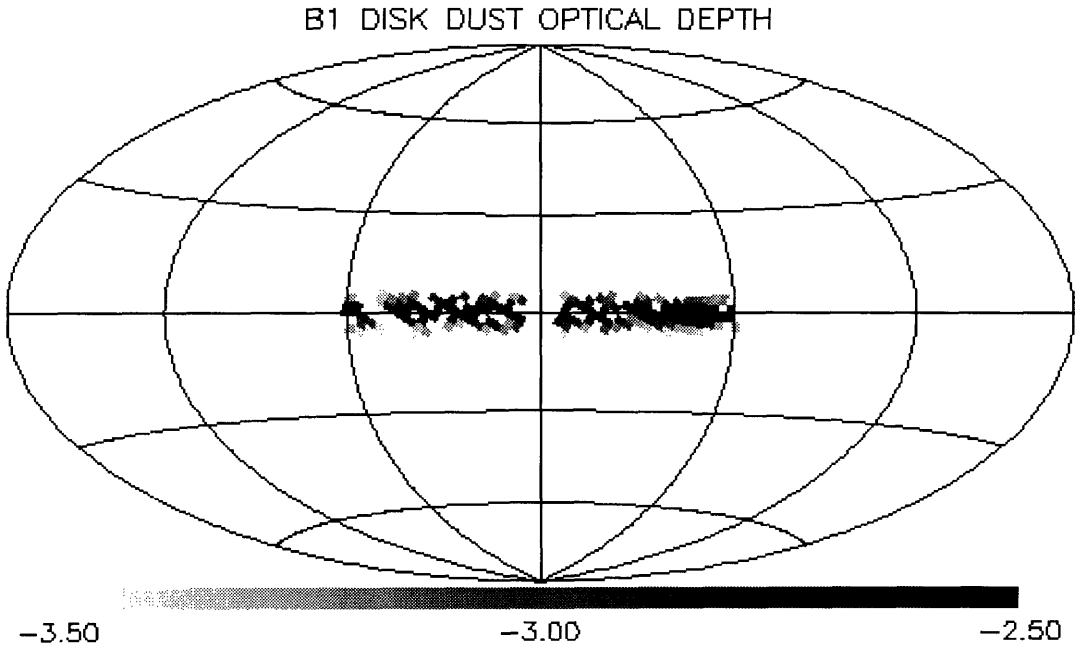

Figure 9-28: Log-scaled optical depth for hotter dust of the two dust model

$$+\tau\frac{(dT^2+\sigma^2)}{2}\left[\frac{\partial^2 D_\nu(T_1)}{\partial T^2}+\frac{\tau_2''}{\tau_1''}\frac{\partial^2 D_\nu(T_2)}{\partial T^2}\right]$$
$$+\tau\frac{(dT^3+3\sigma^2 dT+\mu^3)}{6}\left[\frac{\partial^3 D_\nu(T_1)}{\partial T^3}+\frac{\tau_2'''}{\tau_1'''}\frac{\partial^3 D_\nu(T_2)}{\partial T^3}\right] \quad (9.13)$$

To find the parameters τ, dT, σ, and μ describing the spectrum in each pixel we can no longer rely on linear template fitting, but must perform a nonlinear least squares fit to each spectrum.

Some spectra may not need the width and skew parameters so a routine was set up to fit each spectra and add in these parameters only if the F-test found their their inclusion significantly lowered the χ^2. The resulting parameters for the hot dust's optical depth, temperature, width and skew are presented in figures 9-28 – 9-31. Clearly this model is wrong. While the dust optical depth behaves relatively well, the hot dust temperature varies from 5 – 35 K. The dust width is only significant for 3 pixels and the dust skew has a rather large range. The dust temperature, width, and skew also show individual behavior at the single pixel resolution. Since we expect physical signals to be several pixels in extent, due to the oversampled beam, this behavior cannot be physical in origin.

The χ^2 for the fits to each spectra are plotted in figure 9-32 and are too high. The plot is

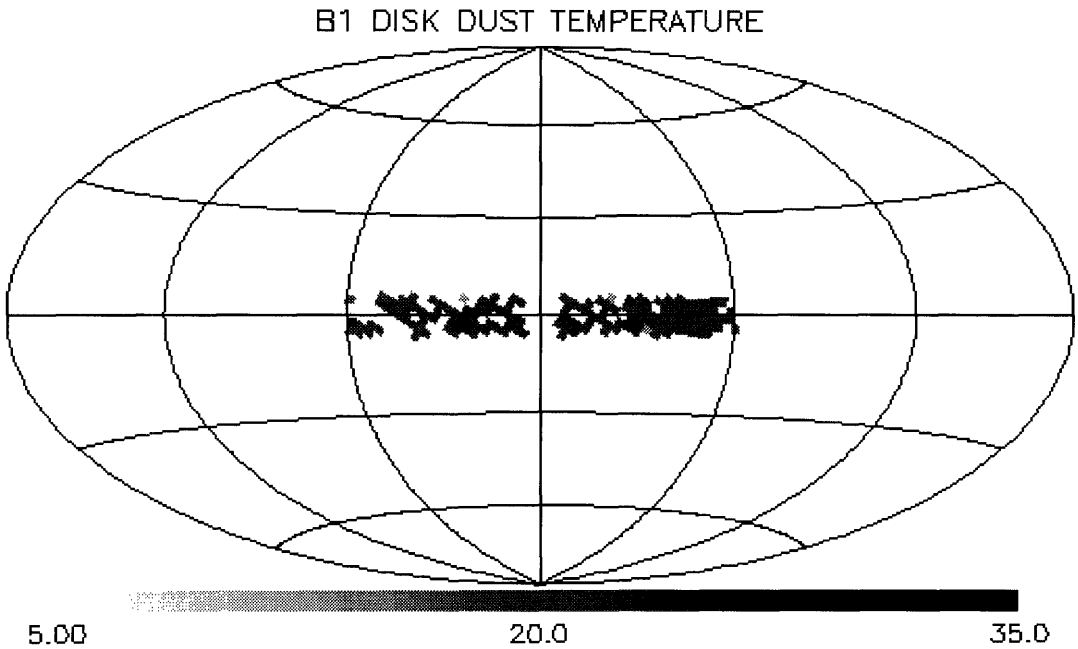

Figure 9-29: Temperature (K) for hotter dust of the two dust model

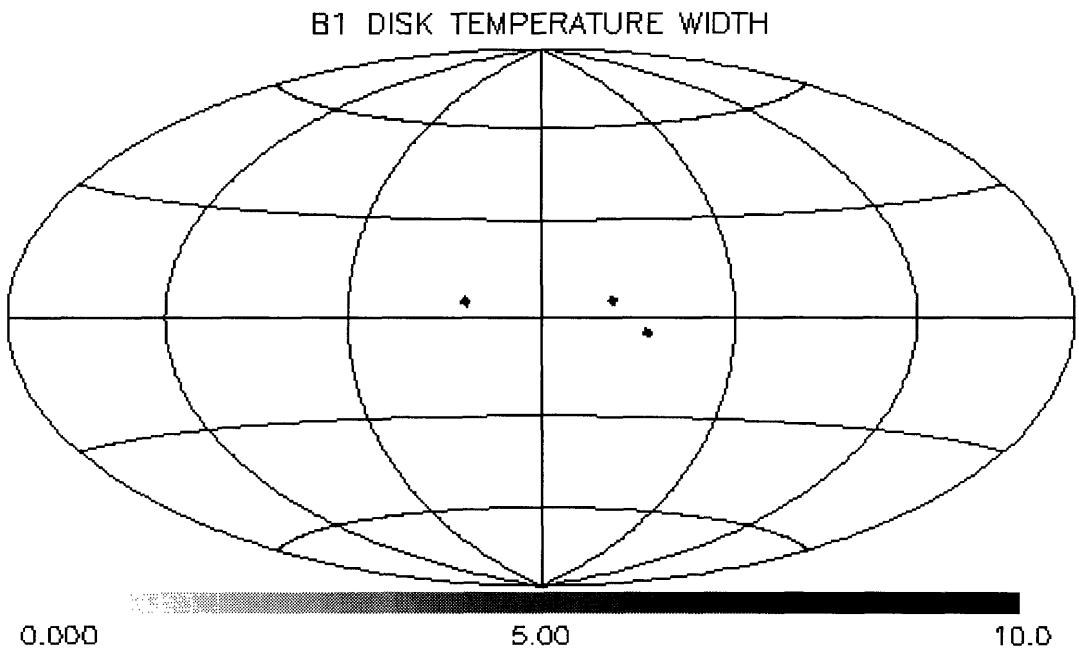

Figure 9-30: Width of the temperature distribution (K) for the hot dust

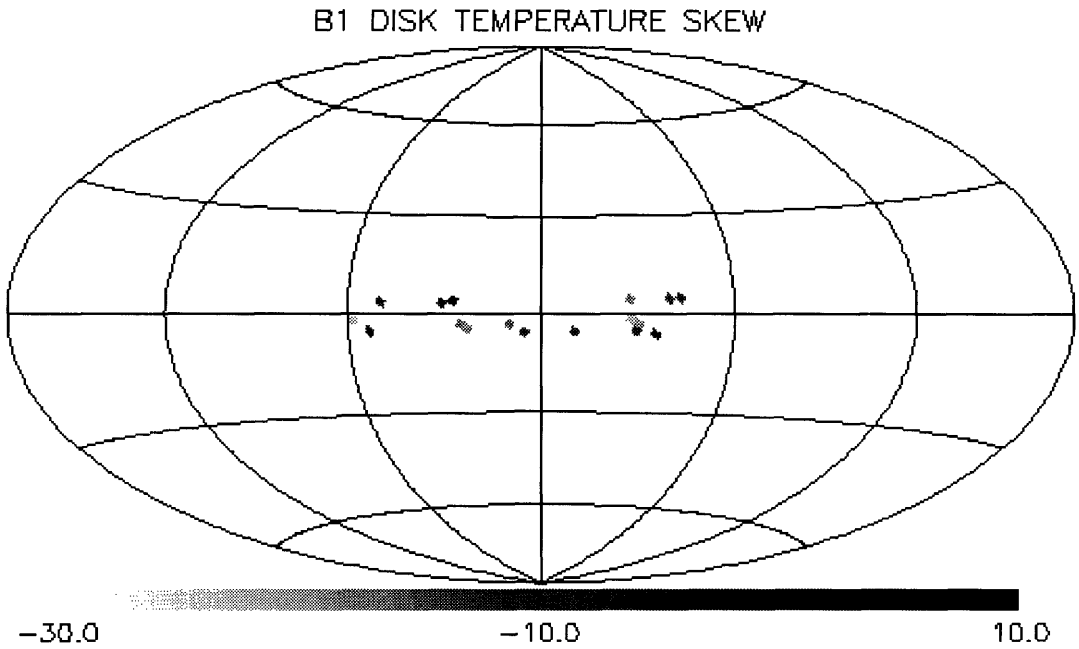

Figure 9-31: Width of the temperature distribution (K) for the hot dust

log-scaled so that, for our 161 frequency points, we expect a value $\log \chi^2 \sim 2.2$. A majority of the points, especially from regions of strong emission, have a χ^2 above 1000 indicating that the model is indeed unphysical.

Their are several explanations for the failure of PCA modeling to determine reasonable parameters along the galactic plane. The most obvious is our model is too simple. Other models were examined (two independent dusts each with a variable temperature, four dusts), but none worked any better on the components than the two dust model above. A more plausible explanation is that the PCA modeling suffers from its inherent linearization of the data. It relies on the assumption that each individual spectrum can be described by an expansion of a physical model about some common physical parameter. In the disk of the Galaxy, each line-of-sight most certainly samples a distribution of dust temperatures, whose combined intensity cannot be expressed as a function of the mean temperature alone. That is, the temperature distribution may be too wide to be described by linearization about a single temperature.

Analysis of the spiral arms and galactic center regions also suffer from the same reason as they sample lines-of-sight containing highly variable dust emission. In these regions it was

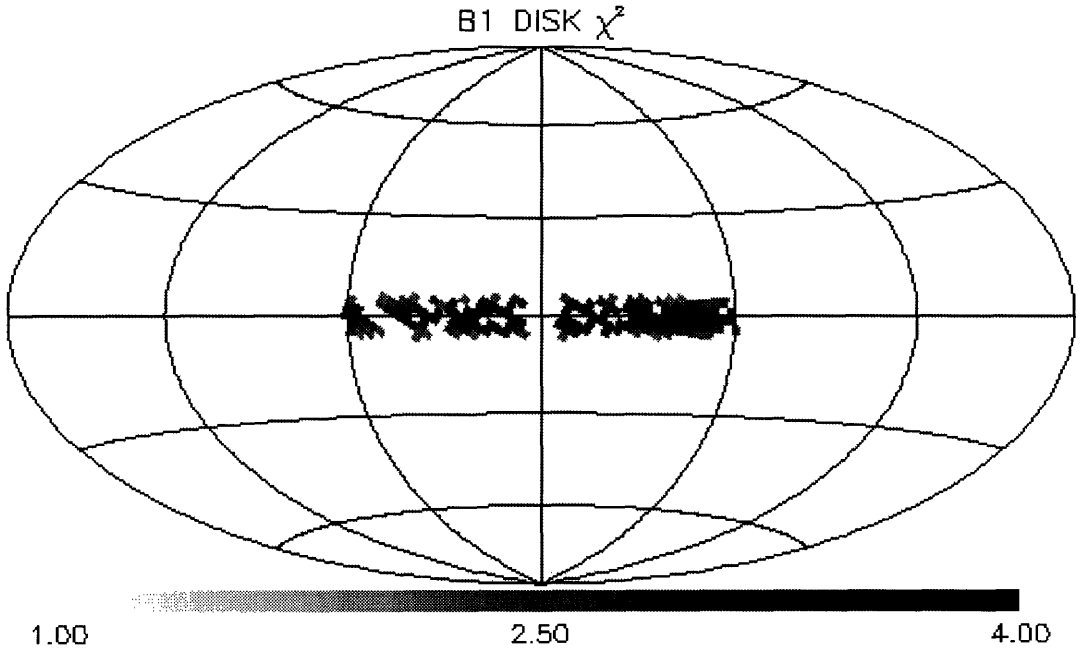

Figure 9-32: Log-scaled χ^2 for the two dust model fit

difficult to even model the spectral components.

9.5.3 Galactic Dust

To investigate the large scale variation in galactic dust optical depth we perform PCA on the entire data set except for the inner galactic plane. Treating the data set as a whole prevents discontinuities in the dust optical depth parameter due to the nonlinear dust parameters for different regions. The PCA modeling for the whole sky was performed as in Region B3 and the best fit parameters for the two dust model are a hot dust temperature of 18.11 K, a cold dust temperature of 6.85 K, and a cold to hot dust optical depth ratio of 2.19. These parameters are very similar to those determined from the lower latitude data which dominates the signal in the data set.

Using these parameters to produce spectral templates as in Region B3, we determine the hot dust optical depth and its temperature as they vary across the sky. The χ^2 for this fit is 633916 for 4868 $\times$ 161 DOF which yields .81 for the reduced χ^2. The maps of the hot dust optical depth and its temperature are presented in figures 9-33 and 9-34. Data for which the uncertainty in the dust temperature was greater than 2 K were excluded and accounted for only 5.7 % of the pixels. They mainly occurred in the higher latitudes which has very low signal to noise.

Using the optical depth map, we fold the negative latitudes onto the positive latitudes and determine the average dust optical depth in latitude bins 1° wide. The results for latitudes 5° – 90° are plotted in figure 9-35. Also plotted in figure 9-35 is the best fit cosecant law. The optical depth is expected to have this form if the galactic dust has a density that is a predominately a function of vertical distance from the galactic plane. We see that the law is well followed for these latitudes.

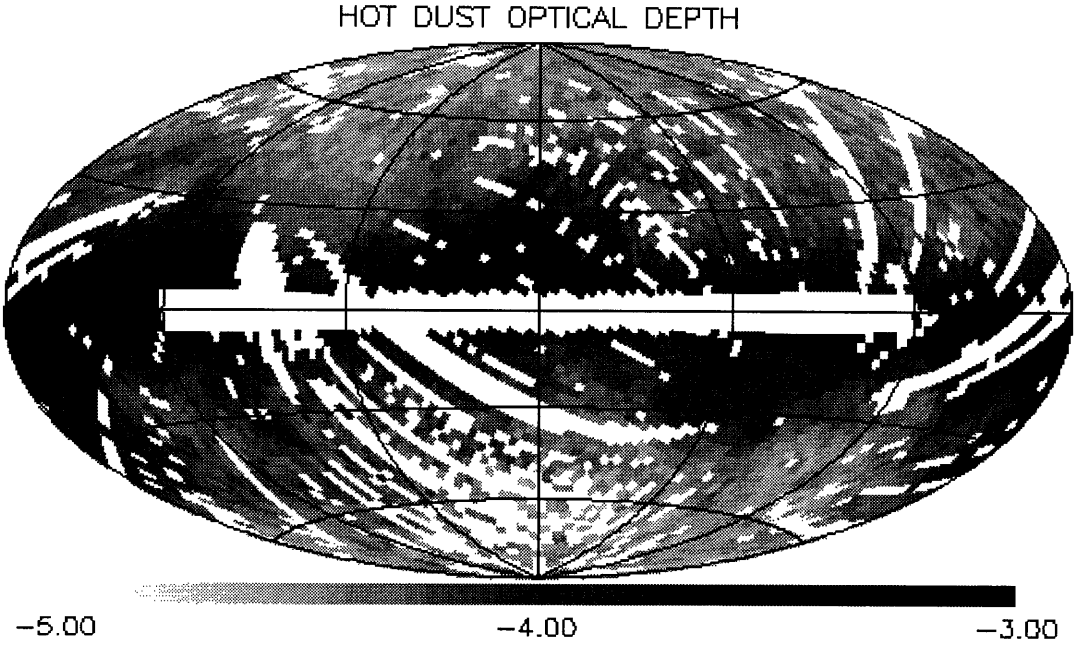

Figure 9-33: Log-scaled optical depth for hotter dust of the two dust model

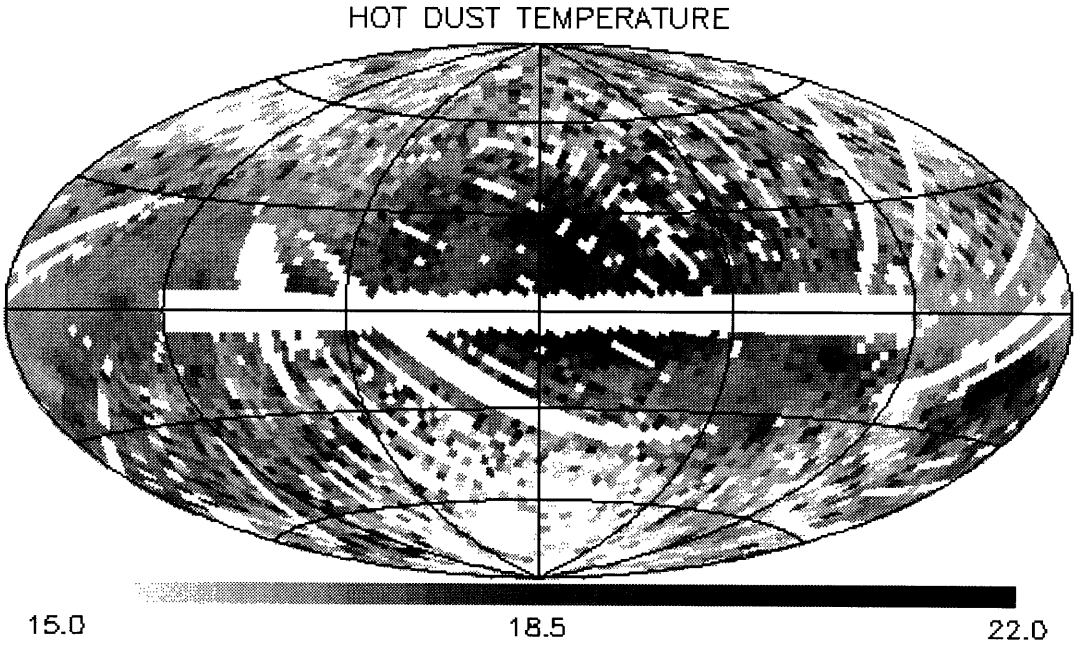

Figure 9-34: Temperature (K) for hotter dust of the two dust model

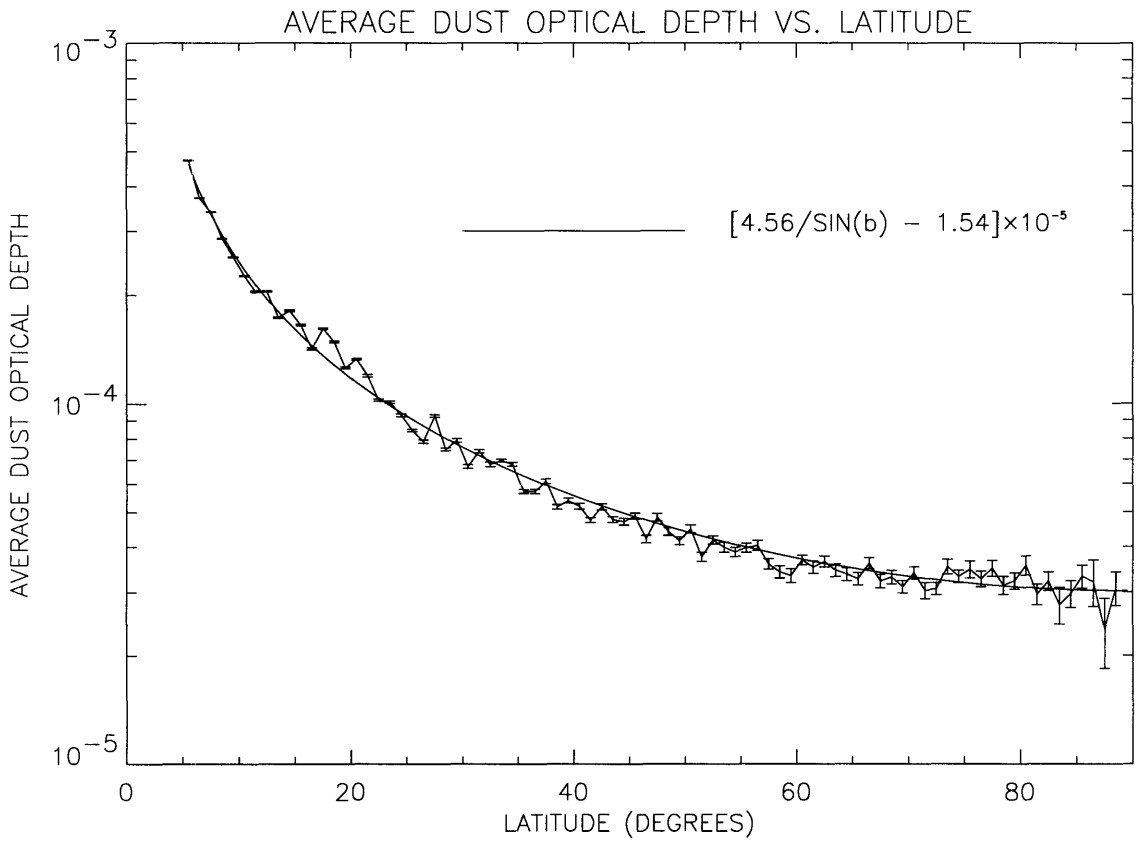

Figure 9-35: Average dust optical depth of hot component in 1° latitude bins

9.6 Conclusions

From a Principal Components Analysis of the FIRAS data we confirm the existence of a cold dust component in the ISM and that the PDR model can account for the observed emission from both dust and gas. We also show that the galactic dust for $|b| > 5°$ is consistent a plane parallel geometry.

9.6.1 Hot Dust

The morphology of hot dust optical depth was shown to exhibit the cosecant law

$$\tau(|b|) = \left[\frac{4.56 \times 10^{-5}}{\sin|b|} + 1.54 \times 10^{-5}\right] \tag{9.14}$$

The constant offset is unphysical, indicating a uniform dust component with *negative* optical depth. While this mathematical model has difficult physical interpretation, it works far better than a strict cosecant law. This negative offset was also found in the study of 100 μm dust emission from IRAS [Boulanger 88]. A strict cosecant law can be fit to the data at high latitude and extrapolated to lower latitudes. The low latitude optical depth of the dust is in excess of this model. The constant offset is necessary to model this increased optical depth.

9.6.2 Cold Dust

For the high latitude data of region B5 an unambiguous interpretation of the dust emission is problematic. Both PCA modeling and the template method indicate that the two dust model does not fit the data significantly better than the single dust model. The fitted emissivity index (~ 1) of the single dust model, however, is in conflict with most theoretical predictions [Draine 84], [Tielens 87], [Wright 93], and also lower than the fitted index (~ 1.5) from the other regions. A possible explanation is that the dust at high latitudes has a distribution of temperatures, which effectively demands a low emissivity index, while the data lacks sufficient signal to successfully determine two dusts.

The evidence for cold dust at lower latitudes is much more robust. Both PCA and the template methods indicate the two dust model is significantly better than the single dust model in agreement with [Wright 91]. While the four lower latitude regions show similar cold dust temperatures (~ 6.5 K), the optical depth ratio between the cold and hot components increases

from $\sim$ 2 in the outer galactic plane to $\sim$ 8 in latitudes near 40° . A possible explanation is that the PDR regions at lower latitudes have more extended envelopes responsible for the hot dust emission than those at high latitudes. There could also be dust at lower latitudes independent of the PDR regions which has the same hot dust temperature but lacks a cold component. This dust would add to the hot dust optical depth, lowering the optical depth ratio.

9.6.3 PDR Model

At high latitudes the lack of C^+ emission at high latitudes can be attributed to either shallow, low density PDRs without sufficient number or column density to produce C^+ emission, or an absence of PDR surfaces altogether. [Bennett 94] found that the line emission away from galactic plane arose predominately from the Cold Neutral Medium (CNM). They argued that the lack of C^+ at these latitudes indicated that the FIR continuum must come from warmer gas (WNM). A possible scenario is that very small grains residing in the WNM pulse with the absorption of each FUV photon. The spectrum from a collection of these particles will exhibit a temperature distribution as discussed above. In this scenario [Bennett 94] explained that the higher excitation conditions of the warmer gas allow other cooling transitions to dominate over the C^+ transition and the reduced density of the WNM decreases the cooling efficiency of this transition.

The PDR model does well in explaining the observed cold dust temperature in relation to the hot dust temperature. At the lower latitudes, the expected C^+ line intensities as a function of hot dust temperature agree with the observed relation to within a factor of two. As mentioned before, this discrepancy can be attributed to the exclusion of photons below 6 eV in the model's determination of dust heating. Another possible explanation is that extended dust envelopes surrounding the PDR add to the total dust optical depth while the C^+ originates only within the cloud. With this factor of two, the PDR model indicates that the observed dust and line emission can be attributed to regions with a neutral hydrogen density between 10 and 100 cm^{-3} which is expected for diffuse clouds. These values agree with [Magnani 85] who surveyed high latitude molecular clouds using CO observations. The clouds they investigated showed a range of densities from 35 to 500 cm^{-3} with a mean density of 140 cm^{-3}.

The ability to account for both the observed two temperature dust model *and* the C^+

intensity's dependence on dust temperature indicate that PDR model is a viable physical model for diffuse emission from galactic dust and gas. Subjecting this model to further tests will have to wait for the observations of the Infrared Telescope in Space (IRTS). The IRTS will include an FIR photometer with four bands covering the FIRAS frequency range with similar sensitivity but a .5° beam. The smaller beam size may allow the separation of the cold cores of dust clouds from hotter surface regions. Also onboard will be an instrument to detect the spectral lines of C^+ and O^0 which is the dominant cooling line for denser ($n \sim 10000$ cm^{-3}) regions. With the ability to study the spatial variations of cold and hot dust components and their associated emission lines, these future observations promise to test the limits of the PDR model.

Chapter 10

Summary

This thesis utilized data from the FIRAS instrument to determine the emission from galactic dust and gas. The method of Principal Component Analysis was refined and its use in modeling both the spectral and spatial variations of data was presented. The method of spectral component modeling was used to determine the physical parameters of thermal emission from galactic dust. These parameters and those describing the emission line of ionized carbon were used to test the photodissociation region (PDR) model of dust and gas emission from diffuse clouds. The PDR model was shown to account for both the cold dust component evident in the data and the observed dependence of the intensity of ionized carbon emission on the dust temperature.

Bibliography

[Anderson 84] Anderson, T.W. 1984, *An Introduction to Multivariate Statistical Analysis* (John Wiley & Sons, New York)

[Binney 87] Binney, J. and Tremaine, S. 1987, *Galactic Dynamics* (Princeton University Press, Princeton, New Jersey)

[Bennett 94] Bennett, C.L. *et al.* 1994, ApJ, submitted

[Bevington 69] Bevington, P.R. 1969, *Data Reduction and Error Analysis for the Physical Sciences* (McGraw-Hill, New York)

[Bohlin 78] Bohlin, R.C., Savage, B.D. and Drake, J.F., 1978, ApJ, 224, 132

[Boulanger 88] Boulanger, F. and Perault, M. 1988, ApJ, 330, 964

[Draine 84] Draine, B.T. and Lee, H.M. 1984, ApJ, 285, 89

[Emerson & Cuming Inc.] Emerson & Cuming Inc., Canton, MA 02021

[Fixsen 94a] Fixsen, D.J. *et al.* 1994, ApJ, 420, 445

[Fixsen 94b] Fixsen, D.J. *et al.* 1994, ApJ, 420, 457

[Fixsen 94c] Fixsen, D.J. private communication

[Francis 92] Francis P.J. *et al.* 1992, ApJ, 398, 476

[Gales 93] Gales, J. 1993, private communication

[Guhathakurta 89] Guhathakurta, P. and Draine, B.T. 1989, ApJ, 354, 230

[Habing 68] Habing, H.J. 1968, Bull. Astro. Inst. Netherlands, 19, 421

[Hauser 84] Hauser, M.G. *et al.* 1984, ApJ, 285, 74

[Hollenbach 79] Hollenbach, D.J., and McKee, C.F. 1979, ApJS, 41, 555

[Hollenbach 91] Hollenbach, D., Takahashi, T., and Tielens, A.G.G.M. 1991, ApJ, 377, 192

[Isaacman 92] Isaacman, R.B., Read, S.M., and Barnes, W.J. 1992, in Proc. Astronomical Data Analysis Software and Systems (ADASS) I, Astron. Soc. Pacific Conference Series 25, ed. D.M. Worrall, C. Biemesderfer, and J. Barnes (ASP, San Francisco, 1992), p. 403

[Kogut 93] Kogut, A. *et al.*1993, ApJ, 419, L1

[Kulkarni 88] Kulkarni, S.R. and Heiles, C. 1988, in *Galactic and Extragalactic Radio Astronomy* eds. Verschuur, G.L. and Kellerman, K.I. (Springer-Verlag, New York)

[McKee 77] McKee, C. and Ostriker, J.P. 1977, ApJ, 218, 148

[Magnani 85] Magnani, L., Blitz, L., and Mundy, L 1985, ApJ, 295, 402

[Mather 82] Mather, J.C. 1982, Appl. Optics, 21, 1125

[Mather 84a] Mather, J.C. 1984, Appl. Optics, 23, 584

[Mather 84b] Mather, J.C. 1984, Appl. Optics, 23, 3181

[Mather 86] Mather, J.C., Toral, M., and Hemmati, H. 1986, Appl. Optics, 25, 2826

[Mather 94a] Mather, J.C. *et al.* 1994, ApJ, 420, 439

[Mather 94b] Mather, J.C., Fixsen, D.J., and Shafer, R.A. 1993, SPIE Transactions on Infrared Instrumentation, submitted

[Mathis 92] Mathis, J.S. and Cardelli, J.A. 1992, ApJ, 398, 610

[Mezger 82] Mezger, P.G., Mathis, J.S., and Panagia, N. 1982, Astron. Astrophys, 105, 372

[Morrison 76] Morrison, D.F. 1976, *Multivariate Statistical Analysis* (McGraw-Hill, New York)

[Murtagh 87] Murtagh, F. and Heck, A. 1987, *Multivariate Data Analysis* (Reidel, Dordrecht)

[O'Neill 76] O'Neill, E.M., and Laubscher, R.E. 1976, *Extended Studies of a Quadrilateralized Spherical Cube Earth Data Base*, (NEPRF Technical Report 3-76)(NTIS Report AD-A026294)(Computer Sciences Corp. CSC/TR-76/6008)

[Searle 82] Searle, S.R. 1982, *Matrix Algebra Useful for Statistics* (John Wiley & Sons, New York)

[Sodroski 89] Sodroski, T.J., Dwek, E., Hauser, M.G., and Kerr, F.J. 1989, ApJ,336,762

[Tielens 85a] Tielens, A.G.G.M. and Hollenbach, D. 1985, ApJ, 291, 722

[Tielens 85b] Tielens, A.G.G.M. and Hollenbach, D. 1985, ApJ, 291, 747

[Tielens 87] Tielens, A.G.G.M. and Allamandola, L.J. 1987, in *Interstellar Processes* eds. Hollenbach, D.J. and Thronson, H.A. (Reidel, Dordrecht)

[Whitcomb 81] Whitcomb, S.E. *et al.* 1981, ApJ, 246, 416

[Whittet 92] Whittet, D.C.B. 1992, *Dust in the Galactic Environment* (IOP Publishing Ltd., Bristol)

[Wilkinson 90] Wilkinson, D. 1990, *Report to the COBE Science Working Group*

[Wright 91] Wright, E.L. *et al.* 1991, ApJ, 381, 200

[Wright 93] Wright, E.L. 1993, in *Back to the Galaxy*, AIP Conf Proc 278, eds. Holt, S.S. and Verter, F. (AIP, New York)